FACULTY
OF MATHEMATICS
AND PHYSICS
Charles University

DOCTORAL THESIS

Jakub Pekárek

Room-temperature semiconducting detectors

Institute of Physics of Charles University

Supervisor of the doctoral thesis: doc. Ing. Eduard Belas, CSc.

Study programme: Physics
Specialization: Quantum Optics and Optoelectronics

Prague 2017

I declare that I carried out this doctoral thesis independently, and only with the cited sources, literature and other professional sources.

I understand that my work relates to the rights and obligations under the Act No. 121/2000 Coll., the Copyright Act, as amended, in particular the fact that the Charles University has the right to conclude a license agreement on the use of this work as a school work pursuant to Section 60 paragraph 1 of the Copyright Act.

In Prague date 18. 07. 2017 signature: RNDr. Jakub Pekárek

Acknowledgement

I would like to thank especially my supervisor doc. Ing. Eduard Belas, CSc. for the procreative discussions about the ideas of the work and experiments. I am grateful to Prof. RNDr. Roman Grill, CSc. for theoretical discussions. I am also thankful to Prof. Ing. Jan Franc, DrSc., RNDr. Jakub Zázvorka, PhD., RNDr. Václav Dědič, PhD., RNDr. Martin Veis, PhD., Mgr. Lukáš Šedivý, Mgr. Martin Rejhon, Mgr. Katarína Ridzoňová and other colleagues at the Institute of Physics at Charles University for their help in my research and study.

My thanks also belong to my family and my closest friends for their support during my whole study at Charles University.

And least but not last, I would like to thank the Charles University Grant Agency for the financial support of the part of my PhD study.

Title: Room-temperature semiconducting detectors

Author: Jakub Pekárek

Department / Institute: Institute of Physics of Charles University

Supervisor of the doctoral thesis:

doc. Ing. Eduard Belas, CSc., Institute of Physics of Charles University

Abstract: Semiconducting material CdTe/CdZnTe has a huge application potential in spectroscopic room temperature radiation detection due to its properties. Such detectors can be used in medical applications, homeland security and for monitoring of nuclear facilities. However, the final device quality is influenced by many parameters. One crucial stage in detector fabrication is the proper surface treatment. The detailed study of surface treatments and their effect on final detector device is reported. Another crucial fact is the polarization of the detector caused by high radiation fluxes which negatively affects the use of such devices. The polarization occurs by capturing the photogenerated holes at the deep levels inside the semiconductor. The possible detector depolarization by infrared illumination during the detector operation has been experimentally verified and the obtained results are shown in this thesis. For optimal technology of preparation, it is also necessary to develop the fast characterization method for prepared detectors. The last aim of the thesis is to study the resulting quality of prepared planar and co-planar detectors by transient-current-technique (TCT). TCT is an electro-optical method allowing to determine variety of transport properties of radiation detectors, such as internal electric field profile, charge collection efficiency, mobility and lifetime of charge carriers, etc.

Keywords: CdTe/CdZnTe, surface treatments, depolarization, transient-current-technique

Contents

1. INTRODUCTION 3

1.1. CdTe and CdZnTe 3
1.2. Detector preparation and characterization 4
1.3. Motivation and goals 5

2. THEORY 7

2.1. Radiation detection in semiconductor detectors 7
2.1.1. Coplanar-grid detectors (CPG) 8
2.2. Detector surface and electronic contacts 10
2.2.1. Leakage current 13
2.3. Electron processes in semiconductor 14
2.3.2. Origin of defect levels 17
2.4. Carrier transport phenomena 17
2.4.1. Mobility and diffusion coefficient 18
2.4.2. Lifetime 19
2.4.3. Charge carriers trapping 20

3. GENERAL EXPERIMENTS USED FOR DETECTOR CHARACTERIZATION 21

3.1. Current-voltage characteristics 21
3.2. Radiation spectroscopy 22
3.2.1. Pulse height spectrum analysis 24
3.2.2. Transient charge technique 27
3.3. Transient-current-technique 28
3.3.1. Principle of transient-current-technique 28
3.3.2. Theory of transient-current-technique 31
3.3.3. Alpha-induced transient-current-technique setup 33
3.4. Ellipsometry 34
3.5. Pockels effect measurement 34
3.6. Infrared microscopy 36

RESULTS 37

4. SURFACE TREATMENTS ON CDTE/CDZNTE RADIATION DETECTORS 37

4.1. Samples preparation 39
4.2. Surface effect on current-voltage characteristics and pulse height spectrum analyses 40
4.3. Surface effect on the internal electric field 43
4.4. Surface effect on time stability 44
4.5. Chapter summary 49

5. INFRARED DEPOLARIZATION OF DETECTORS UNDER HIGH FLUX OF X-RAY RADIATION 50

5.1. Sample preparation and experimental section 51
5.2. Polarization and IR depolarization 54
5.3. IR depolarization in X-rays spectroscopy 57
5.4. Influence of IR depolarization on energy resolution 60
5.5. Chapter summary 62

6. TRANSIENT-CURRENT-TECHNIQUE AS A POWERFUL TOOL FOR DETAIL DETECTORS CHARACTERIZATION 64

6.1. Electronic pulse shape formation in transient charge and transient current detection approach in Cd(Zn)Te detectors 64
6.2. Laser-induced transient current pulse shape formation in Cd(Zn)Te planar detectors 72
6.2.1. Restoration of real current waveform shape 76
6.2.2. Charge collection efficiency set by L-TCT 82
6.2.3. Mobility-lifetime product set by L-TCT 84

6.3. INFLUENCE OF THE CRYSTALLOGRAPHY DEFECTS ON THE LASER-INDUCED TRANSIENT CURRENT WAVEFORMS 88
6.4. CHARGE TRANSPORT IN CDZNTE COPLANAR GRID DETECTORS EXAMINED BY LASER-INDUCED TRANSIENT CURRENTS 94
6.4.1. Experiment and experimental results 94
6.4.2. Theoretical methods and TCT simulations 98
6.4.3. Doping, depletion width and diffusion 103
6.4.4. Differential current sensing 106
6.4.5. Discussion of obtained results 109

7. CONCLUSION 111

BIBLIOGRAPHY 114

LIST OF TABLES 122

LIST OF ABBREVIATIONS 123

1. Introduction

In the early 1950-ies, the development of semiconducting materials led to a huge expansion of technology based mainly on silicon and germanium. One of the useful applications of semiconductor materials and technology is the detection of high–energy radiation (X-ray and gamma-ray). In the case of Si and Ge, the absorbed radiation is directly converted to the measured signal (see chapter 2.1 Radiation detection in semiconductor detectors). Such a direct approach of radiation detection has a better spectroscopic resolution than indirect approach like in scintillators.

However, in the following years some disadvantages of these materials appeared, limiting their use in detection applications. In the case of Si, it is low sensitivity of radiation detection with energy higher than several tens of keV, and, in the case of Ge, it is relatively high volume (up to 100 cm^3) necessary for efficient operation. Because of their small bandgaps (1.12 eV for Si, 0.67 eV for Ge at 300 K), both materials must have been cooled down to liquid nitrogen temperatures to avoid excessive thermal currents. Therefore an alternative semiconducting III-V and II-VI compound materials, like GaAs or CdTe, were explored and investigated.

This work is focused on the study and characterizations of CdTe and its compounds based detectors. The essential theory for understanding all studied problems is written in chapter 2 "Theory" and the standard experimental methods used in this work are described in chapter 3 "General experiments used for detector characterization". Results and discussions are divided into three chapters – 4 "Surface treatments on CdTe/CdZnTe radiation detectors", 5 "Infrared depolarization of detectors under high flux of X-ray " and 6 "Transient-Current-Technique as a powerful tool for detail detectors characterization". The summary of all results is in the "Conclusion".

1.1. CdTe and CdZnTe

The first comprehensive study of Cadmium Telluride (CdTe) material was published in 1959 by de Nobel [1], in which basic structural, electrical and optical properties of this material were described. CdTe crystallizes in a cubic zinc-blende

structure and its advantages comparing to previously mentioned semiconductors are a high mobility of carriers, direct band gap, and high atomic number.

In recent years, an increased interest in uncooled detectors of X-ray and gamma-ray radiation has been recorded. CdTe and Cadmium Zinc Telluride (CZT) have been previously reported as an promising material with a huge range of applications (national security, medical imaging, astrophysics, etc.) [2]–[4]. Both of the materials have a high charge collection efficiency (CCE) and spectral energy resolution while operating at the room temperature. It is not necessary to cool them down because they have a small thermal noise, due to a relatively high band gap ~ 1.5 eV at 300 K. That is why CdTe and CZT detectors are nowadays used in the mammographic X-ray spectroscopy where they can compete with Ge and Si sensors [4]. Furthermore, CdTe and CZT detectors show better spectral energy resolution than NaI(Tl) scintillating detectors which are mostly used in positron annihilation spectroscopy [4]. Also the use of these sensors in astrophysical application have already been demonstrated with the European astronomic satellite, INTEGRAL, and in the NASA mission SWIFT [5].

Besides the fact, that CdTe material has a great application potential in the detection of X-ray and gamma-ray radiation, it is also used for the production of electro-optical modulators and as a substrate for the epitaxial growth of the semiconductor $Hg_{1-x}Cd_xTe$ which is a high-quality infrared (IR) radiation detector.

Another field of application is in solar cells where, after crystalline silicon, CdTe thin films are the second most common photovoltaic (PV) technology in the world marketplace, currently representing 5% of the world market. "*CdTe thin-film solar cells can be manufactured quickly and inexpensively, providing a lower-cost alternative to conventional silicon-based technologies. The record efficiency for a laboratory CdTe solar cell is 22.1% by First Solar, while First Solar recently reported its average commercial module efficiency to be 16.1% at the end of 2015*" [6]. For comparison, the silicon solar cells are nowadays at 18% – 22% of efficiency under standard test conditions.

1.2. Detector preparation and characterization

CdTe/CZT single crystals are usually grown by the Travelling–Heater–Method (THM) or High-Pressure-Bridgman (HPB) or by the Vertical–Gradient–Freeze–

Method (VGF). The intentional doping elements used to increase the resistivity are placed into the ampoule prior to melting. By itself as-grown material can contain various defects and impurities. These act as donors or acceptors and they create shallow or deep levels inside the bandgap which impede a higher resistivity of the samples. Impurities can be embedded from the crystal ampoule or doping and defects arise as a result of tension at the crystal surface, etc. Defects and impurities are described in chapter 2.3.2 “Origin of defect levels” and their effect is described, for example, in chapter 2.4.3 “Charge carriers trapping”. The deep energetic levels comparing to the shallow levels are interesting due to their participation in longer trapping and higher recombination of free photogenerated charge carriers. When charge carriers are trapped at the deep level, space charge is induced inside the detector and the effect of polarization can occur. Polarization causes that the inner electric field is concentrated under one of the biased electrodes and almost zero electric field is formed under the other electrode. Charge carriers are not accelerated in this part of the sample and can be transported only through diffusion. Therefore their probability of trapping and recombination is much higher. Thus polarization influences the final CCE of the detector.

After the growth, the crystal is cut into smaller monocrystalline samples and the proper surface treatments have to be applied. Surface treatments influences the value of leakage current on the surface of the detector which can disturb the final detector properties. The current flowing on the surface of the detector can be greater than the bulk current by orders of magnitude. Also the surface treatments affects the final metal-semiconductor contacts which are created on the opposite sides of the sample. Even though the surface preparation effects are widely studied in these days, the optimal surface processing is still under discussion.

After the preparation of the detector, it is connected to an electronic readout system that can evaluate the current pulses induced by absorbed radiation and the sample properties can be set by various methods.

1.3. Motivation and goals

CdTe single crystals and its compounds have been studied several years at the Institute of Physics of Charles University (IoP CU). They were grown by VGF method and characterized by various electrical, optical and spectroscopic methods in order to

compare their properties with commercially available materials. There are many stages in development of high quality radiation detectors. One of the key-problem in the fabrication of high performance detectors is high level of leakage current. This thesis is focused on the development of optimal detector surface treatment which resulted in the suppression of the leakage current.

The second one is polarization occurring at the high fluxes due to capturing of the high amount of charge carriers at the deep levels. The best detectors, in a meaning of homogeneity and small amount of impurities (thus small concentration of deep levels), which are currently commercially available costs hundreds to thousands dollars. Therefore it is also necessary to develop methods how to use less quality and cheaper material which is also subject of this thesis.

As it is indicated, the preparation technology of CdTe/CZT detectors is still insufficiently effective and needs to be further optimized. But for this, it is also necessary to develop methods that will enable the rapid characterization of prepared detectors with subsequent proposal of their possible modifications. One convenient option is the measuring of transient currents (TCT), where the current pulse shape is analysed. The current pulse is created by the charged carriers passing through the detector in the applied electric field. Electron-hole pairs (e-h pairs) are generated near one of the electrodes by the impact of alpha particles that penetrate only to a small depth under the irradiated electrode [7], [8], or by using an optical pulse of wavelength shorter than the value corresponding to the width of the band gap [9], [10], or by using an electron source [11], [12]. From the shape of the current pulse, it is possible to determine a number of transport parameters that characterize the quality of the detector. These are mainly charged carrier mobility, internal electric field profile, density of the spatial charge, thickness of the depleted layer in the detector, and trapping time of the charge carriers. Testing of transient-current-technique as a fast characterization method for planar and co-planar detectors is the third goal of this thesis.

2. Theory

2.1. Radiation detection in semiconductor detectors

If an ionizing radiation is wanted to be characterize, it must be detected by a suitable ionizing radiation detector. In most cases, detectors that provide an electrical output signal are used. Detection of ionizing radiation is based on the interaction of radiation with matter. Only the corpuscular particles (α, β) directly interact with the substance. Conversely, γ photons and X-ray photons propagate loosely in the material and ionize and release the charged particles as a result of photo-effect, Compton's phenomenon and the generation of an electron-positron pairs [13].

When using a spectrometric detector, it can be obtained not only the information about registration of the particle interaction and the time when the interaction occurred, but also the energy of that particle from which it is possible to re-determine what particle it is. The huge part of spectrometric detectors are photon detectors. Photon detectors operate on the principle of external or internal photo-effect [13]. The output signal of photon detectors depends on the energy of the incident radiation, the absorption coefficient of the material from which the detector is made, and the amount of the generated charge. This category includes, for example, photomultiplier (external photo-effect) and semiconductor detectors (internal photo-effect).

The simplest semiconductor detector design is a photoconductor [13]. It is a passive electronic component without a P-N transition whose electrical resistance is proportional to the photon flux. Incident photons generate (e - h) pairs and these contribute to the reduction of electrical resistance. If the external electric field is applied to the photo-resistor, carriers will be transported, resulting in a change in the electrical current in the circuit. The photoconductor measures either a directly increased current (photoconductivity) proportional to the photon flux (the more photons irradiates detector, the more (e - h) pairs are created) or the voltage drop on the load resistor R_L. The basic diagram of the connection of the photoconductor is shown in Fig. 2.1.

Important material parameters of a high-quality X-ray or gamma ray semiconductor detector include a high atomic number Z, whose value in power increases the absorption coefficient; high resistivity ρ, increasing the sensitivity of the

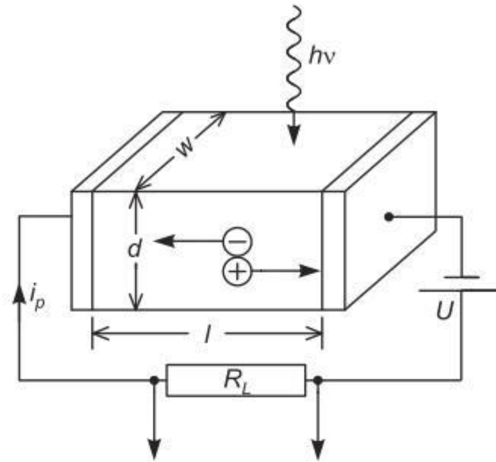

Fig. 2.1 *Schematic diagram of the photoconductor which consists of a slab of semiconductor and two ohmic contacts at the ends.*

detector; large width of band gap E_g, enabling high-energy radiation to be detected and reducing the thermal noise of the detector; and the high value of the $\mu\tau$ product, characterizing the charge transport inside the detector.

2.1.1. Coplanar-grid detectors (CPG)

The negative property of CZT detectors is its indirect proportions of the detector thickness relative to the signal detection capability. Not only the detection capability but also other detector parameters are influenced by its thickness. In the case of CZT, this is in principle a phenomenon, where after generating (e - h) pair, fast electrons are collected on the anode in a short time, whereas slow holes (mobility of holes is 10× smaller then electrons) have a great probability of trapping and travel long time through the sample to the cathode, which greatly affects CCE [13]. This phenomenon is generally observed in thicker detectors (> 5 mm in thickness). Compare to that, thin samples have a much lower detection efficiency of γ-radiation.

The best way to deal with the capture of holes in the detector is to scan only one charge. Otherwise, neglect the influence of holes and only take into account the negative electrons. This can be done by hemispheric detectors or pixel detectors where the internal field is rectified on small collecting anode [14] or by CPG concept. The whole idea is based on the modification of gas ionization chambers, which was first introduced by Frisch in 1944 [15], who inserted a grid electrode, known as Frisch

grid - FG, near the anode [16], [17]. FG behaves as an electrostatic shield in the area between the cathode and the grid while the area between the grid and the anode becomes highly sensitive to the movement of the charge carriers. Thus, the number of events recorded between the cathode and the grid, which is the bulk of the detector volume, is reflected by the rapid movement of electrons through the grid and the induction of their entire charge on the anode, while the slow cations travel in the opposite direction and do not induce any charge on the anode.

In 1994 P.N. Luke discovered a similar method suitable for use on semiconductor detectors, which is called the coplanar grid [18]. The coplanar grid consists of a series of narrow strips which are coplanarly connected together, as shown in Fig. 2.2. Fig. 2.3 shows a schematic diagram of such a coplanar-grid detector (CPG) connection.

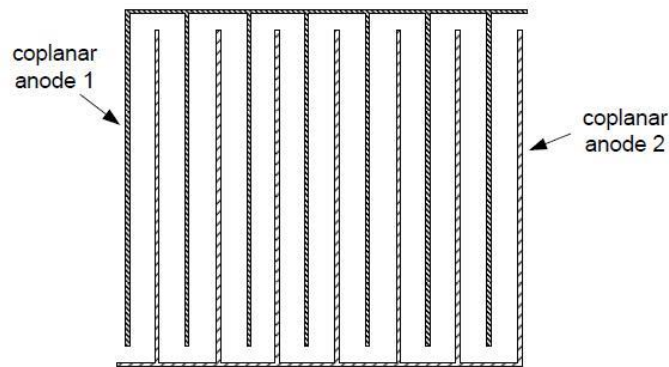

Fig. 2.2 *First generation of Coplanar Grid construction* [19].

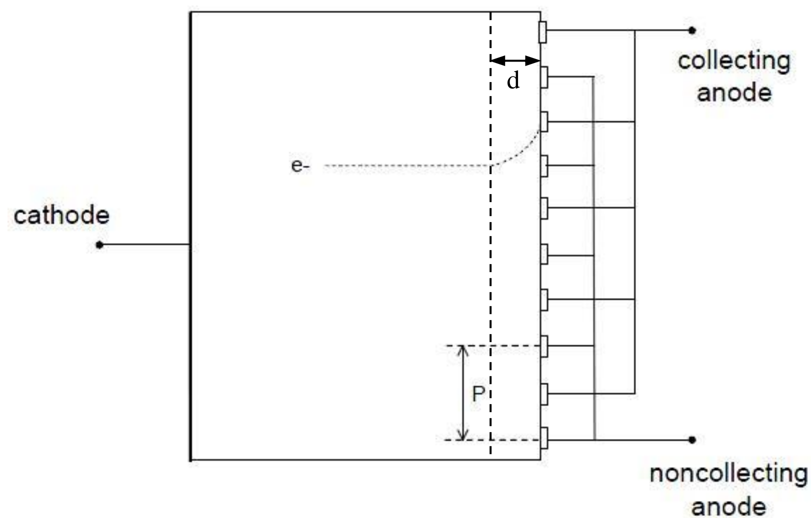

Fig. 2.3 *Schematic diagram of CPG connection. Full cathode and coplanar grid anode.*

Fig. 2.2 shows two anodes. Anode 1 is collecting grid – CG, it is connected to external voltage which allows it to positively biased, whereas anode 2 is non-collecting grid – NCG and is grounded. By the biasing of CG to tens to hundreds of volts, electrons at the distance *d* from anode side are rectified towards CG and by the calculation of the signal difference between the two grids it can be achieved a signal sensitive only to electron movement. A big advantage of CPG is the construction of coplanar grid on one surface of the semiconductor crystal.

The CPG construction itself is of great importance to the overall energy resolution of the detector. This is due to the unbalanced weighting potential for the collecting and non-collecting anode at a given depth of the detector. However, for the first CPG generation shown in Fig. 2.2, there was a difference between potentials on the left side and right side. Therefore, several improvements have been made to reduce this deficiency [18], [20]. Although the resolution of the most recent 3rd generation of CPG is close to 2% FWHM at 662 keV [18], a great influence on the detection properties of such a structure at higher voltages has the leakage current [21] discussed in chap. 2.2.1.

2.2. Detector surface and electronic contacts

The resulting quality of the detector is not only influenced by the material parameters (resistivity ρ, $\mu\tau$ product, sample width L, material homogeneity [13], ...), but also by the type of electronic contact which is prepared on the surface of the semiconductor detector [13], [22]–[24]. Basically, there are two types of metal contacts, rectifying Schottky contact or linear Ohmic contact. In the ideal case, the difference between the work function of metal and the semiconductor defines what type of barrier (thus the type of contact) is created.

The causes of barriers at metal-semiconductor (MS) contacts can be summarized in three categories [23]:

(1) Improper matching of work function between the metal and semiconductor.
(2) Presence of surface states on the semiconductor, producing an intrinsic surface barrier.
(3) Presence of thin layer of a third material (such as an oxide – MOS structure) which in turn causes barriers for reason 1 or 2 above.

Such barriers usually demonstrate their presence by giving rise to rectification effects, i.e. the resistance to current flow is much less for one direction of the applied field than for the reverse direction. When the barrier arises from the surface states, it pre-exists at the semiconductor surface even before a contact is established [24].

There are two mechanisms how charge carriers can cross this barrier [23]:

a) By quantum mechanical tunnelling through the barrier.

b) By passing over the barrier possessing sufficient energy.

The barriers resulting from improper matching of work function between metal and semiconductor is shown in Fig. 2.4 representing energy level diagrams for an n-type semiconductor and metal. The energy levels for a metal with work function ϕ_m (from Fermi level F_m to vacuum energy level E_{vac}) and for a semiconductor with electron affinity χ_s and work function ϕ_s ($\phi_s < \phi_m$) are shown in Fig. 2.4 (a), when the metal and semiconductor are still separated. E_c, F_s and E_v are conducting band, semiconductor Fermi level and valence band, respectively.

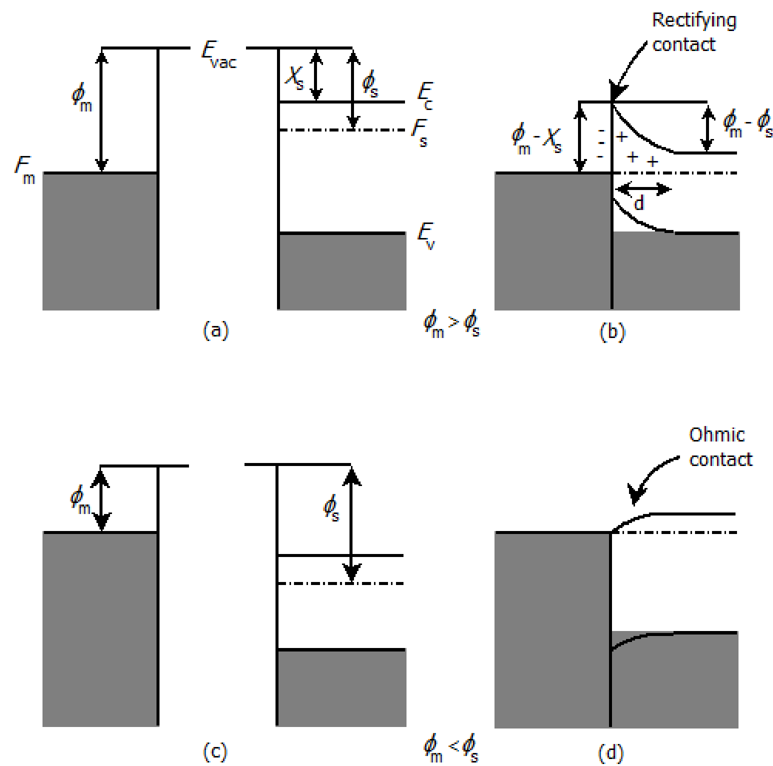

Fig. 2.4 *Energy level representation between metal and n-type semiconductor contact. (a) before and (b) after connection with a metal of greater work function than that of semiconductor; (c) before and (d) after connection with a metal of smaller work function than that of semiconductor.*

After the connection, the equilibrium state shown in Fig. 2.4 (b) occurs. Fermi levels of two materials come into coincidence by thermodynamic rules. Barrier is formed by negative charge at the contact and positive charge (ionized donors distributed in a volume) of semiconductor reaching a distance d from the contact (known as screening length [24]). The final barrier height is given by [23], [24]

$$\phi_B = \phi_m - \chi_s. \quad (2.1)$$

Fig. 2.4 (c) and (d) show the alternative case when the work function of the metal is smaller than that of the n-type semiconductor. In this case, no barrier is formed when contact is made. Such contact is called Ohmic contact because currents passing through the contact obey the Ohm's law over a large range of applied bias.

The ideal case of MS contact (discussed above) can be applied only to the endless crystal or to a part of the final crystal at a sufficient distance from the surface. Near the surface, the grid constant changes from the bulk one, and the material's physical properties change too. It can also be assumed that the contact materials are not chemically inert and the product of their chemical reaction is formed at the interface. However, the surface is predominantly affected by the absorption of atoms from the environment, especially oxygen atoms. A minimum of monoatomic layer of foreign impurities is always absorbed on the surface. Since it may be a monocrystalline, polycrystalline and amorphous layer, it is very difficult in such case to apply energy band theory. In most cases, this layer has semi-insulating properties. Therefore the establishment of an equilibrium between surface and the volume results in the existence of an intrinsic surface barrier which is presented even before the contact is achieved. In this case the contact barrier is independent of the work function of the used metal and the eq. (2.1) is no longer valid. The real Schottky contact is shown in Fig. 2.5 where d stands for the thickness of the interlayer.

According to [23], a real Ohmic contact can be defined as a contact which does not add a noticeable parasitic impedance to a given structure and which does not noticeably alter the equilibrium concentration of the current carriers in the semiconductor volume and thus does not change the nature of the device.

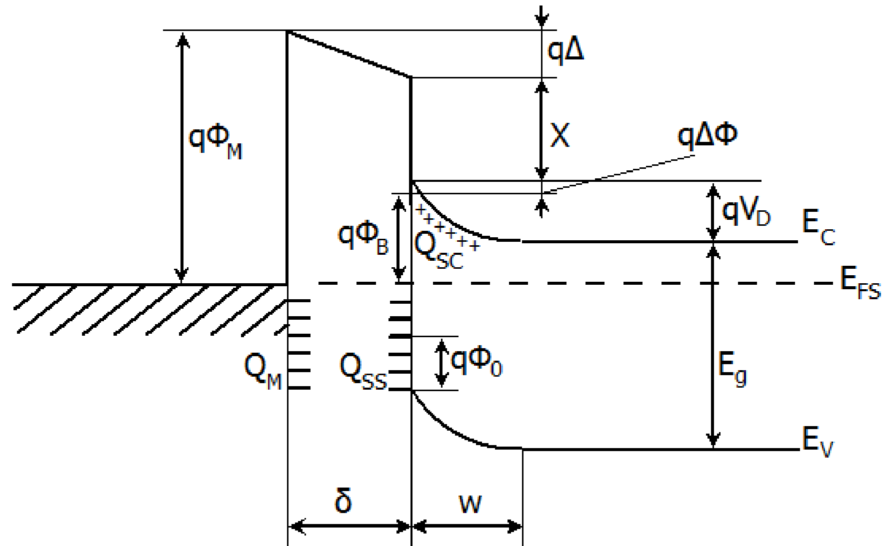

Φ_M = work function of metal
Φ_B = barrier height of MS barrier
Φ_0 = energy level at surface
$\Delta\Phi$ = image force barrier lowering
Δ = potential across interfacial layer
χ = electron affinity of semiconductor
V_D = built in potential
δ = thickness of interfacial layer
w = width of space-charge region
Q_{SC} = space-charge density in semiconductor
Q_{SS} = surface-state density on semiconductor
Q_M = surface-charge density on metal

Fig. 2.5 *Detailed energy level diagram of a metal and n-type semiconductor contact with an interface layer of the order of atomic distance* [13].

2.2.1. Leakage current

Not only the final contact is affected by the surface states that form the interlayer between metal and semiconductor, but the rest of the detector surface is affected too. Non stoichiometric surface and free dangling bonds on the surface are easy to oxidize [25] and these oxides most often give rise to a leakage current.

Leakage current is an electrical current that flows unintentionally along the detector surface under normal conditions. Thus, it is necessary to provide more power to the detector to compensate for loss of the leakage current. At the same time, the leakage current generates heat, thus it becomes a source of noise and in time, it causes a degradation of the detector [26].

The leakage current on CdTe detectors can be reduced by creating Schottky contact on one side of the detector. Thus created detector has a lower leakage current than the detector with two ohmic contacts, however, the detector is polarized by the rectifying contact, thereby the detection properties degrade [27], [28]. Another possibility how to reduce the leakage current magnitude are the different methods of surface etching or the surface passivation, which eliminates conductive surface states. In addition, it has also been shown that the guard ring (GR) structure can be used for separating the leakage current from the current flowing through the sample [29], [30]. Essentially, the GR is a metal contact which fully surrounds the inner anode as seen in Fig. 2.6. Both the GR and the inner anode are connected to the same potential, so there is no current passing between the two electrodes. Therefore, it is assumed that GR collects all the leakage current and the inner anode is used for measuring the signal.

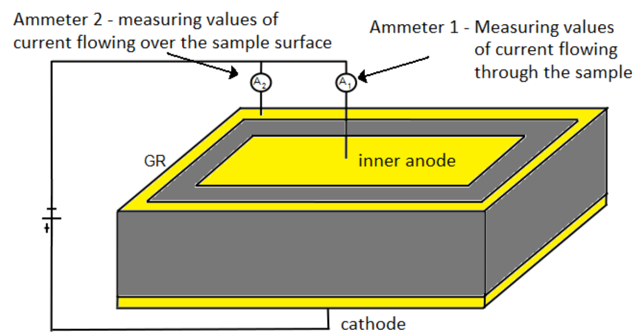

***Fig. 2.6** Diagram of the detector with guard ring structure.*

2.3. Electron processes in semiconductor

Many photoelectric phenomena in semiconductors are connected with free carriers' activity. These include optical absorption by which free carriers are created, electrical transport by which free carriers contribute to the electrical conductivity of the material, and capture of free carriers leading either to recombination or trapping.

2.3.1. Electronic transitions

Above mentioned effects are illustrated in Fig. 2.7. Intrinsic absorption in Fig 2.7 (a) corresponds to the excitation of electrons from valence band to the conduction band of semiconductor. Extrinsic absorption corresponds to the excitation of electron from defect level to the conduction band (Fig. 2.7 (b)) or the excitation of an electron from valence band to a defect level as in Fig. 2.7 (c).

Optical absorption for the light with intensity of I_0 in the sample with thickness of d is given by Beer's Law:

$$I = I_0 \exp(-\alpha d) \tag{2.2}$$

where α is the absorption constant [22]. There is a cutoff of absorption at the minimum energy required for transition; this minimum energy corresponds to the band gap energy for intrinsic transition (Fig. 2.7 (a)). For light with energy greater than the minimum required, absorption is continuous and fairly constant. The connection between light energy E and its wavelength λ is given by

$$E[eV] = \frac{hc}{e\lambda} = \frac{1239.84}{\lambda[nm]}, \tag{2.3}$$

where h is Planck's constant, c is speed of light and e is elementary charge. For light with energy smaller than energy of the band gap, the transition occurs only at the energy of light corresponding to the energy of specific defect level (Fig. 2.7 (b), (c)). A free electron can be captured at a defect level as in Fig. 2.7 (d) or free hole can be captured at a defect level as in Fig. 2.7 (e). The capture process is described by a capture cross section of charge carriers S_c and thermal velocity of free carriers v_{th} that the rate of capture R of species with density n by a species with density N_t is given by

$$R = S_c v_{th} n N_t. \tag{2.4}$$

When capture of free charge carriers leads to recombination with opposite charge carriers, a recombination process has occurred. The lifetime of a free carrier τ,

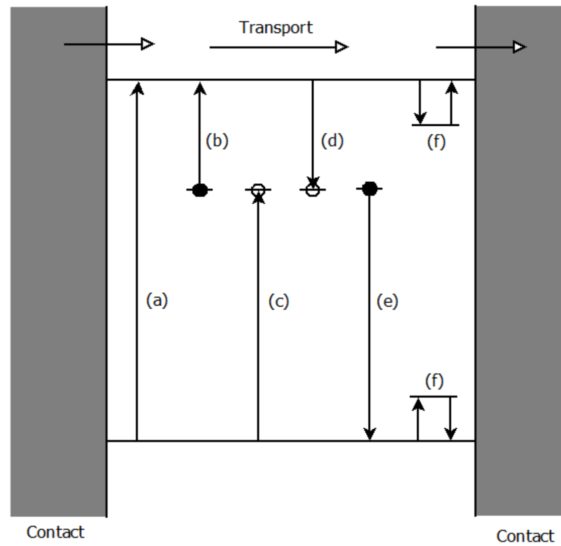

Fig. 2.7 *Major transitions and phenomena associated with photoelectronic effects in semiconductors. (a) intrinsic absorption, (b) and (c) extrinsic absorption, (d) and (e) capture and recombination, (f) trapping and detrapping.*

i.e. the average time when the carrier is free before recombination, is given by

$$\tau = \frac{1}{S_c v_{th} N_t}. \tag{2.5}$$

If the more than one type of recombination process is present, the individual recombination rates add.

A captured carrier at a defect level may (i) recombine with a carrier of opposite type, as just described, or (ii) be thermally re-excited to the nearest energy band before recombination occurs. In the (ii) case the imperfection is referred as a trap, and the capture and release of the carrier are called trapping and detrapping. Fig. 2.7 (f) shows such a trapping and detrapping situation. Centre with energy level lying near one of the band edges (shallow levels) will be more probably a trap than a recombination centre and vice versa for centres with levels lying near the middle of the band gap (deep levels). The distinction between traps and recombination centres is a distinction drawn on the basis of the relative probability of thermal injection versus recombination, i.e., on kinetic conditions, and not on the basis of intrinsic nature of the centres themselves [23].

2.3.2. Origin of defect levels

Defect levels in CdTe semiconductor are formed mostly by native point defects or by extrinsic point dopants.

In the case of native point defects in a binary compound *AB,* cation and anion vacancies V_A, V_B, interstitials A_i, B_i, antisite defects B_A, A_B, and complex defects like vacancy-antisite complex V_AB_A can be created. This is due to crystal growth at nonzero temperature when the deviations from the ideal distribution of atoms inside the crystal occur and these native defects are formed.

The extrinsic point defects originate from the present of impurities inside CdTe crystal. They can be divided into (i) impurities uncontrollable present in crystals and (ii) dopants specially introduced into the crystal to modify the physical and chemical properties of the material. The main aim is to prepare material with impurity concentrations as low as possible to attenuate their influence on the crystal properties. This goal is successfully reached by combination of purification methods, e.g. zone refining. Typical uncontrollable impurities in CdTe are Cu, Li, Na, Ag, K and O. Contrary to impurities, dopant's atoms are intentionally introduced to the material resulting in changing of its physical properties. The most important ones are indium and chlorine dopants. Both behave as shallow donors and together with a cadmium vacancy create also an acceptor-like complex defect called "A-centre".

Other types of defects which can be found in CZT crystals are line defects, plane defects or second phase defects. More about defects, their origin and compensation is in [31].

2.4. Carrier transport phenomena

The transport process in semiconductors, as usually described in terms of scattering effects or carrier mobility, determines how the change in free carrier density (e.g. due to illumination) affects the actual electrical conductivity. The total current density $\mathbf{J_{tot}}$ can be expressed as the sum of a drift current $\mathbf{J_{dr}}$ and a diffusion current $\mathbf{J_{df}}$ as [22]

$$\mathbf{J_{tot}} = \mathbf{J_{dr}} + \mathbf{J_{df}}. \quad (2.6)$$

2.4.1. Mobility and diffusion coefficient

The drift current due to a free electrons is given by

$$\mathbf{J_{dr}} = \sigma_n \boldsymbol{E} \tag{2.7}$$

where $\boldsymbol{E}$ is the electric field strength and σ_n is the electrical conductivity, $\sigma_n = ne\mu_n$ for free electrons with density n, e is the charge per electron and μ_n is the electron mobility. The electron drift current can also be written as

$$\mathbf{J_{dr}} = ne\boldsymbol{v}_{dr} \tag{2.8}$$

where $\boldsymbol{v}_{dr}$ is drift velocity of carriers. Comparing both equations (2.7) and (2.8), at low electric field the drift velocity of carriers is proportional to the field strength and the proportionality constant is the mobility [13]. It is defined as

$$\boldsymbol{v}_{dr} = \mu_n \boldsymbol{E}. \tag{2.9}$$

The mobility is influenced mainly by scattering due to phonons and ionized impurities inside the crystal [23]. In general, as the impurity concentration increase, the mobility decreases and can be also written as

$$\mu_n = \left(\frac{e}{m_n^*}\right)\tau_{sc} \tag{2.10}$$

where m_n^* is the effective mass of the electron and τ_{sc} is the scattering relaxation time for electrons, the average time between electron scattering events.

Another parameter associated with mobility is carrier diffusion coefficient. For non-degenerated semiconductor, the electron diffusion coefficient is given by

$$D_n = \left(\frac{kT}{e}\right)\mu_n \tag{2.11}$$

where k is Boltzmann constant and kT is the thermal energy in eV. The electron diffusion current then can be expressed as

$$\mathbf{J_{df}} = eD_n \boldsymbol{\nabla} n. \tag{2.12}$$

2.4.2. Lifetime

The conductivity for both charge carriers in semiconductors in the dark is given by

$$\sigma_0 = e(n_0\mu_{n0} + p_0\mu_{p0}) \qquad (2.13)$$

where n_0 and p_0 are the densities of free electrons and holes, respectively, and μ_{n0} and μ_{p0} are the electron and hole mobilities. Again, let's consider only the electrons.

In a homogenous material in which n_0 is uniform throughout the material, conductivity increases by the photoconductivity $\Delta\sigma$ when absorbed illumination increases the value of electron density by Δn or the value of electron mobility by $\Delta\mu$

$$\sigma_L = \sigma_0 + \Delta\sigma = (n_0 + \Delta n)e(\mu_0 + \Delta\mu). \qquad (2.14)$$

Then

$$\Delta\sigma = e\mu_0\Delta n + (n_0 + \Delta n)e\Delta\mu. \qquad (2.15)$$

It is generally true that

$$\Delta n = G\tau \qquad (2.16)$$

where G is the photoexcitation rate ($m^{-3}s^{-1}$) and τ is the electron lifetime so that

$$\Delta\sigma = e\mu_0 \mathrm{G\tau} + ne\Delta\mu, \qquad (2.17)$$

where $n = n_0 + \Delta n$. Let's point out that the increase in carrier mobility $\Delta\mu$ in monocrystalline material can be caused by change in charged impurities scattering under the illumination either through a change in density of such charged impurities or through a change in the scattering cross section of such impurities [22].

In the case of semiconductors at a reasonably high photoexcitation rates, $\Delta n >> n_0$, it may be defined a 'figure of merit' for single-carrier photoconductor as

$$\frac{\Delta\sigma}{Ge} = \mu\tau. \qquad (2.18)$$

Thus the 'mobility-lifetime' product is a quantity of the photoconductor's sensitivity to photoexcitation.

The τ in eq. (2.18) is the free lifetime [23] of electrons. It is a time that the charge carriers are free to contribute to the conductivity. The free lifetime of charge carriers can be terminated by recombination or by extraction from the crystal by the electric field without replenishment from the opposite electrode. If the carrier is extracted from the crystal by the field at the same moment as an identical carrier is injected into the crystal from the opposite electrode, then the free lifetime is undisturbed. In addition, the lifetime can be interrupted by trapping of charge carriers and then be resumed after the detrapping.

2.4.3. Charge carriers trapping

If the semiconducting material exists without any trapping energetic levels inside the band gap then every excited carrier in the crystal would be a free carrier. However, in the case of real materials, the trapping centres and recombination centres are present inside the crystal and thus the number of free carriers n can be less than the number of excited carriers.

In one way, this effect can be considered through a ‘drift mobility’ μ_d by

$$(n + n_t)\mu_d = n\mu, \tag{2.19}$$

where n_t is the density of trapped carriers. Thus the observed conductivity for the density of free electrons moving with the mobility of free electrons is equal to the conductivity which would be expected if all the excited electrons moved with the drift mobility. If there is no trapping inside the crystal, then the drift mobility will be the same as normal mobility.

The drift mobility can be measured by directly timing the transit of charge carriers over a known distance. Such a measurement is generally called Time of Flight (ToF) method. ToF can be specified by the quantities that are measured: a) if the transient of charge is measured, then it is called transit charge technique (TChT), b) if the transient of current is measured, then ToF is called transient-current-technique (TCT).

3. General experiments used for detector characterization

3.1. Current-voltage characteristics

The detailed current-voltage characteristics are measured in apparatus presented in Fig. 3.1. This apparatus allows to measure planar detectors and also detectors with guard-ring structure (see chap. 2.2.1). In both cases, full planar electrode is biased by Keithley 2410 sourcemeter. In the planar configuration, the current I_1 is obtained on the opposite electrode and is derived from the measured voltage V_1 by Keithley 2000 multimeter on load resistor R_{L1} with resistance of 100 MΩ as

$$I_1 = \frac{V_1}{R_{L1}} \tag{3.1}$$

while the *jumper* depicted in the Fig. 3.1 is opened.

In the case of guard ring structure, the values of bulk current (I_1) and surface current (I_2) are measured separately on two distinct load resistors R_{L1} and R_{L2} with the same resistance of 100 MΩ. The example of measurement with guard ring structure is shown in Fig. 3.1 where the *jumper* component has to be closed.

The sample is placed in non-transparency ferromagnetic shielding during the measurement to avoid interference with external sources, mainly with external light.

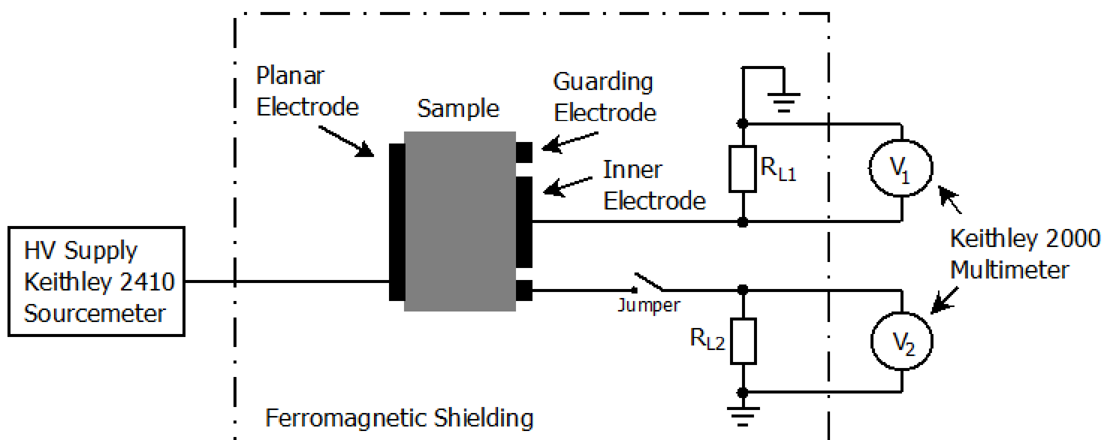

***Fig. 3.1** Setup for measuring of current-voltage characteristic for planar detectors and detectors with guard ring structure.*

3.2. Radiation spectroscopy

For radiation detector applications, there are three general modes of detectors operations. They are called *pulse mode*, *current mode* and *mean square voltage mode* [32]. Pulse mode has several inherent advantages over the two other modes [32]. In this mode, the measurement instrumentation is designed to record each individual quantum of radiation that interacts in the detector. It is usually represented by the time integral of each burst of current or the total charge Q, since the energy deposited in the detector is directly related to Q. The one benefit is the much higher sensitivity which can be achieved. It is usually many orders of magnitude higher than in current mode or mean square voltage mode because each individual quantum of radiation can be detected as separate pulse. But the more essential advantage is that each individual pulse amplitude contains some information. In the other two modes, this information on individual pulse amplitude is lost and all interactions, regardless of amplitude, contribute to the average measured current. Therefore in nuclear instrumentation the pulse mode is the most used pulse-processing technique.

When radiation detector operates in pulse mode, the large number of pulses varies in amplitudes. These variations in amplitudes could be caused by differences in the radiation energy or by fluctuations in the inherent response of the detector to monoenergetic radiation. The pulse amplitude distribution is the fundamental property of the detector output that is routinely used to deduce information about the incident radiation or the operation of the detector itself. The most common way to display pulse amplitude information is through the differential pulse height distribution [32].

In many application of radiation detectors, the objective is to measure the energy distribution of incident radiation – *radiation spectroscopy*. Energy spectrum can be determined from differential pulse height spectra by *pulsar calibration* of used spectroscopic apparatus.

The fundamental output of all pulse-type radiation detectors is a burst of charge Q created by a single incident radiation quantum in the detector. The charge Q is usually proportional to the deposited energy and is delivered as a transient current $I(t)$, where Q is the time integral of current pulse. With a continued exposure to a radiation source, the input to the pulse processing system is a series of these transient charge pulses, occurring at random times and usually with varying amplitudes and durations. The pulse processing system require accumulation of multiple events that are the

results of interactions of many individual incident quanta over a given measurement time.

In laboratory of IoP CU, the standard measuring apparatus for spectroscopy measurement consists of shielding vacuum chamber Canberra, home-made preamplifier based on Amptek A250 amplifier, shaping amplifier Ortec 671, multichannel analyser (MCA) Ortec MCA easy 8, evaluation program Maestro 32 and by high voltage supply Iseg SHQ 122M. The schema of spectral apparatus is illustrated in Fig. 3.2 where the output illustrated on MCA is recorded by Maestro 32 program as a function of counts per channel. The distinct channel corresponds to distinct energy via calibration.

The semiconducting planar detector sample is placed inside the measuring apparatus where one electrode is always grounded and the other is biased by Iseg SHQ high voltage source. The point source of radiation is placed on the cathode side. The incident radiation generates (e–h) pairs which are separated in applied bias and are drifted towards the relevant electrodes. The charge carriers movement is reflected as a current impulse ($I(t)$). The total charge is usually too small to be sensed directly. Therefore the impulse is sent to a preamplifier, an interface between the detector and the subsequent processing electronic. The preamplifier has a charge sensitive configuration, integrating the transient current pulse to produce a voltage step V_{max}

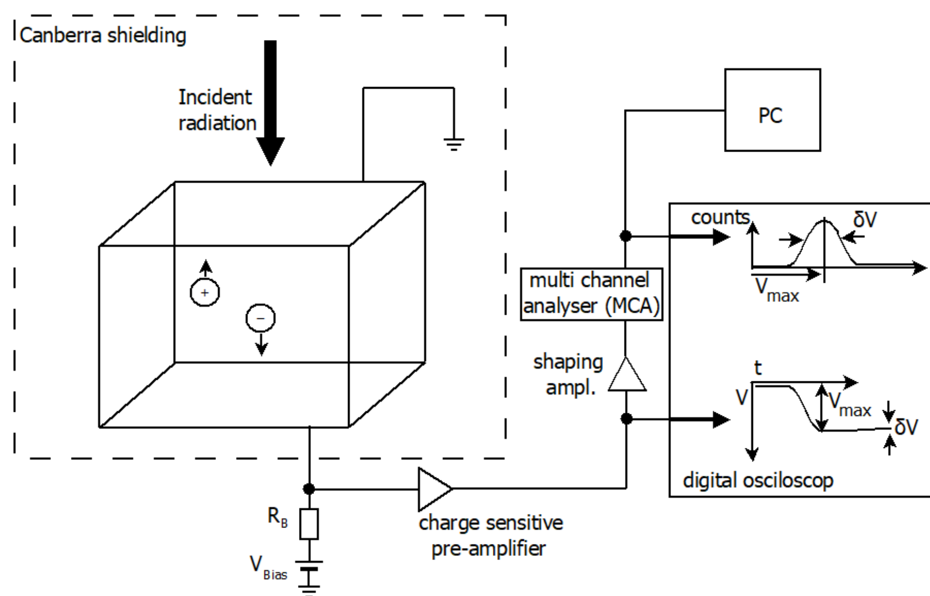

Fig. 3.2 *Scheme of apparatus for measuring radiation spectra.*

proportional to Q. The shaping amplifier converts the preamplifier output signal into a form suitable for MCA, producing an output voltage pulse with pulse proportional to the deposited charge Q. This voltage pulse is readout in MCA as it is shown in Fig. 3.2. The output of the shaping amplifier returns rapidly to the baseline to prevent pulses from overlapping and resulting distortion of the measurement. Since the size of Q reflects the energy deposited by the incident quantum in the detector, recording the pulse height distribution is a good method to provide information about the energy distribution of the incident radiation.

3.2.1. Pulse height spectrum analysis

Individual types of energy emitters used in our laboratory are depicted in the Table 3.1. The table contains type of radiation, main line energy and activity of those emitters. The applied biases for pulse height spectrum analysis are usually in range from +800 V to -800 V.

In the case of homogenous linear electric field inside the detector the parameter $\mu\tau$ can be determined via Hecht equation [33]:

$$CCE = \frac{Q_m}{Q_0} = \left\{\frac{v_h \tau_h}{L}\left(1 - \exp\left[\frac{-x_i}{v_h \tau_h}\right]\right) + \frac{v_e \tau_e}{L}\left(1 - \exp\left[\frac{x_i - L}{v_e \tau_e}\right]\right)\right\}, \quad (3.2)$$

where CCE is charge collection efficiency, $v_{h,e}$ is velocity of holes/electrons, $\tau_{h,e}$ is lifetime of holes/electrons, L is the width of the sample and x_i is the position inside the sample where the incident radiation is absorbed.

If the radiation source is alpha-^{241}Am and the incident particles are absorbed within a few micrometres inside the sample under irradiated cathode [34] then the value of x_i can be set as zero. If it is also used of

$$v = \mu E \qquad \text{and} \qquad E = V/L, \quad (3.3a,b)$$

then it can be obtained the simple one carrier (electrons in this case) Hecht equation as

$$CCE = \frac{Q_m}{Q_0} = \left\{\frac{\mu_e \tau_e V}{L^2}\left(1 - \exp\left[\frac{-L^2}{\mu_e \tau_e V}\right]\right)\right\}. \quad (3.4)$$

Source	Type of radiation	Main line energy	Activity
^{241}Am	α – alpha	5.5 MeV	8,5 kBq
^{241}Am	γ – gamma	56.9 keV	89 kBq
^{67}Co	γ – gamma	132 keV	150 kBq
^{137}Cs	γ – gamma	662 keV	87 kBq

Table 3.1 *Types of radiation sources.*

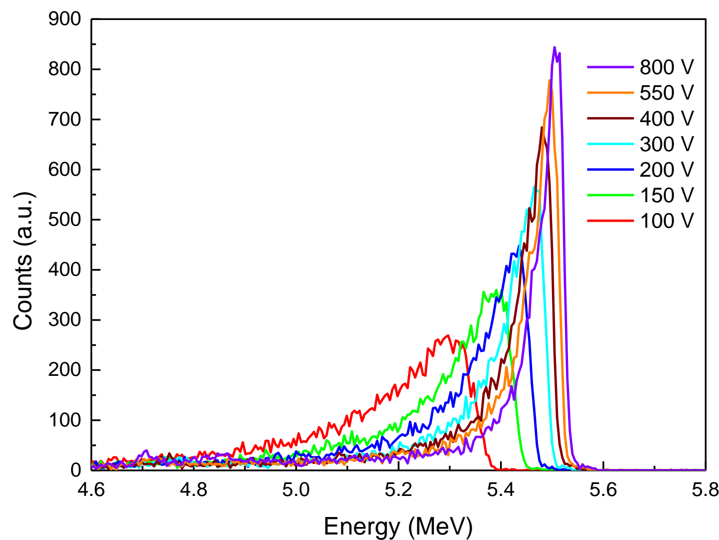

Fig. 3.3 *Common spectrum of α-^{241}Am for selected applied biases in range of 100 V to 800 V obtained with CZT detector.*

The value of the fitted parameter μτ can be determined by fitting of the *CCE* dependency on the applied bias *V* by the equation (3.4).

Common alpha spectrum for different applied biases is shown in Fig. 3.3. The graph shows that for higher applied bias the peak positions moves to the right, towards the higher energy. Otherwise, the charge collection of the generated charge carriers is higher with the strongest electric field inside the sample. The central position of the obtained peaks depending on applied bias is plotted in Fig. 3.4. For a given width of the sample, it is possible to determine the μτ product value by fitting this dependency with the simple Hecht equation (3.4). The fitted value of μτ product in Fig. 3.4 is equal to $9.4{\cdot}10^{-3}$ cm^2/V. The similar analysis can be done in gamma spectroscopy using gamma radiation emitters. Spectrum for γ-^{241}Am for different applied biases is shown in Fig. 3.5.

One important property of the detector in radiation spectroscopy is its response to a monoenergetic source of radiation. Hence from the obtained spectrum it can be determined the energy resolution of the given detector which is defined as [41]

$$\text{Resolution } R_\gamma = \frac{FWHM}{E_\gamma}\ \% \tag{3.5}$$

where *FWHM* is the full width at the half maximum of photopeak obtained by an energy of the monoenergetic source of radiation E_γ.

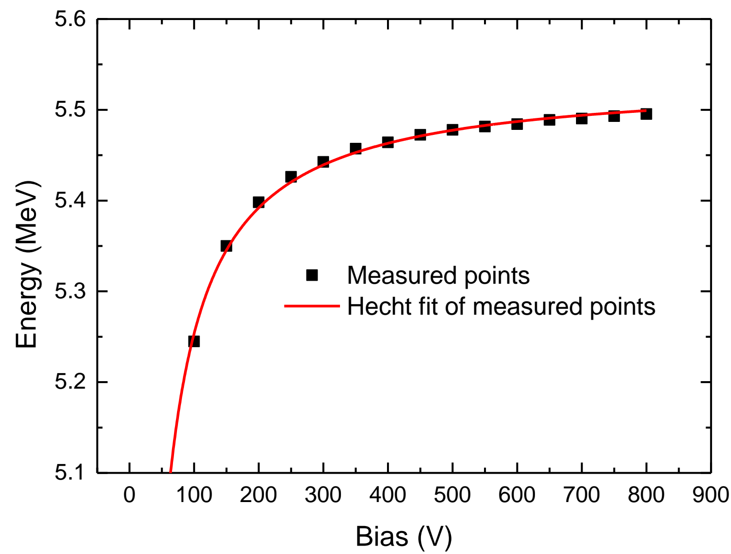

Fig. 3.4 *Determination of Hecht relation for α-^{241}Am.*

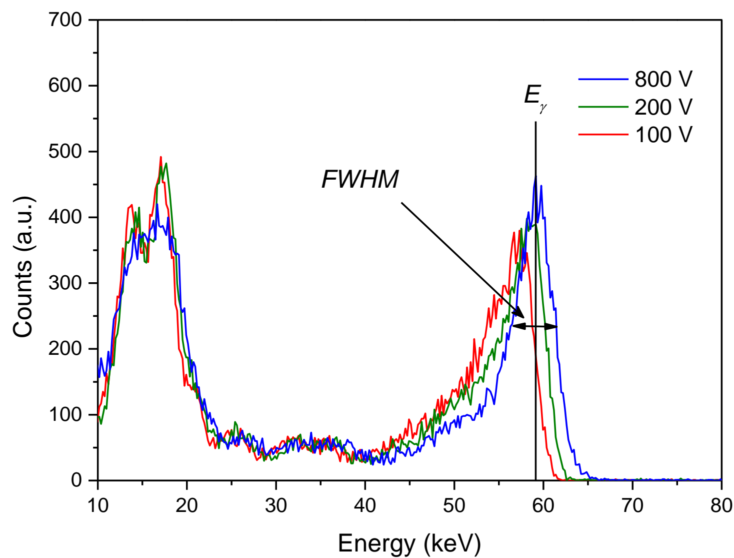

Fig. 3.5 *Common spectrum of γ-^{241}Am for selected applied biases in range of 100 V to 800 V obtained with CZT detector.*

3.2.2. Transient charge technique

Transient charge technique (TChT) is a very useful tool to measure charge transport of semi-insulating radiation detectors, as it relies on the operation principle of these devices. From transients, carrier collection times can be accessed and therefore carrier mobility calculated [36].

For this method ^{241}Am alpha particle source is used to generate e-h pairs which create electronic input signal. The readout electronics of the TChT consists of a low noise input FET transistor and a very fast integration amplifier with a buffer (see Fig 3.6). The output pulse from the amplifier is directly recorded by the ultrafast digital sampling oscilloscope (LeCroy WaveRunner 640Zi, 40 Gs/s, vertical resolution up to 11 bits, 4 GHz bandwidth) for further computer processing. Again Iseg SHQ 122M is used as a bias source.

Combining the eq. (2.9) and (3.3b) the simple relation for homogenous sample without space charge is given as

$$\mu = \frac{L^2}{t_r V} \tag{3.6}$$

gives the value of electron mobility for given bias *V*. The transit time t_r is represented by the electrons drifting from irradiated cathode through the detector of width *L* to reach the anode.

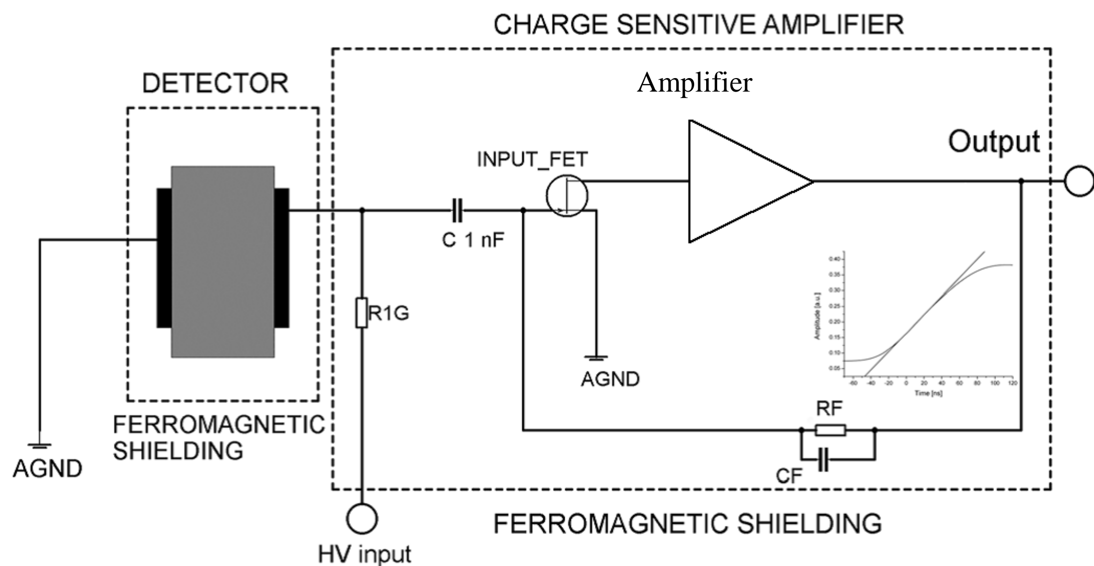

Fig. 3.6 *Transient charge technique experimental setup with a typical transient charge output pulse in the inset graph.*

3.3. Transient-current-technique

Transient-current-technique (TCT) is another ToF method. The basic ideas of the TCT technique for the study of transport phenomena in semiconductors was first presented by Haynes and Shockley [37]. The most important measured parameter is again transit time t_r. It is a time taken by charge carriers to travel across a given region of the sample under the influence of a known electric field [38].

3.3.1. Principle of transient-current-technique

The schematic principle of TCT is illustrated in Fig. 3.7. For a very short period, an ionizing radiation with small penetration depth (alpha particles in this case) creates electron-hole pairs under the contact of ideal semiconductor detector. Let's consider the radiation intensity small enough and all additional space-charge effects let's be avoided. Due to the applied bias on the sample, an electric field is presented inside the sample and enables one type of charge carriers (electrons in case of Fig. 3.7) to travel across the sample. The other carriers – holes are almost immediately swept towards the cathode. Electrons travelling across the whole region L will induce a current transient signal (Fig. 3.8 red curve) in an external circuit which is connected with the sample. The duration of the signal t_r is exactly the same as the time carriers need to move through the region L. The current transient signal induced by the motion

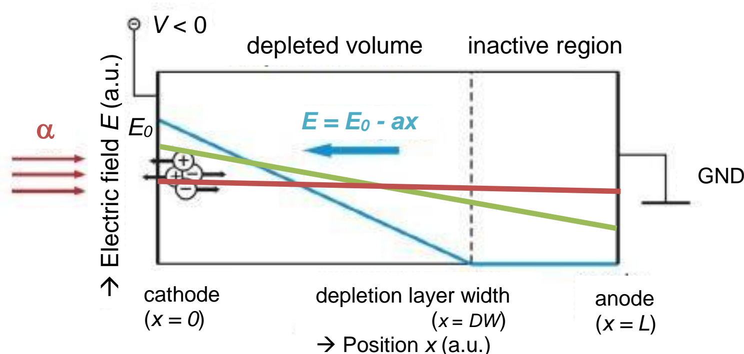

Fig. 3.7 *Schematic of the TCT. An ionizing radiation creates charge pairs in a narrow region close to one contact. Red, green and blue lines represent the linear profile of the electric fields in a detector; green and blue lines are profiles with positive accumulated charge.*

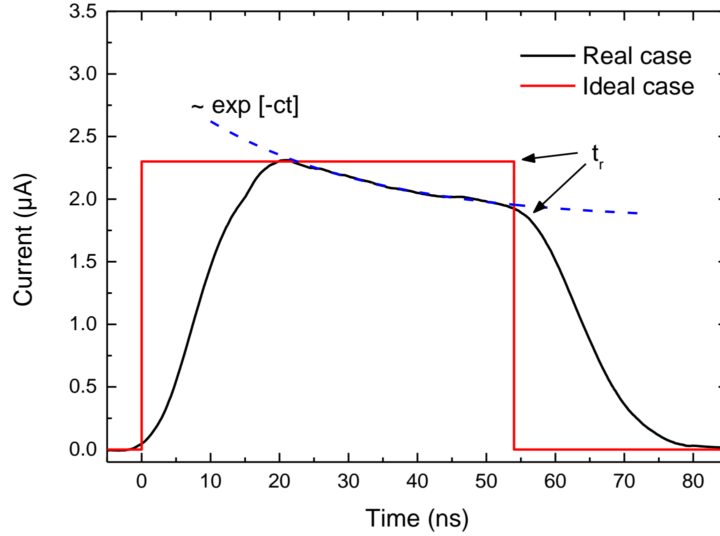

Fig. 3.8 *Current signal induced by the carriers drifting across the sample.*

of charge carriers can be calculated under the following conditions:

$$\tau_g \ll t_r, \tau \gg t_r \text{ and } \tau_\epsilon \gg t_r \tag{3.7}$$

where τ_g is time of electron-hole pair generation, τ is a lifetime of the mobile carriers and $\tau_\epsilon = \rho\epsilon_0\epsilon_r$ is dielectric relaxation time of given material (ρ is resistivity, ϵ_0 is vacuum permittivity and ϵ_r is relative permittivity of the material). The amplitude of the current pulse $I(t)$ induced by number n of carriers drifting across the sample is given as [38]

$$\begin{aligned} I(t) &= \frac{ne}{t_r} \quad 0 \le t \le t_r \\ I(t) &= 0 \qquad t \ge t_r. \end{aligned} \tag{3.8}$$

The duration of the current transient signal is exactly equal to the time required for carriers to drift across the whole L region and the drift velocity v_d is simply given by

$$v_d = \frac{L}{t_r}. \tag{3.9}$$

It is evident, that in principle, this technique enables to study charge pulses formed by the drifting of each type of carriers separately in the same sample. This can

be easily achieved by reversing the applied bias polarity V or by irradiating the opposite contact.

The current waveforms (CWFs) observed in experiments can be different from the ideal ones predicted by eq. (3.8) and represented in Fig. 3.8 by the red curve. The following events can occur and disturb the ideal CWFs [38]:

a) a non-uniform electric field is presented in the sample, particularly when the examined device is Schottky or p-n junction;
b) space-charge effects are presented when the density of the carriers generated by the ionizing radiation is so high that the electric field inside the sample is strongly disturbed;
c) trapping and detrapping effects are presented;
d) thermal diffusion phenomena are presented.

The real CWF is represented by black curve in Fig. 3.8. At the beginning of CWF the Plasma effect takes place. The plasma effect was discussed in detail in [8], [39] and its main manifestation is the expansion of the leading edge of the pulse. Supposing that 5.5 MeV alpha particle is absorbed at 10-20 μm under the irradiated contact then charge cloud over 10^6 e-h pairs (plasma) is created in this area (the creating energy for one e-h pair in CZT is 4.7 eV). These carriers are subject to an electric field in a detector, hence, this high conductivity plasma disturbs for some time (plasma time or plasma-decay time) the internal electric field and therefore retards the charge collection. As it was proven in [8] drift dominates over diffusion in a direction perpendicular to the detector's contacts and thus, the initial acceleration of carriers and the erosion of the charge cloud is caused by the electric field in a sample. Also in [8] was concluded that the plasma effect can be strong enough to delay signal formation and that this charge cloud causes the screening of an applied bias. For higher bias voltages, the plasma effect becomes less important and sometimes it can be suppressed overall. The middle part of CWF represented by exponential decay from 20 ns to 58 ns in Fig. 3.8 is given by current induced inside the detector by electrons drifting towards the anode. At the time of t_r the major part of electrons is collected at the anode. A gradual decrease of CWF after t_r represents the collecting of trapped and subsequently detrapped carriers from energetic levels inside the bandgap and electrons delayed by plasma effect.

3.3.2. Theory of transient-current-technique

The whole theory of TCT is well described in [8] or [40], therefore, there is only a brief summary.

Several measurements [8], [41], [42] approved that a constant space-charge density ρ_{SC} (positive or negative) anticipates in both CdTe and CZT radiation detectors.

$$\rho_{SC} = \text{const.} \tag{3.10}$$

Under the condition (3.10) and by the involving of free carriers losses due to trapping in deep defects, the electric field strength, $E(x)$, at the distance x from the irradiated electrode can be expressed as

$$E(x) = E_0 - ax \tag{3.11}$$

where a is the linear slope of the electric field and the constant term E_0 is an electric field under the irradiated electrode. The slope of the electric field is induced by the space-charge density N via

$$a = \frac{eN}{\epsilon_0 \epsilon_r} \tag{3.12}$$

where ϵ_0, $\epsilon_r = 10.3$ are the vacuum- and relative-permittivity for CdTe/CZT, respectively, and e is the elementary charge. If the positive space charge is assumed, then $a > 0$. The current induced inside the detector

$$i(t) \approx e^{-ct} \tag{3.13}$$

can be fitted from the experimental data as it is seen in Fig. 3.8 – black curve represents the real CWF and the blue dash curve is exponential decay fit. The parameter c is then given as

$$c = \left(a + \frac{1}{\mu\tau}\right)\mu. \tag{3.14}$$

By a theory of p-n junction, the depletion width DW of the detector's volume with space-charge density N can be calculated as

$$DW = \sqrt{\frac{2\epsilon_0\epsilon_r V}{eN}} \leq L, \tag{3.15}$$

where V is the applied bias. It is clear that two situations can occur:

i) For $DW < L$, the electric field is screened completely near the anode, wherein an inactive region with a zero electric field appears (see Fig. 3.7 – blue curve).

ii) For $DW = L$, the electric field is nonzero within the entire volume of the detector and the inactive region does not exist.

In the second case, the arrival of drifting electrons to the anode is identified by a clear drop of current transient (see Fig. 3.8 – black line) which allows to determine the transit time t_r. Such a drop is not visible in case when the inactive region is formed inside the sample.

For parameters obtained by experiments (c, t_r and $\mu\tau$), the parameter a can be numerically solved from transcendental equation [8]:

$$ct_r = \left(1 + \frac{1}{a\mu\tau}\right) \ln\left(\frac{1 + \frac{aL^2}{2V}}{1 - \frac{aL^2}{2V}}\right). \tag{3.16}$$

Consequently, all the model's parameters a, E_0 and μ can be determined for all measured CWFs.

As it is written above, if the applied bias is low and the electric field is completely screened near the anode, an inactive region appears under that electrode, and then the transit time is undefined. The information offered by the experiment is insufficient to the determination of all model's parameters. It may be, however, taken the advantage of the bias-independent value of μ determined from the analysis of current pulses at high bias and insert it into eq. (3.14) to calculate the linear slope a of the electric field.

3.3.3. Alpha-induced transient-current-technique setup

One part of the Result section is about modification of TCT apparatus as well as representation of obtained results by this method. Therefore here is given an example of simple setup using the alpha particle source for electron-hole pairs generation. The modification and comparison to other methods is written in chapter 6 “Transient-Current-Technique as a powerful tool for detail detectors characterization”.

The TCT setup (see Fig. 3.9) is based on the direct amplification of the detector current pulse corresponding to the collected charge in the detector volume flowing through the input stage (input impedance internally) of the very high frequency bipolar amplifier (Miteq AM1607–3000R, 40 dB gain, 3 GHz radiofrequency amplifier). The output pulse from the detector is AC coupled to the amplifier input and Schottky diodes connected in parallel are used for protection. The output pulse from the current amplifier was directly recorded by the ultrafast digital sampling oscilloscope (LeCroy WaveRunner 640Zi, 40 Gs/s, vertical resolution up to 11 bits, 4 GHz bandwidth) for

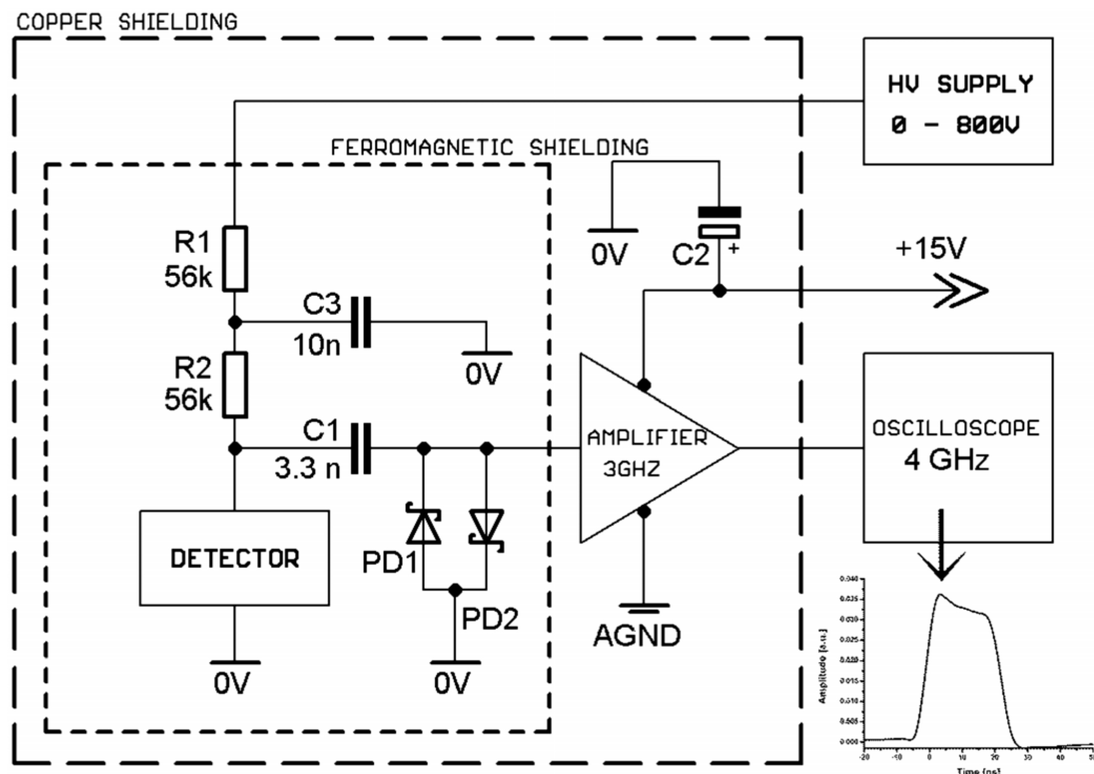

Fig. 3.9 *Alpha-induced transient-current-technique experimental setup with a typical transient current output pulse in the inset graph.*

further computer processing.

For this methods ^{241}Am alpha particles are used to generate electron-hole pairs. Low noise high voltage power supply Iseg SHQ 122M is used for the detector biasing usually from 0 V to -800 V. As one could expect, the detected pulse amplitude is substantially weak and much noisy. Data accumulation (several thousands of pulses) with computer filtering, precise oscilloscope trigger setup and efficient high frequency noise double shielding are inevitable prerequisites to obtain plausible results.

3.4. Ellipsometry

Ellipsometry is an optical technique allowing to derivate optical properties of given material as well as the surface layer thickness [43]. By commercial Mueller matrix ellipsometer J.A.Woollam RC2 it is possible to measure changes in light polarization after reflection on the sample. The light energy of given ellipsometer ranged from 1.2 eV (~ 1050 nm) to 4 eV (~ 300 nm). The change in polarization is represented by ellipsometric angles Ψ and Δ which are related to the Fresnel reflection coefficients for p– and s–polarization as

$$\delta = \frac{r_p}{r_s} = \tan(\Psi) \cdot e^{i\Delta}. \tag{3.17}$$

Parameters Ψ and Δ are influenced by surface conditions, layers thickness and dielectric function of specific material. With the theoretical model of Effective Medium Approximation (EMA) which is described in [44] or [45] it is possible to derive spectrally dependent optical properties of studied material and the thickness of the surface oxide layer.

3.5. Pockels effect measurement

Experimental apparatus for Pockels effect measurement (Fig. 3.10) uses as its name suggests the Pockels effect.

It is a standard and widely-used method [41], [46]–[51], which allows to study samples under various excitation conditions. Pockels effect is a linear electro-optical effect, when after attaching the electric field $\vec{\boldsymbol{E}}$ on the semiconductor, a change in the

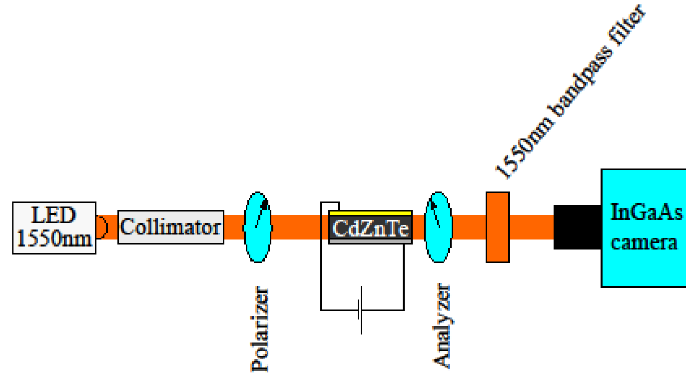

***Fig. 3.10** Pockels effect apparatus for steady state measurements.*

electrical components of the impertivity tensor $\boldsymbol{\eta}$ occurs. Therefore, the refraction index n is changed as well. From the symmetry of $\boldsymbol{\eta}$, from the mutual dependencies of its individual elements, and from the crystal symmetry of CdTe/CZT it results that there is only one non zero element in the impertivity tensor $\boldsymbol{\eta}$ [52]. Therefore after the electric field attachment the isotropic material becomes birefringent and the refraction index is linearly dependent on the attached field as

$$n_{x,y}(E) = \mathrm{n}_0 + \frac{1}{2\sqrt{3}} r_{41} n_0^3 E \tag{3.18}$$

$$n_z(E) = \mathrm{n}_0 - \frac{1}{2\sqrt{3}} r_{41} n_0^3 E \tag{3.19}$$

where n_0 is refraction index of isotropic material and r_{41} is Pockels coefficient for CdTe/CZT material.

In our setup on Fig. 3.10 the collimated monochromatic low intensity light beam (1550 nm, ~0.8 eV), called Pockels light, passes through the biased sample (by high voltage supply Iseg SHQ 122M) placed between two orthogonal linear polarizers. In this configuration, the spatial distribution of the transmittance T (x, y) of the above-described system (monitored by an InGaAs camera) depends on the electric field distribution E (x, y) in the sample as

$$T \sim \sin^2 E. \tag{3.20}$$

3.6. Infrared microscopy

Since the defects in the CdTe/CZT samples absorb the near IR radiation and form the dark entities in the images, IR microscopy is very suitable for characterization of defects with the size above 1 μm.

Optical inverted microscope OLYMPUS IX70 is used for investigation of defects inside the semiconducting samples. The halogen lamps is used as a source of the light for sample illumination. The infrared (IR) light passing through the sample is detected by CCD camera with low signal to noise ratio at 50 dB. The microscope imaging works with the near IR radiation at wavelength λ ~ 900 nm. The picture can be magnified by 3 objectives OLYMPUS RMS 4x, 10x and 20x. The highest resolution of this optical system (for 20x objective) is ~ 1.4 μm [31].

Results

The emphasis of this dissertation thesis has been focused on the characterization and description of CdTe/CdZnTe based detectors through experimental techniques. The focus of Results chapter is to report the experimental results that were obtained on several detectors and to provide explanations for these results. The chapter 4 analyses the surface treatments and their influence on the final detector (e.g. energy resolution). The chapter 5 reports of infrared LED enhanced spectroscopic CdZnTe detector working under high fluxes of X-rays. The chapter 6 displays the adaptation of TCT measurements on characterization of CdTe/CZT detectors and shows the advantages of this method (e.g. electron mobility determination) compared to the other experimental techniques. The chapter 6 have more or less character of basic research. On the contrary, the other two mentioned chapters show the direction of possible application use. For example, the results from the 5th chapter have a high application potential in modern medicine as it was reported in [53].

4. Surface treatments on CdTe/CdZnTe radiation detectors

Surface treatments are one of the main problems in the development of high performance detector. In this chapter, the focus lies on study of different surface treatments and their influence on final detector performance.

During the cutting of the detector samples from the crystal ingot, the surface of CdTe/CdZnTe is often damaged and surface states and residues are created. It is necessary to improve surface treatments to dispose of the surface states. This surface states produce defects which give a rise to the leakage current that negatively disturbs the detector spectral resolution and CCE [1]. Different surface treatments of the CdTe/CdZnTe detectors can lead to a different surface leakage currents [26], [56], [57]. It has been previously published that the surface treatments on the lateral sides may significantly affect the detector performance [57]–[59]. So the amount of the collected charge depends not only on homogeneity of the single crystal, but also on the surface treatments and metal contacts preparation. It has to be point out, that the

leakage current also affects electronic components of the measuring apparatus and contributes to the noise of used electronics (e.g. amplifier) [60]. It has been previously reported that during measurements with the bias applied to the sample, only a minor part of the current passes through the bulk (about 1 – 5 %) [26] and the rest of the current flows over the surface as the surface leakage current.

Additional factor limiting the CCE is the detector polarization due to the space charge formation on deep level traps in the detector's volume [8]. In this case the screening of an applied bias can occur which cause a creation of an "inactive" region with zero electric field close to the contact [8], [61]. The formation of deep level traps is again influenced by the metal contact preparation [62], [63]. Therefore it is necessary to create long-term stable contacts without the presence of the detector polarization. In an ideal case, the type of contact is determined by the difference between metal and semiconductor work functions (see chapter 2.2). Ohmic contacts exhibit lower polarization of detectors, but can cause a higher dark current compared to Schottky contacts and vice versa. In a real case, the barrier height is formed by the work function of the metal and the surface states of semiconductor also known as an interlayer. The interlayer (surface states) between metal and semiconductor (MIS structure) also affects the properties of the detector because it determines the resulting type of contact.

Various surface treatments of CZT crystals leading to the leakage current reduction have been previously reported in [26], [64], [60], [65]–[67]. Chemical etching produces dangling bonds and non-stoichiometric surface species [68], [69] that are responsible for high values of surface leakage current. To prevent this effect, passivation of the semiconductor is usually applied to decrease the surface leakage current and by this means to increase the detector performance. As a good passivation reagents for CZT, solutions of NH_4F/H_2O_2 [65], [70] and KOH [66] were identified in several studies. Those two solutions create different oxides on the crystal surface which passivate it. The X-ray photoelectron spectroscopy (XPS) used for chemical analysis of the surface passivation by NH_4F/H_2O_2 is reported in [65] and [66]. The conclusion is that this passivation creates surface layer primarily of TeO_2. On the other hand the KOH passivation should create Cd-rich surface on CZT as it was reported in [66].

However, the published results did not present a clear conclusion about an optimal surface treatment process from the detector performance viewpoint. In this

chapter we present various surface etching types and a passivation treatment study before metal contact preparation with emphasis on the time stability of such prepared detectors. The current voltage characteristics, gamma-ray pulse height spectrum analysis, the internal electric field profiles and ellipsometry are used to characterize the quality of the prepared detectors (mainly the magnitude of leakage current).

4.1. Samples preparation

For this study, five samples were used. It were used two neighbouring samples from the indium doped CdTe wafer grown in our laboratory at Charles University by the vertical gradient freeze method [71]. The other three samples comes from commercial indium doped $Cd_{0.85}Zn_{0.15}Te$ material provided for academic research also grown by the vertical gradient freeze method. The samples were not crystallography oriented and the dimensions were $5 \times 5 \times 2$ mm^3. Sample's labels and their resistivity is shown in Table 4.1. Resistivity was measured by modified contactless resistivity measurement (COREMA) setup, described in detail in [44], [72].

As the initial surface treatment, samples were mechanically grinded using SiC abrasive of different sizes of the abrasive grains, in sequence SiC 600, 1000 and 1200. The higher the number of abrasive is, the finer grain size it has. After the mechanical grinding the samples were chemically etched by immersion into 3% bromine-methanol solution for 2 minutes – (**BM**) method. (**BM**) etching was followed by sample rinsing – twice in methanol and once in isopropyl alcohol, and all samples were dried with purified air. It is a standard approach usually used in our laboratory which is also proposed by several studies, e.g. [73].

Sample label	**Resistivity [Ω·cm]**
CdTe-I	$9.1 \cdot 10^{9}$
CdTe-II	$7.8 \cdot 10^{8}$
CZT-I	$1.3 \cdot 10^{10}$
CZT-II	$8.2 \cdot 10^{10}$
CZT – Sample C	$1.0 \cdot 10^{10}$

Table 4.1 *Labelling of samples for surface treatment study and their resistivity obtained by contactless resistivity measurement (COREMA)*

Subsequently the following surface treatment procedures were used:

- Chemo-mechanical polishing in 3% bromine-ethylene glycol solution (**BE**) made on a polishing kit on a silk pad. To achieve the same quality on each side of the sample, polishing takes 30 seconds per side. Additional sample rinsing was done twice in methanol and once in isopropyl alcohol and it was dried with purified air.
- After (**BE**) treatment, the sample was further etched for about 30 seconds in a 3% bromine-methanol solution - (**BEBM**) treatment. The rinsing of the sample was same as for (**BM**) treatment.
- Passivation with 25 ml of 10%wt NH_4F 10%wt H_2O_2 aqueous solution. CZT sample was immersed in the solution for 5 min (**NHF**). After the immersion the sample was bathed three time in distilled water and was dried with purified air.
- Passivation in 50% potassium hydroxide (**KOH**) solution for 1 min. When passivated, the sample was rinsed three times in distilled water and dried with purified air.

As it was previously reported, electroless contact deposition creates strong chemical bonds between metal and semiconductor [62], [74] and gold creates quasi-ohmic contact on CZT [75]. Hence, after performing one of the listed surface treatments gold contacts were electrolessly deposited from a 1% $AuCl_3$ aqueous solution to the both largest sides of the detector.

Samples were mechanically polished before each individual treatments listed above in order to remove the previous surface layer and to prepare the same starting surface quality. The surface treatments were performed on all samples in random order to avoid some crystal property change due to the process induced damage.

4.2. Surface effect on current-voltage characteristics and pulse height spectrum analyses

Spectra of ^{241}Am gamma source were measured by standard spectroscopic apparatus described in chapter 3.2. CdTe/CZT detector was placed inside a Canberra shielding box with a 59.6 keV ^{241}Am gamma-ray source at the distance of 2 cm. The Iseg SHQ 122M voltage supply is used for detector biasing in the range of +800 V to -800 V. The current voltage characteristics which in particular show the leakage current values [26] were recorded by apparatus described in chapter 3.1.

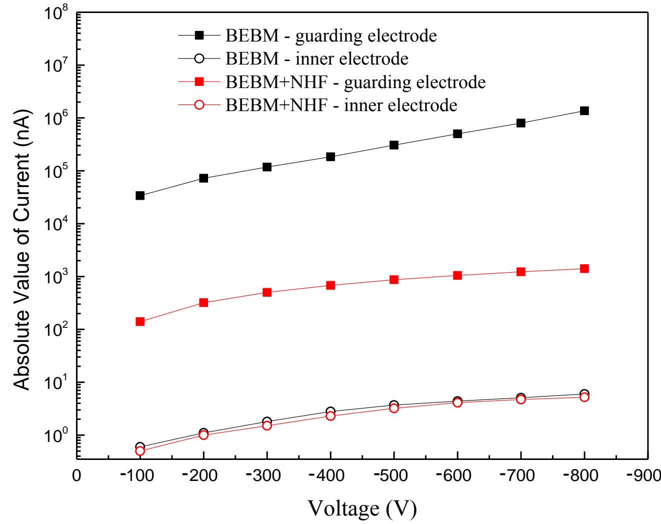

Fig. 4.1 *Current-voltage characteristic of CdTe-II sample with the guard ring structure before (**BEBM**) and after (**BEBM+NHF**) surface passivation in* NH_4F/H_2O_2.

The influence of NH_4F/H_2O_2 passivation on the sample CdTe-II ($\rho = 7.8 \cdot 10^8$ Ω·cm) with a guard ring structure (see Fig. 2.6) was investigated. The guard ring had a width of 1 mm and the inner electrode had a diameter of 3.5 mm, leaving the space between them of 0.5 mm. Current-voltage characteristics for the guarding and the internal electrode of the CdTe-II sample with (**BEBM**) treatment before and after surface passivation (**BEBM+NHF**) are shown in Fig. 4.1. After the surface passivation in NH_4F/H_2O_2 the reduction of the surface leakage current was about 99.7 %, while the values of the bulk current passing through the detector remained similar to those before passivation treatment. It was found that the shapes of the current voltage characteristics using a guard ring or one electrode are very similar. Therefore other measurements of current voltage characteristics were performed with planar electrodes on both contact sides without the guard ring structure.

After the surface treatments with various chemical etchants and passivators on CdTe/CZT detectors, the current-voltage characteristics and gamma spectrum of ^{241}Am gamma source were measured. The obtained results were similar for all four samples despite on the surface treatments order. Fig. 4.2 shows absolute values of current-voltage characteristic for six different surface treatments on CZT-I sample. Small asymmetry of the current-voltage curves is most probably done by different wall side leakage current at opposite polarities or different quality of the native surface oxide formed during contact preparation [44]. Hence it is possible that on the one side the contact was slightly more injecting. Corresponding normalized spectrums of ^{241}Am

gamma source obtained at the bias of -800 V are shown in Fig. 4.3. The spectral resolution of the gamma peak at 59.6 keV, CCE and the current at -800 V are presented in Table 4.2 for these different surface treatments. Calculated percentage reduction of the leakage current compared with the (**BM**) method is shown in Table 4.2. Evidently (**BE**) surface treatment does not lead to lower leakage current values and higher gamma peak resolution than initial (**BM**) treatment. On the other hand the surface passivation by NH_4F/H_2O_2 after chemo-mechanical polishing (**BE+NHF**) resulted in the lowest value of the leakage current from all treatments. The leakage current reduction was approximately 96%.

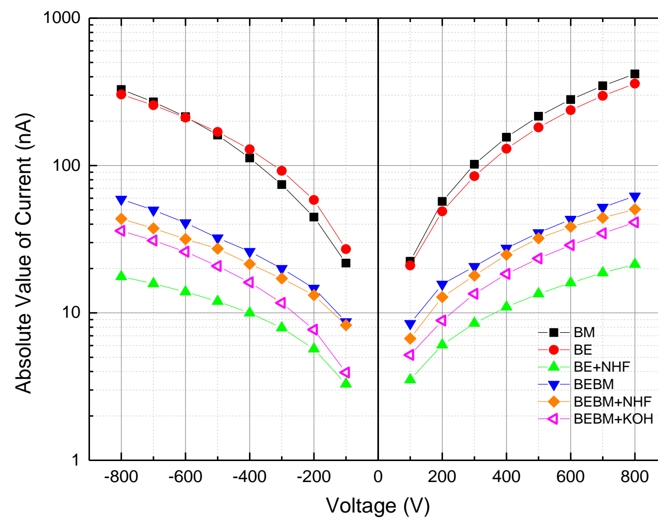

***Fig. 4.2** Current-voltage characteristic for various surface treatments on CZT-I sample.*

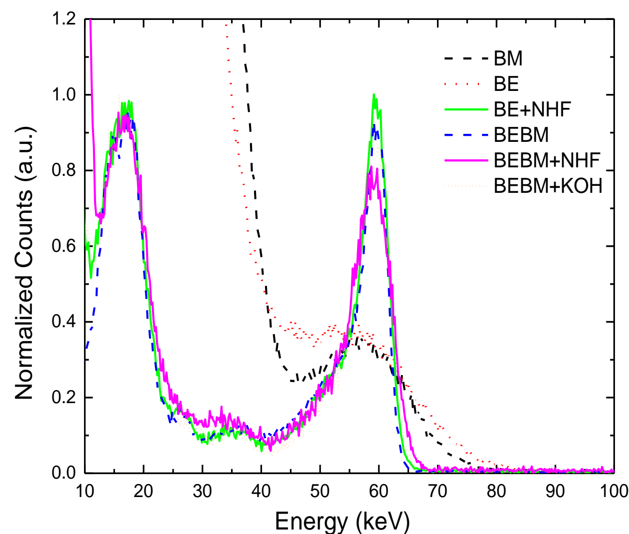

***Fig. 4.3** Normalized spectrum of gamma ^{241}Am obtained with CZT I detector for different surface treatments at -800 V bias*

Surface treatment	R_γ [%]	CCE_γ [%]	I [nA]	% Reduction of leakage current compared to (**BM**)
BM	31.4	91.1	-327.9	-
BE	49.4	87.5	-303.2	8
BEBM	12.1	96.3	-59.0	82
BEBM+NHF	9.9	96.5	-43.5	87
BE+NHF	9.4	96.5	-17.6	95
BEBM+KOH	8.8	96.1	-36.0	89

Table 4.2 *Resolution ($R\gamma$), $CCE\gamma$ and current (I) for various surface treatments on the CZT-I sample at bias of -800 V*

Even though (**BEBM**) surface treatment shows lower leakage current values and better energy resolution than individual methods (**BE**) or (**BM**), additional surface passivation (**BEBM+NHF/KOH**) led to higher leakage current reduction with the same spectrum quality. By reducing the leakage current and reducing the negative properties of surface states, respectively, the passivation in NH_4F/H_2O_2 or KOH led to better detector parameter values than (**BEBM**) treatment itself (see Table 4.2).

4.3. Surface effect on the internal electric field

Using the 5.5 MeV ^{241}Am alpha particle source, the internal electric field profile was determined by TCT apparatus described in the chapter 3.3.3. "Alpha-induced transient-current-technique setup".

The linear internal electric field profile in the sample CZT-I obtained by TCT method after the different surface treatments is presented in Fig. 4.4. Treatments (**BM**), (**BEBM**), (**BE+NHF**), (**BEBM+NHF**) and (**BEBM+KOH**) have similar profiles of the internal electric field. The value of electric field at the cathode side is changing due to the thinning of the sample between each measurements. The significant slope difference of the internal electric field was measured only for (**BE**) treatment. It shows that this surface treatment influences the profile of the internal electric field. This again can be caused by different oxide structure formation on the detector body prior to the gold contacts fabrication on the sample. The formation of this oxide layers was often presented in the literature [26], [44], [65], [66]. The amount and the type of this oxide (TeO_2, CdO, ZnO…) are dependent on the used surface treatment as our group

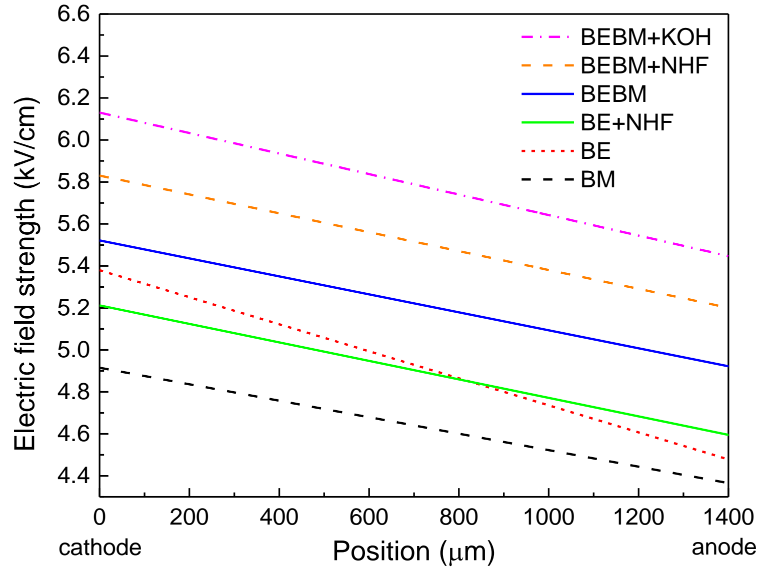

Fig. 4.4 Calculated linear profile of the internal electric field in CZT-I detector for various surface treatments at -800 V bias.

has reported in [45], [76] on different CdTe/CZT samples, where XPS was used for chemical analysis of the surfaces. The conclusion of XPS experiment is that the (**NHF**) passivation creates surface layer primarily of TeO_2. Going deeper to the sample, there is an increasing appearance of CdO with a corresponding decreasing appearance of TeO_2. It can be assumed that similar oxides are created after (**BEBM**) treatment. Because the surface is etched mostly by bromine-methanol solution as in (**BM**) method, therefore it should react with (**NHF**) in a similar way.

4.4. Surface effect on time stability

The surface passivation after chemo-mechanical polishing (**BE+NHF**) gave the best detector parameters – the highest achieved spectral resolution, the lowest leakage current values and similar internal electric field profile as other treatments. However, the detector properties are not long term stable. Fig. 4.5 and 4.6a show surface degradation within seven days after surface passivation in NH4F/H2O2. Increasing noise was measured seven days after this surface treatment and after 21 days the noise was so high that it was not possible to obtain any spectrum at all.

Considering the low time stability of (**BE+NHF**) surface treatment, chemo-mechanical polishing with additional chemical etching treatment and further passivation (**BEBM+NHF**) or (**BEBM+KOH**) appears to be an optimal surface treatment (see Fig. 4.5). Reduction of the leakage current is approximately 90 % which is only about 4 – 5 % lower than in the case of (**BE+NHF**) treatment as stated in Table 4.2. Nevertheless, it is obvious that such prepared detectors show long-term stabile performance which is seen in Fig. 4.5 and 4.6b and 4.6c. Even after 21 days there is no significant difference in the obtained spectrum and the value of the leakage current is stable in time.

The (**BEBM+NHF**) treatment performed on CZT-II sample was studied for one year. Fig. 4.7 and Fig. 4.8 shows current-voltage characteristics and obtained gamma spectrum before and one year after performing this treatment on CZT-II

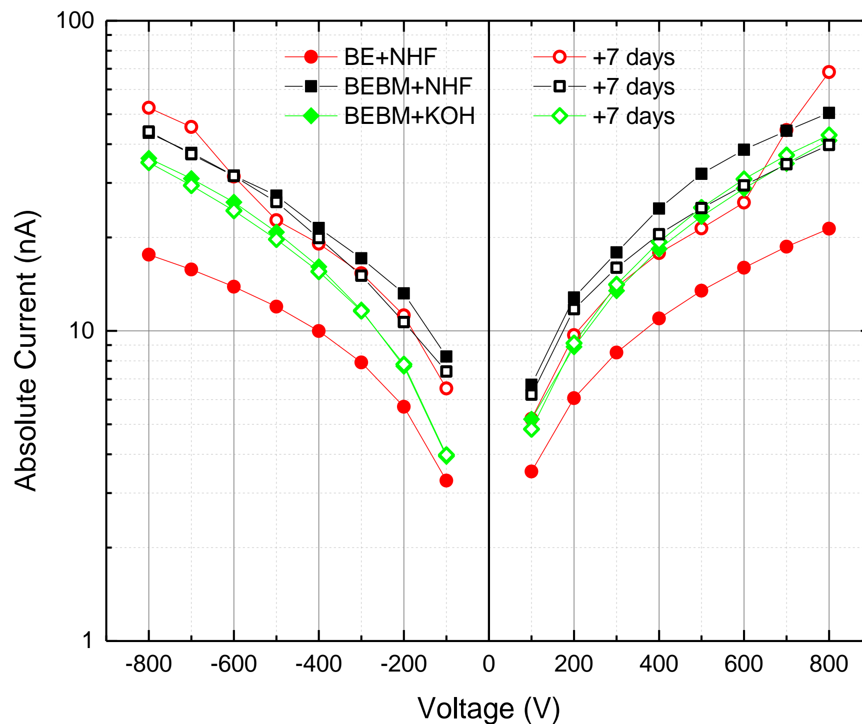

Fig. 4.5 *Current-voltage time dependency for various surface treatments on CZT-I sample.*

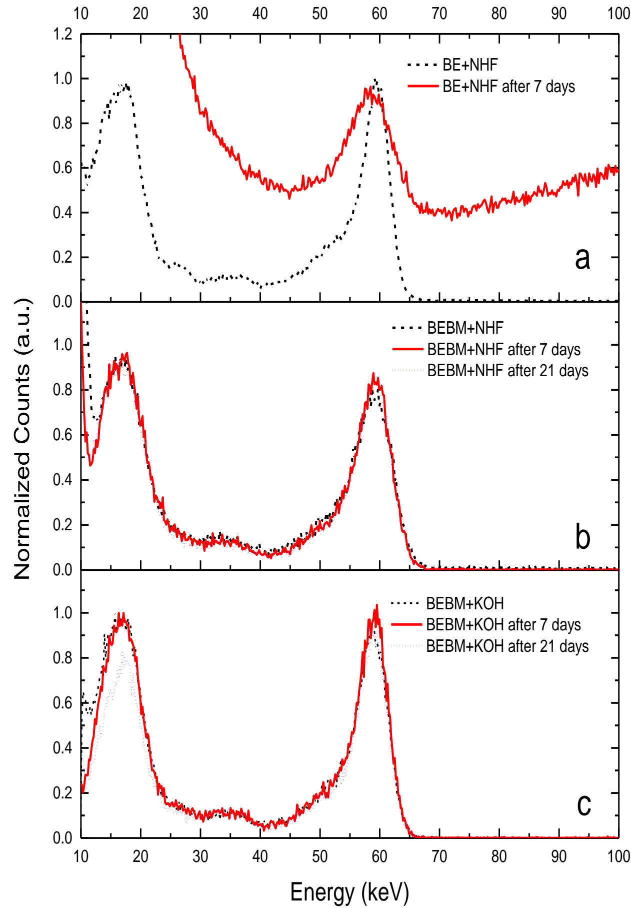

Fig. 4.6 *Time dependency of gamma ^{241}Am spectrum obtained with CZT-I detector at -800 V bias for (**BE+NHF**) treatment (a), (**BEBM+NHF**) treatment (b) and (**BEBM+KOH**) treatment (c).*

sample, respectively. In Fig. 4.7 there is visible relaxation to lower values of current as well as on sample CZT-I within 7 days (see Fig. 4.5). And also there is no deterioration in obtained spectrum as shown in Fig. 4.8. The spectral resolution of such prepared detector is long term stable.

The results shown in Fig. 4.7 are in good correlation with results of surface oxide layers dynamics and properties study on Sample C. The surface was created by passivation with (**NHF**) solutions. The study was made by optical ellipsometry (chap. 3.4) and the leakage currents were measured simultaneously with the ellipsometry for up to 40 days. After the surface passivation the oxide thickness was

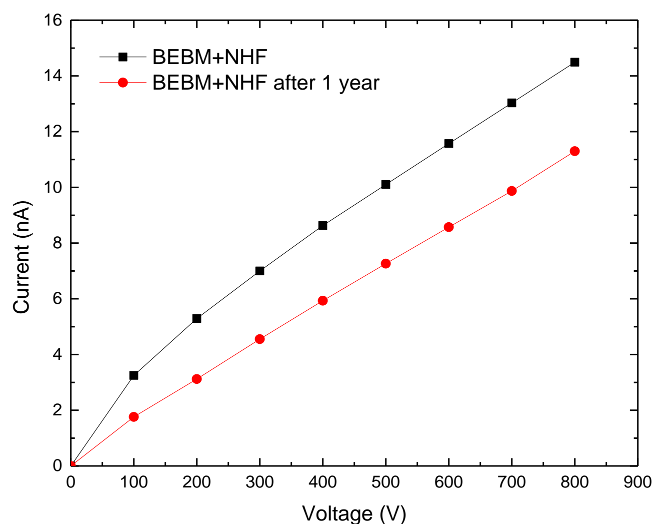

Fig. 4.7 *Current-voltage time dependency for **BEBM+NHF** treatment on CZT-II sample.*

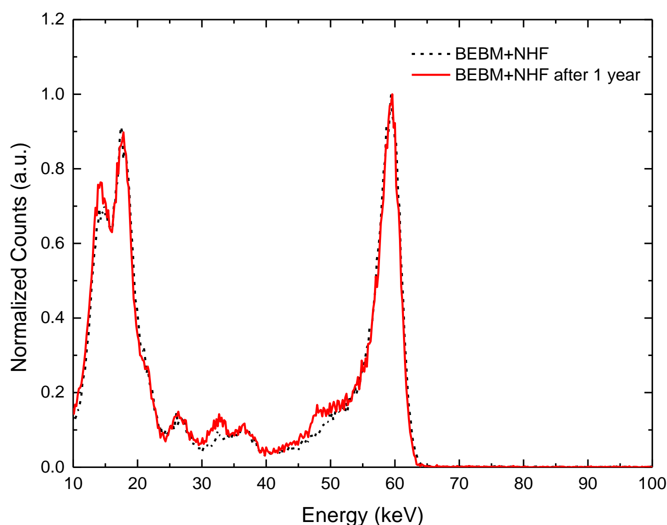

Fig. 4.8 *Time dependency of gamma ^{241}Am spectrum obtained with CZT-II detector for BEBM+NHF treatment at -800 V bias.*

large, indicating a high oxidization ability of the (**NHF**) solution. This can be seen in Fig. 4.9 which shows a time evolution of the effective surface layer thickness determined by ellipsometry. In this figure it can be also seen that during the following several days there was a visible increase of the layer thickness followed by a slightly saturated growth with dependence on time. The leakage current shown in Fig. 4.10 was very low after the passivation, and decreased even more during the following 40 days. This passivation resulted in the growth of a thicker oxide surface layer that had low leakage currents and was stable during the observed period.

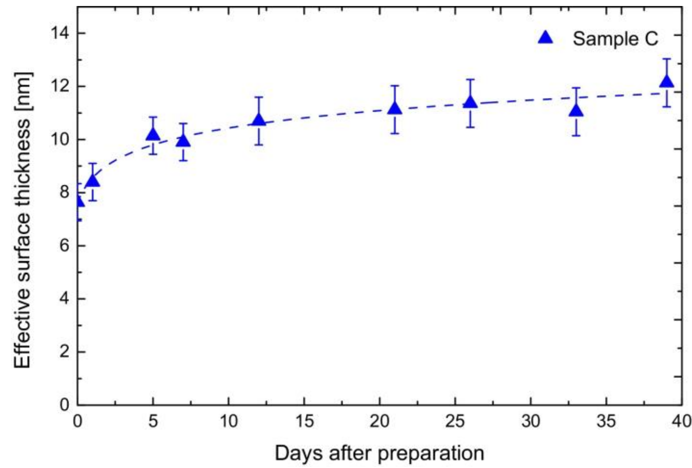

Fig. 4.9 *Time evolution of the effective surface layer thickness of Sample C over 40 days. Dashed line is depicted to highlight the oxide growth trend. Sample C was passivated for 2 min in* NH_4F/H_2O_2 *solution.*

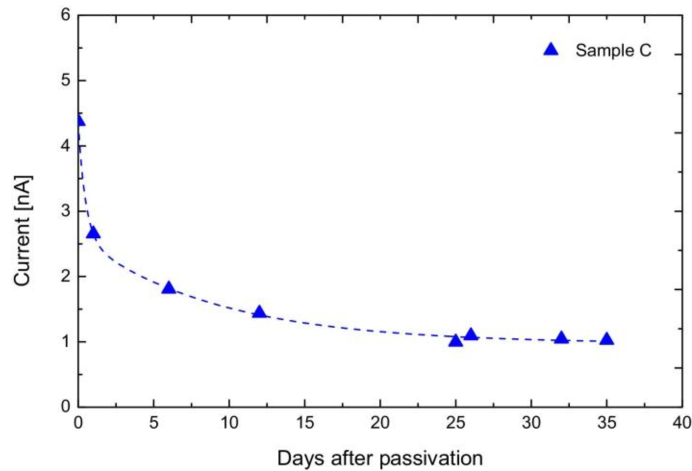

Fig. 4.10 *Time evolution of the current of Sample C at 400 V bias within 40 days. Dashed line is depicted to highlight current evolution connected to the oxide growth trend. Sample C was passivated for 2 min in* NH_4F/H_2O_2 *solution.*

Thus it confirms that passivation produces higher leakage current reduction comparing to simple (**BEBM**) method while maintaining similar spectra resolution and CCE and furthermore enhances the time stability. It is also unnecessary to create the Guard Ring structure on the anode side of such prepared detector as it is recommended in [26] which makes the detector preparation much easier.

4.5. Chapter summary

The effects of different surface etching and passivation methods executed on two CZT and two CdTe detectors were characterized by current-voltage characteristics, spectrum pulse high analysis and the internal electric field profile. First, the comparison of various surface treatments was done in order to lower the value of the surface leakage current. After that, the time stability of such prepared detectors was studied.

One of the findings was that the internal electric field was only affected by the chemo mechanical polishing treatment (**BE**). Moreover this treatment is giving the worst spectral resolution of all used methods. Other methods maintained the similar profile of the internal electric field.

Detector samples with surface passivation by NH_4F/H_2O_2 give the best leakage current values (resulting in a better spectrum with higher resolution) compared to chemically etched detectors. However, the results of this work indicates that the passivation after chemo-mechanical polishing (**BE+NHF**) is not stable in time. Within seven days after the surface passivation increased values of leakage current and increased noise were observed.

Comparing to this, chemo-mechanical polishing with additional chemical etching and consequent passivation in 50% potassium hydroxide (**BEBM+KOH**) or in NH_4F/H_2O_2 aqueous solution (**BEBM+NHF**) gives only about 5 % lower leakage current reduction. But the highest advantage of these treatments is long-term stability (measured within seven, 21 days and one year, respectively) and are overall optimal in spectral resolution aspect compared to the other used surface treatments.

5. Infrared depolarization of detectors under high flux of X-ray radiation

High-resistivity CdZnTe is a material of choice for high energy X-ray and gamma ray detectors working at room temperature due to the high average atomic number and wide bandgap. Nowadays, CZT is used in several high radiation flux applications, such as computed tomography, gamma cameras, mammography and astrophysics [4]. The main factor usually limiting the CCE of CZT detectors under high radiation fluxes is the polarization phenomenon. This chapter deals with high flux polarization and its possible compensation.

In this case, the polarization results in a deformation of the internal electric field caused by an accumulation of positive space charge at deep levels due to the trapping of photogenerated holes [77], [78]. The internal electric field in the detector strongly increases towards the cathode and decreases towards the anode. An inactive region with a very low electric field is formed, which results in a reduction of CCE.

The motivation of the infrared (IR) depolarization of the detector is based on several studies of the high flux optical manipulation of deep level occupations in the bandgap, which were performed on CdTe [79], [80] and CZT [81], [82] previously. It has been previously introduced the concept of the electric field restoration of polarized indium doped CZT detectors based on the optical transition of electrons from the valence band to the deep level in which the holes are trapped. This transition induced by the IR light with the wavelength around 1200 nm (~1.03 eV) [83] reduces the originally positive space charge accumulation.

The first part of this chapter describes an application of IR light-induced depolarization on a polarized CZT detector working under high radiation fluxes. The second part presents the utilization of simultaneous IR illumination on the spectroscopic properties of a CZT detector operating under high radiation flux. The internal electric field study by Pockels effect measurements and the pulse height spectrum analysis using a standard spectroscopic setup were used for the characterization of the IR depolarization phenomena. In some measurements, the LED at 940 nm (~1.32 eV) instead of X-rays was used, because it was previously shown [84] that the IR light with a slightly below the bandgap wavelength (around 900-950 nm in the case of CZT) produces electrons and holes in the CZT detectors and may cause their radiation-induced polarization at high fluxes similar to X-rays. Similar flux

influences on electric field profiles and detector currents were observed for X-ray and 910 nm LED types of excitations in [85]. In the context of this chapter, ‘high flux’ means a sufficient intensity of the radiation under which the distribution of the internal electric field in the detector changes, while under ‘low flux’, it does not. High flux is represented by X-rays or high intensity light and low flux by a low activity ^{241}Am gamma source (89 kBq) or low intensity light.

5.1. Sample preparation and experimental section

For this study, it was used two neighbouring detector-grade samples cut from the <111>-oriented single-crystal wafer of In-doped $Cd_{0.9}Zn_{0.1}Te$. The electron mobility-lifetime product was set by alpha spectrum pulse height analysis as $\mu_e \tau_e = 3 \cdot 10^{-3}$ cm$^2 \cdot$V^{-1}. The resistivity was determined by COREMA setup of ~ 10^{10} Ω·cm.

Sample 1 with dimensions of 5 × 4.3 × 1.5 mm^3 was used for the Pockels effect measurements to demonstrate the radiation-induced polarization and to find an optimum wavelength for the depolarization of the given material. The surface of the sample was optically polished in order to be suitable for monitoring the transmittance distribution of the testing light during the Pockels effect measurements. The used surface treatment introduces high leakage current. Therefore, the sample was equipped with planar gold cathode and indium anode on large opposite surfaces by evaporation,. In this configuration, the indium anode helps to reduce the leakage current.

For a study of the polarization and depolarization processes in detectors, the method of infrared spectral scanning (IRSS) exploiting the Pockels effect was developed in our laboratory and was tested on several CZT and CdTe samples [84]–[86]. The IRSS is based on measurements of the electric field profiles in the biased sample, which is excited by the light with a fixed wavelength causing the polarization (represented by an LED at 940 nm in this paper). Then, it is simultaneously illuminated by a tunable IR light with wavelengths ranging between 0.9 and 1.7 μm (~1.38 – 0.73 eV). The experimental setup for IRSS is shown in Fig. 5.1. Tunable light is coming from a Carl Zeiss SPM2 monochromator equipped with a 50 W halogen lamp and a LiF prism. This tunable light from the monochromator with a constant photon flux is convenient for studying the change of the occupations of deep levels

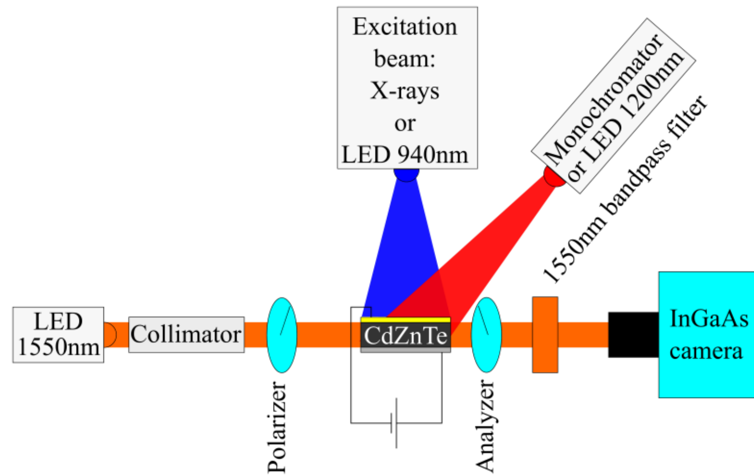

Fig. 5.1 *Experimental setup for depolarization Pockels effect measurements performed on Sample 1. During standard electric field measurements, the cathode of the sample was irradiated by X-rays and simultaneously illuminated from the side by a 1200 nm LED during depolarization mode. During the infrared spectral scanning (IRSS) measurements, the cathode was illuminated by a 940 nm LED and by tunable light from the monochromator from the side.*

caused by the optical manipulation. By this method, it is possible to find an optimal depolarizing wavelength.

Sample 2 with dimensions of $5 \times 4 \times 0.9$ mm^3 was used for X-ray and gamma-ray spectroscopic measurements. Because there is no need for optically polished surfaces to be used for spectroscopic measurements, its surface was chemically etched in a 1% Br-methanol solution for 1 min in order to reduce the leakage current. When the leakage current was reduced by chemical etching, there was no need to use indium anode. Therefore after the etching, the sample was equipped with evaporated gold contacts covering both larger sides because gold creates quasi-ohmic contact on CZT [75]. The contact, which was acting as the anode, was divided into a round pixel with a diameter of 0.5 mm and the surrounding guard ring separated by an approximately 0.5 mm wide gap, as is schematically shown in Fig. 5.2.

The reason for using the pixel was to decrease the effective volume of the detector in order to reduce the number of events during the detection of the high flux of X-rays. During spectroscopic measurements, the detector Sample 2 was placed inside a 3 mm thick aluminium shielding box as it is seen in Fig. 5.2. In all spectroscopic measurements the sample was irradiated on the cathode side. The

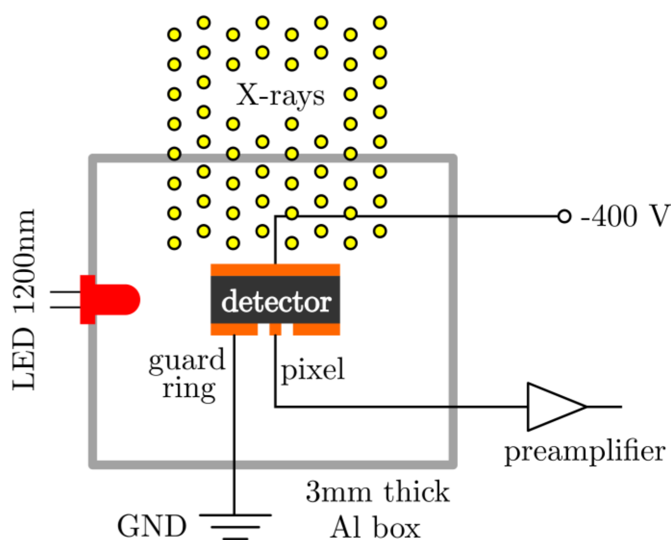

Fig. 5.2 *The experimental setup used for X-rays measurements on Sample 2 (b). The planar cathode (top) was irradiated by X-rays. The pixel with a 0.5-mm diameter was surrounded by a guard ring covering the rest of the anode side (bottom).*

cathode was biased by high voltage supply ISEG SHQ 122M. Both the pixel and the guard ring were set to the zero potential, while the detector signal from the pixel was amplified with a preamplifier based on the Amptek A250 amplifier with a 560 μs decay time. The multichannel analyser Canberra DSA1000 with the lowest rise time of 0.4 μs and zero flat top was used for spectral analysis. For ultra-high count rates, a lower rise time/flat top is useful, as the pile-up probability and the necessary processing ability decrease with decreasing rise time/flat top. The 1200 nm LED was used to illuminate the side of the detector from the distance of 1.5 cm. The IR depolarization using the LED of the specific wavelength of 1200 nm was motivated by the results of the influence of deep levels on the polarization and depolarization related processes in detectors (see chapter 5.2). As the below bandgap light absorption of CZT is very low, it is expected an almost homogeneous distribution of illumination by the light inside the whole detector sample. The forward current of the LED at 1200 nm was set to 50 mA, and its photon flux measured utilizing the Ophir Vega laser power meter with a Ge detector was 2×10^{14} $mm^{-2} \cdot s^{-1}$ during all of the measurements.

For the X-ray measurements (either Pockels or spectroscopic measurements) samples were placed 1840 mm from a tungsten target X-ray tube MXR160 made by

GE Company. X-ray tube had the standard radiation quality of RQR6 (80 kVp, 1 mm thick inherent beryllium filtration and 3 mm thick aluminium filter).

All of the measurements were performed at room temperature and in steady state conditions. The estimated error of the electric field measurements is 5%, and the error of the X-ray flux is 10%.

5.2. Polarization and IR depolarization

The Pockels effect measurement was used in order to study the spectral dependence of radiation-induced polarization and IR depolarization on the given CZT material. Sample 1 was biased at 500 V, while the gold was acting as the cathode, and its electric field profiles between electrodes were determined for various conditions (Fig. 5.3).

In the dark condition (solid line in Fig. 5.3), the electric field is almost constant. The dark condition means using only the Pockels light with wavelength of 1550 nm without any additional irradiation. The constant internal electric field, according to the Gauss law, represents no or very low space charge accumulation. On the contrary,

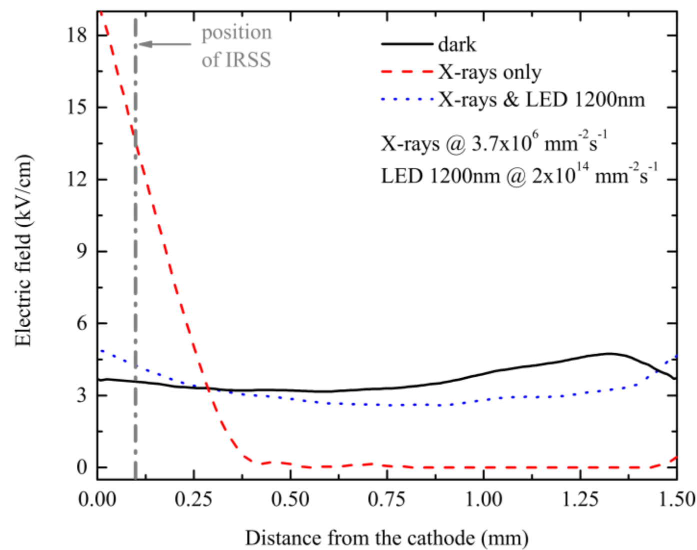

Fig. 5.3 *Electric field profiles between electrodes of planar detector Sample 1 biased at 500 V measured by the cross-polarizer technique based on the Pockels effect. The vertical dash-dotted line shows the depth below the cathode used for IRSS analysis.*

when the cathode side of the detector was irradiated by a high X-rays flux of 3.7×10^6 mm$^{-2}\cdot$s^{-1}, the electric field was accumulated near the cathode and strongly decreased towards the anode. At the distance around 0.4 mm from the cathode towards the anode, it is visible the formation of the so-called dead layer with a very low electric field (dashed line in Fig. 5.3). Such a situation is known as the radiation-induced polarization of the detector. It is caused by screening of the electric field by the positive space charge originating from photogenerated holes trapped at a deep level. This inactive layer is created in 75% of the detector volume.

In order to find an optimal wavelength for the IR depolarization, the IRSS measurements were performed at 500 V, and the evaluated electric field at the depth of 0.12 mm under the cathode is shown in Fig. 5.4. In the dark condition, the electric field is ~ 3.3 kV/cm, as can be expected from the applied bias (solid line in Fig. 5.4). After that, the sample was set to the polarized state by the cathode side illumination with the LED at wavelength of 940 nm. This polarization caused that the electric field below the cathode increases to ~ 13.3 kV/cm (dashed line in Fig. 5.4). Then the detector side was simultaneously illuminated with low energy light from the monochromator. The flux of the light from the monochromator was fixed at 5×10^{13} mm$^{-2}\cdot$s^{-1} for all of the wavelengths – circles in Fig. 5.4. The energy of the monochromator light was ranging between 0.73 eV (1700 nm) and 1.37 eV (900 nm). For the energy between 0.73 eV (1700 nm) and 0.8 eV (1550 nm) there is no significant change of the electric field. Between 0.8 eV (1550 nm) and approximately 1.1 eV (1130 nm), there is a significant lowering of the electric field below the cathode when the electric field dropped to ~ 9 kV/cm. This corresponds to decrease of the accumulated positive space charge.

This IR light-induced depolarization effect can be explained as the neutralization of the positive space charge associated with trapped holes by an optical transition of electrons. Electrons are excited from the valence band to the energetic level where the holes are trapped and recombination may occur. This depolarization gets stronger with increasing intensity of the depolarizing light [83].

With a further increase of the photon energy of the light from the monochromator above 1.1 eV (wavelength below 1130 nm), the positive space charge accumulation prevails due to the trapping of a high amount of photogenerated holes. This trapping originates from higher absorption when the photon energy approaches the main photoconductivity peak localized slightly below the bandgap energy [87].

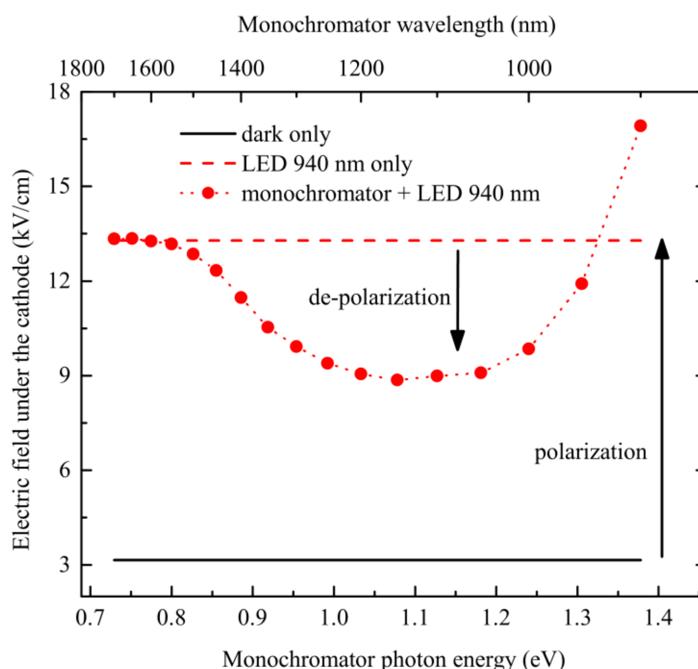

Fig. 5.4 *Infrared spectral scanning (IRSS) of the electric field under the cathode of planar detector Sample 1 biased at 500 V measured by the cross-polarizer technique based on the Pockels effect.*

The positive space charge accumulation could be also explained by the optical transition of electrons from the level with the energy of 1.1 eV to the conduction band [85]. Both mechanisms lead to the same effect of positive space charge accumulation in the case of the below bandgap light illumination.

Based on the strongest depolarization effect around 1.05 eV (1180 nm) shown in Fig. 5.4, it has been chosen a commercially available LED with a central wavelength at 1200 nm (~ 1.03 eV) for the further IR depolarization investigation. Moreover, the 1200 nm LED has higher optical power than 1200 nm light from a monochromator. IR depolarization of the detector under a high flux of X-rays is demonstrated in Fig. 5.3 by blue dotted line. In this case the electric field profile of Sample 1 under X-rays flux and simultaneous illumination with the 1200 nm LED is again almost flat, like in the dark condition. This is a sign of no significant space charge accumulation. The stronger effect of IR depolarization by the 1200 nm LED shown in Fig. 5.3 than by the monochromator shown in Fig. 5.4 is caused by the four times higher photon flux of the used LED.

5.3. IR depolarization in X-rays spectroscopy

In this subchapter, the results of X-rays' spectroscopic measurements performed on the CZT Sample 2 biased at 400 V under X-ray radiation are presented. The cathode of the sample was irradiated by high fluxes of X-rays, and simultaneously, the side of the sample was illuminated with an LED at 1200 nm wavelength. The experimental setup is shown in Fig. 5.2.

Fig. 5.5 shows the spectral response of Sample 2 under X-rays coming from an X-ray tube set to 80 kVp. The various X-ray fluxes were created by different setting of the X-ray tube power. Under a low radiation flux, while the flux of the X-ray tube is set between 5.72×10^5 $mm^{-2} \cdot s^{-1}$ and 1.71×10^6 $mm^{-2} \cdot s^{-1}$, there is no polarization of the detector. The maximum of the spectral curve is located at around 40 keV and decreases to the lower energies because of the shielding by a 3 mm thick aluminium box and a 3 mm thick aluminium filter of RQR6. Although the photon energy should be limited to 80 keV, there is a tail at higher energies caused by pile-up events. A pile-up event occurs when the detection system's readout electronics records two or more incident X-ray photons that are proximate in time as only one photon with higher energy. Nevertheless, the amount of pile-up events is negligible, maximally up to 8% for energy higher than 80 keV during all of the measurements. Therefore, this issue is not discuss anymore, and the rest of the discussion is only about polarization and depolarization effects.

Fig. 5.6 shows the spectral response of Sample 2 under X-ray radiation and simultaneous illumination of the detector by the 1200 nm LED. It can be seen that the spectra are also slightly affected by the high energy tail of pile-up events, but they still keep their typical shape up to 3.72×10^6 $mm^{-2} \cdot s^{-1}$ of X-ray flux. Although there is a visible polarization at the flux of 4.72×10^6 $mm^{-2} \cdot s^{-1}$ demonstrated by the lower charge collection, the position of spectral maxima can more or less maintain their position compared to the case without the LED illumination. The influence of the 1200 nm LED on the energy resolution of the detector is discussed later.

Comparing the measured X-ray spectra from Fig. 5.5 and Fig. 5.6, it is obvious that simultaneous depolarizing illumination keeps the spectral information up to higher X-ray fluxes.

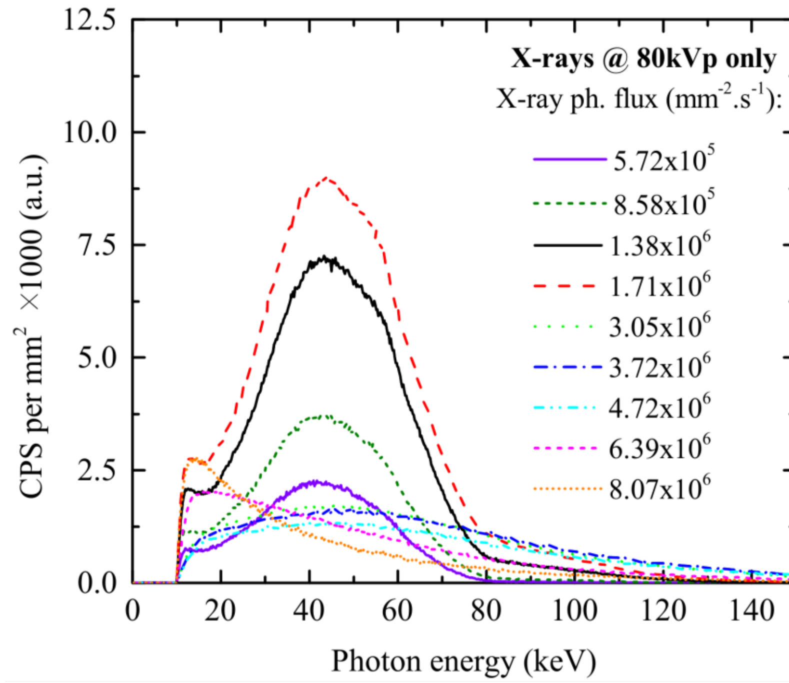

Fig. 5.5 *Spectra measured on the central pixel of Sample 2 under various X-ray radiation fluxes only. The X-ray tube was biased at 80 kVp. The applied bias on the sample was 400 V.*

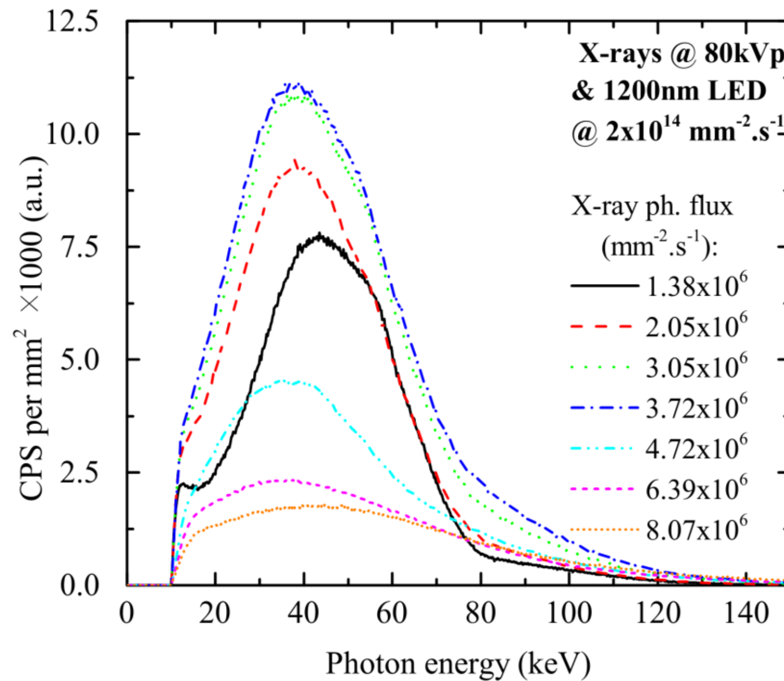

Fig. 5.6 *Spectra measured on the central pixel of Sample 2 under various X-ray radiation fluxes with simultaneous illumination by the 1200 nm LED with photon flux of* 2×10^{14} $mm^{-2} \cdot s^{-1}$. *The X-ray tube was biased at 80 kVp. The applied bias on the sample was 400 V.*

Fig. 5.7 shows the total number of counts per second (CPS) per millimetre square dependence on the X-ray flux recorded by the Sample 2. In the case of sample irradiation only by X-rays, CPS increases linearly up to the flux of 1.71×10^6 $mm^{-2}\cdot s^{-1}$. This is represented by squares in Fig. 5.7. This reflects the fact that the sample is not yet polarized [77]. For fluxes equal to and higher than 3.05×10^6 $mm^{-2}\cdot s^{-1}$, total CPS decreases due to worse CCE caused by polarization. Spectra for X-ray flux equal to and higher than 3.05×10^6 $mm^{-2}\cdot s^{-1}$ lose their typical shape due to the polarization of the detector, which is clearly seen in Fig. 5.5. For the maximum used X-ray fluxes (ping and orange curves in Fig. 5.5) the spectrum shape is completely transformed due to full polarization of the sample.

In case of X-rays and simultaneous illumination by 1200 nm LED, the number of CPS increases for the X-ray flux up to 3.72×10^6 $mm^{-2}\cdot s^{-1}$ (circles in Fig. 5.7). This also supports the conclusion that simultaneous depolarizing illumination keeps the spectral information up to higher X-ray fluxes. Unfortunately, or X-ray fluxes higher than 3.72×10^6 $mm^{-2}\cdot s^{-1}$, CPS decreases because of insufficiently high LED intensity; therefore, the polarization prevails again.

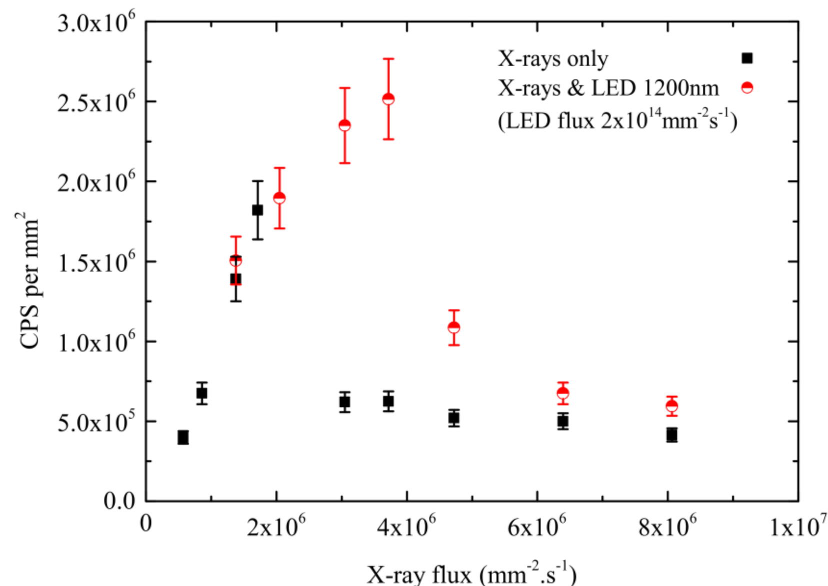

Fig. 5.7 *Dependence of counts per second per mm^2 on X-ray flux only and X-ray flux with simultaneous illumination by 1200 nm LED for Sample 2.*

5.4. Influence of IR depolarization on energy resolution

The influence of IR depolarization on the energy resolution of Sample 2 was tested by using γ-^{241}Am radiation source.

This gamma source with a low activity of 89 kBq was put inside the shielding aluminium box at a distance of 1 cm from the cathode side of the detector.

Polarization and depolarization modes were activated using the LEDs at 940 nm and 1200 nm, respectively. As it was previously shown in [85], after the adjusting the intensity of IR LED, the polarization of the detector was achieved comparable to the application of the X-ray flux. The similar effect on the internal electric field determined by Pockels effect measurement in [85] and on the values of electric current were observed in both cases. Therefore it can be assumed that both types of irradiation lead to a similar change of deep levels occupation.

The 940 nm LED has better defined radiation and is easier to operate then the spectrally broad X-ray source. But the main advantage of illumination by 940 nm LED was the possibility to compare spectral resolution under various conditions compared to the measurements under X-rays. In the case of X-rays, the detector spectral resolution was not sufficient enough to observe characteristic X-rays of tungsten K lines. Also the bremsstrahlung had a broad spectrum, which is not sufficient at all for deciding about the detector energy resolution.

Fig. 5.8 shows the gamma spectra of γ-^{241}Am under simultaneous illumination by the polarizing LED at 940 nm simulating a high flux of X-rays. The spectra were normalized to the maximal number of counts for the photon energy equal to or higher than 35 keV. This normalization was chosen in order to compare spectra around the 59.6 keV photopeak of ^{241}Am. In the dark condition (gamma source without polarizing LED), the energy resolution of the used detector Sample 2 at 59.6 keV was 5.7 keV (~ 9.6%), and the L line of ^{237}Np (the product of the alpha decay of ^{241}Am) is also apparent at around 17 keV. With increasing of the photon flux of the 940 nm LED, the energy resolution worsened significantly, and the counts at lower energies related to higher electronic noise of the spectroscopic apparatus increased. The higher the photon flux of the 940 nm LED is, the higher is the amount of photogenerated electrons, resulting in a larger current flowing through the whole spectroscopic apparatus. This current contributes to the noise of the used electronics (e.g., amplifier) [60], which is reflected in the low energy part of the spectrum. For the 940 nm LED flux higher than

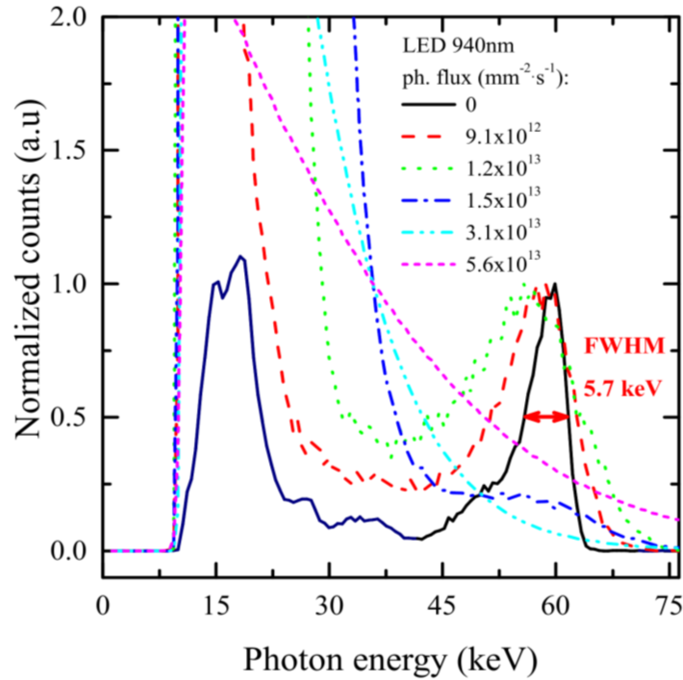

Fig. 5.8 *Pulse height spectra of γ-^{241}Am obtained with Sample 2 under various levels of polarization by the LED at 940 nm at 400 V. The spectra were normalized to the maximal number of counts for the photon energy equal to or higher than 35 keV.*

1.5×10^{13} mm^{-2}·s^{-1}, the photopeak completely disappeared due to the noise of the detector.

Furthermore, in Fig. 5.8 it is visible that the higher detector polarization shifted the central position of the 59.6 keV photopeak to lower energies. This is caused by the losses of the photogenerated electrons due to the polarization.

On the other hand, gamma spectra from Fig. 5.9 measured under simultaneous illumination of the sample by both polarizing (940 nm) and depolarizing (1200 nm) LEDs do not change until a certain flux of 5.6×10^{13} mm^{-2}·s^{-1} of polarizing light. The photon flux of the depolarizing LED at 1200 nm was fixed to 2×10^{14} mm^{-2}·s^{-1}. Although the low channel noise is higher than in the dark condition (Fig. 5.8), the negative influence of the 1200 nm LED illumination on the spectra is lower at higher energies, and the detector energy resolution is 6.75 keV (~ 11.3%) at 59.6 keV. This fact could make IR depolarization useful for spectroscopic CZT detectors operating under high radiation fluxes.

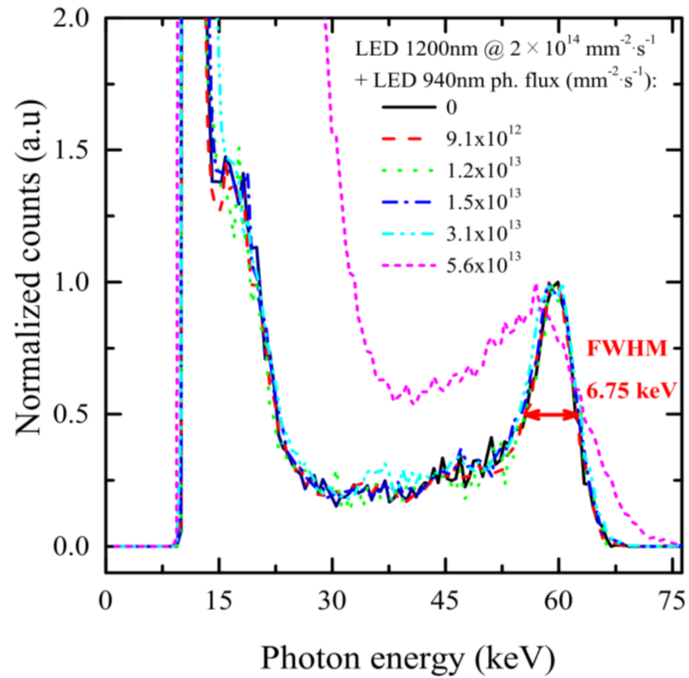

Fig. 5.9 *Pulse height spectra of γ-^{241}Am obtained with Sample 2 under various levels of polarization by the LED at 940 nm with the additional depolarization at a 400 V bias. The spectra were normalized to the maximal number of counts for the photon energy equal to or higher than 35 keV. Depolarization was set by the LED at 1200 nm with photon flux of* 2×10^{14} $mm^{-2}\cdot s^{-1}$.

5.5. Chapter summary

In this chapter, it has been demonstrated a promising mechanism of the IR depolarization of spectroscopic In-doped CZT detectors operating under a high flux of X-rays using the LED at 1200 nm with a relatively high photon flux of 2×10^{14} $mm^{-2}\cdot s^{-1}$. This optimal depolarizing wavelength was found using the IRSS method based on the internal electric field profile determination by the Pockels effect measurements. The IR depolarization is based on the neutralization of a positive space charge in the detector by an optical transition of electrons from the valence band to the deep level. With the intensity of the used 1200-nm LED, the IR depolarization works up to approximately a two times higher X-ray flux than without the LED on the studied detector.

Although there is a quite high low-channel noise under the 1200 nm illumination, the energy resolution of the detector is only slightly affected at photon

energies around 60 keV, which can make the concept of IR depolarization useful. High flux spectroscopic radiation detectors with IR LED depolarization could be successfully applied in nuclear power plants, computed tomography, X-ray defectoscopy, etc.

6. Transient-Current-Technique as a powerful tool for detail detectors characterization

The final chapter is focused on the Transient-Current-Technique as a powerful tool for detector characterization. This chapter shows not only the possible application in characterization, but also the modification of TCT apparatus during my doctoral studies. At the beginning TCT apparatus consisted of alpha particle radiation source as it is described in chapter 3.3.3. Then it has been enhanced by the laser source (laser diode powered by pulse generator). By this modification it was possible to irradiate the samples by both, above bandgap and below bandgap laser lights. After that the apparatus was improved by pulse bias source for the time study of detector polarization. The other expansion was the modification for transient charge study in the CPG detectors and the possibility of mapping the samples via XYZ-stages with the resolution of ~ 10 μm. The last modification was changing the laser diodes for the continuum white laser (NKT Photonics SuperK COMPACT, continuum spectral range from 400 nm to 2100 nm) with laser lines filters of FWHM ~ 10 nm.

6.1. Electronic pulse shape formation in transient charge and transient current detection approach in Cd(Zn)Te detectors

The determination of electric field profile and charge collection efficiency is a key for characterizing the semiconductor radiation detectors. Two basic methods – transient charge technique (TChT) and transient-current-technique (TCT) are routinely used for this purpose [8], [32], [36], [42], [88], [89]. While TChT is based on the integration of the current pulse induced on the detector electrode, TCT allows us a direct visualization of the transient current induced by the detected radiation. In spite of apparently definite correspondence between the charge and current transients via simple derivation

$$i(t) = \frac{\mathrm{d}q(t)}{\mathrm{d}t} \tag{6.1}$$

or integration

$$q(t) = \int_0^t i(t')\mathrm{d}t + q_0 \tag{6.2}$$

in time [88], the passing of the signal through real electronic circuits interferes with the evaluation of the quantities and hampers the direct relation between the TChT and TCT transients. This fact is due to the different electrical circuit parameters and signal processing used in either case, which yields substantially different rising edge of the pulse. Consequently, an erroneous collected charge or transient current is obtained if determined by the counterpart method.

Detected TCT pulse enables us to characterize the time resolved charge collection process in the detector volume [8] and evaluate its internal electric field. TCT gives better possibility of time-resolved measurement of the charge formation process in comparison to TChT integration type detection with the low impedance input circuit of the amplifier matched to the detector output. On the contrary, the TChT provides more precise total collected charge measurement than TCT. In order to preserve the information content about the detector electric field profile and the carriers drift mobility, minimum transient pulse shape distortion is needed which helps to minimize any negative influence on the real capturing of the transition phenomena (specifically the leading edge shape). Obviously, frequency response of the current amplifier circuitry is of key significance in this regard.

In this chapter it is compared the TChT and TCT methods as used to measure the carrier transit time and is correctly calculated the mobility. It is also suggest how to improve the transit time readout in case of TChT method.

Both TChT and TCT methods were used to characterize transport properties of two planar $Cd_{0.9}Zn_{0.1}Te$ detectors with gold contacts (labelled CZT-M1 and M2) with the thickness 1.23 mm (M1) and 1.35 mm (M2), which were prepared at Institute of Physics by vertical gradient freeze method. Both measurement techniques are based on the electronic amplification and processing of the detector output pulse.

The TChT setup is described in chapter 3.2.2. In this experiment, two types of the home-made charge sensitive amplifiers (hereafter labeled A1 and A2) with different frequency response have been used to record the integrated pulse. A1 is based on 2SK152 input FET and Amptek A250 integrating amplifier with a buffering amplifier. A2 is based on the same input FET and home-made integrating and buffering amplifier designed by PEVOT Company. Direct input of the high impedance with FET gate electrode is used with 50 Ω impedance adaptation.

The TCT setup used in this experiment is described in chapter 3.3.3.

For both methods alpha particles are used to generate electron-hole pairs and low noise high voltage power supply (Iseg SHQ122M) is used for the detector biasing from 0 to -800 V.

The TCT electron current pulse (the cathode was irradiated) is characterized by very fast transition edges (a few ns and a width of tens of ns). In this case, when the current waveform is generated by an alpha particle, the plasma effect (chapter 3.3.1) delays the initial signal formation, as apparent from extension of the rising time. The bias dependence of current transients (TCT output pulses) for detector CZT-M2 in the bias interval from 300 V to 700 V with 100 V steps is shown in Fig. 6.1 together with the corresponding calculated integral representing the collected charge. The same integral can be directly obtained from the measured TCT signal by using an integration circuit built into the sampling oscilloscope probe, which preserves its full bandwidth [88]. This integral represents the ideal TChT signal, which is not affected by the electronics and from which the same value of transit time comparing TCT signal can be evaluated. The bias dependence in the bias interval from 200 V to 700 V with 100 V steps of the TChT pulse rising edge and corresponding calculated derivative representing the current passing through the detector is shown in Fig. 6.2 for detector CZT-M2 and the integration amplifier with better frequency response (A1).

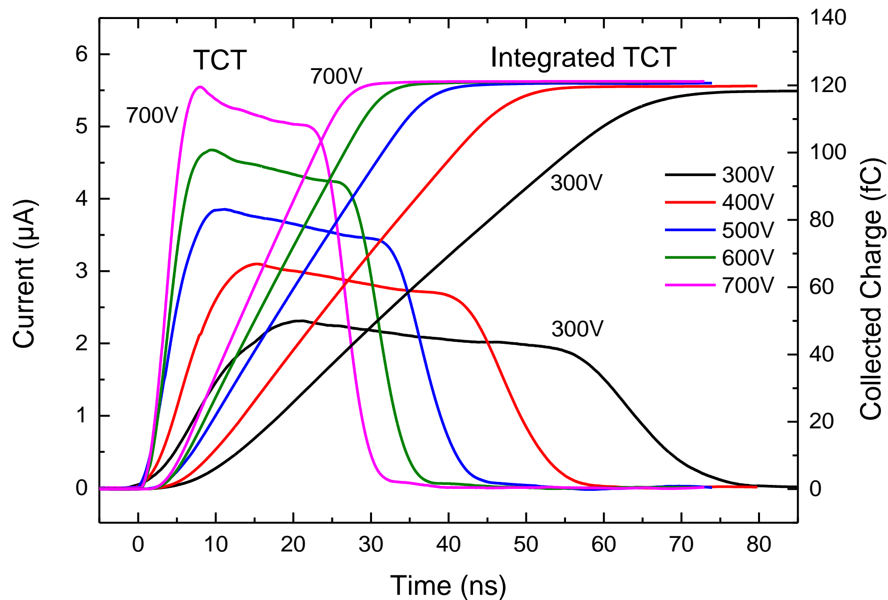

Fig. 6.1 *Transient current pulses and corresponding collected charge obtained by integration via equation (6.2) for CZT-M2 detector.*

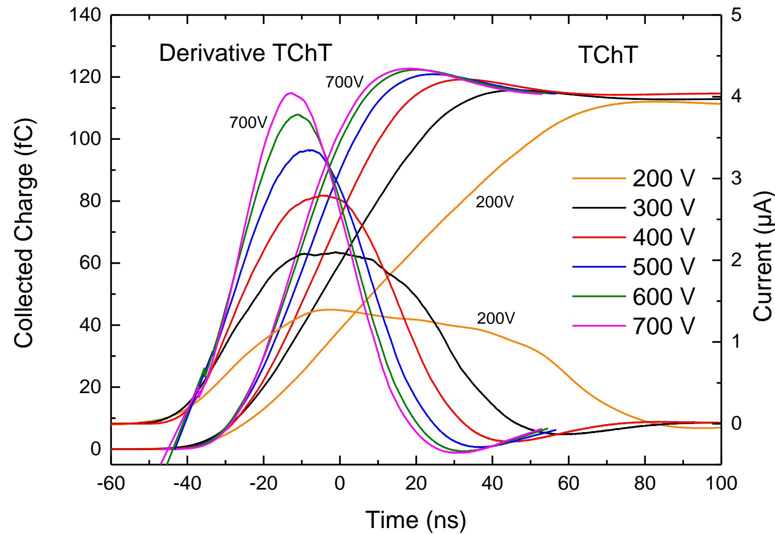

***Fig. 6.2** Transient charge pulses and corresponding current pulse obtained by derivation via equation (6.1) for CZT-M2 detector and A1 amplifier.*

Savitzky–Golay smoothing procedure [90] has been used for the final data treatment of the recorded pulses in both detection methods. Influence of pole compensation resistor trimmer level on the rising time of the charge integration amplifier by using single step function (rise time 2.5 ns) generated with the arbitrary waveform generator (Tektronix AFG3252) is shown in Fig. 6.3. It is evident that a critical aperiodic waveform response with minimum rising edge overshot setup (trimmer level 3) gives the most realistic leading edge.

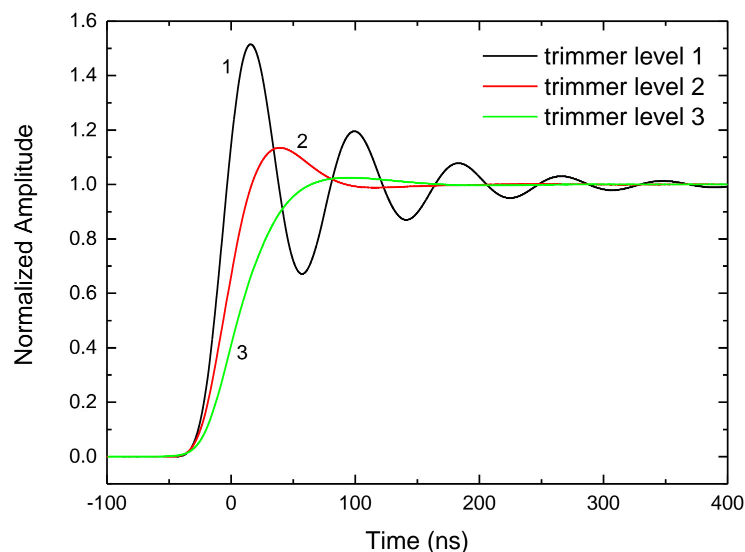

***Fig. 6.3** Charge integration amplifier leading edge for 3 different increasing levels of the pole compensation resistor trimmer setup. Critical aperiodic waveform (level 3, green online) represents an optimum setup.*

In this experimental setup, the electronic design nor one of the amplifiers did allow to fully compensate the pulse overshot. Bias dependence of the derivative waveform should directly correspond to the TCT pulse shape in Fig. 6.1 for each bias voltage; however, it can be observed substantial distortion of the expected derivative shape due to a relatively slow frequency response of both integration amplifiers. Corresponding data for detector CZT-M1 is even more influenced by the amplifier frequency response due to the shorter transit time of detector CZT-M1 (not shown here). On the contrary, integrated waveform from TCT exhibits faster leading edge in comparison to TChT due to a much better high frequency response of its electronic circuitry. This fact serves as clear evidence that no direct experimental correspondence between the two methods can be used for the transient time readout.

In case of relatively low internal charging of the detector, the relation between the carrier mobility μ, the detector width L, voltage U, and the transit time t_r is given by equation (3.6). t_r represents the time taken by the electrons drifting from irradiated cathode towards the anode. In case of TCT the transit time is well determined by taking the intersection of the pulse shape double exponential fit [8]. In case of TChT the transit time is not exactly defined. In this work it is proposed to determine it from the rise time of the charge pulse using the two methods schematically depicted in Fig. 6.4.

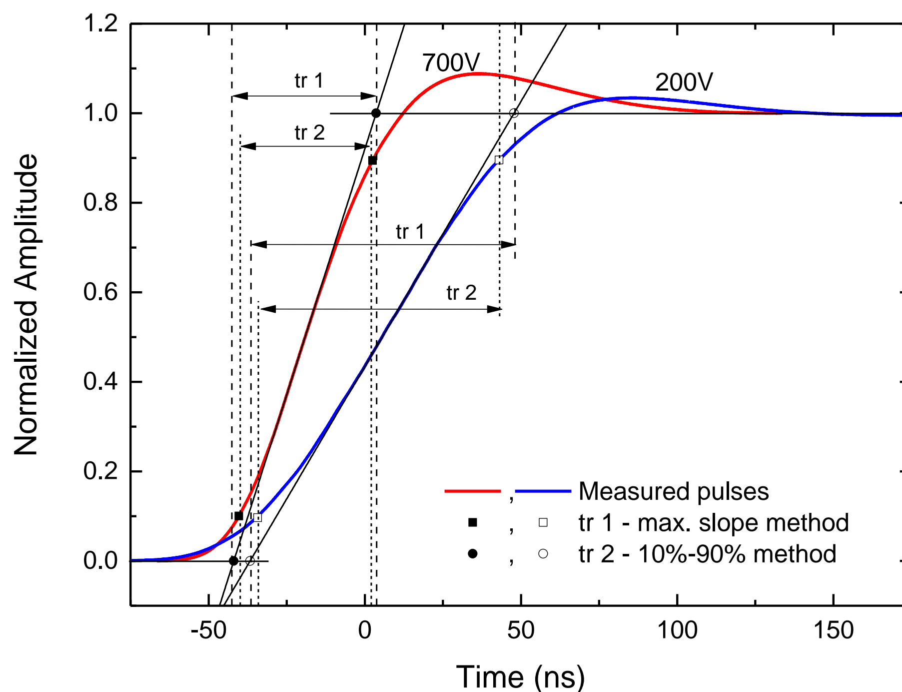

***Fig. 6.4** Transit time calculation methods in TChT measurement for 200V (blue) and 700V (red). t_{r1} is transit time determined by MSM and t_{r2} by 10 to 90 % method.*

The first method, denoted as a maximum slope method (MSM), was based on the straight line extrapolation of the rising edge in the point of inflection, so that the transit time is defined as an interval between points of intersection of the extrapolation line with the steady state and minimum amplitude of the normalized pulse. The second method of the transit time determination was based on the matching 10 to 90 % of the pulse rising edge, which is a standard rise time evaluation approach in electronics.

Two types of charge sensitive amplifiers were examined in order to assess the influence of detection electronic transfer characteristics on the detected pulse shape and calculated mobility value. Calculated average electron mobility for both detectors determined from TCT and TChT measurement is presented in Fig. 6.5 and Fig. 6.6, respectively. The electron mobility evaluated from TCT measurement is almost constant and reaches the value about 1070 cm^2/Vs for both detectors in the whole bias interval. This value is in a good correspondence with the theoretical room temperature mobility value of CdZnTe which is slightly higher than mobility of CdTe itself [91]. Direct comparison of the mobility with experiment is difficult due to scatter of accessible data $\mu = 1000$ cm^2/Vs [8]; 950 cm^2/Vs [92]; 1350 cm^2/Vs [93] and 1120 cm^2/Vs [94]. The lower mobility in [8] and [92] determined by TCT could be also affected by carrier trapping and detrapping on shallow traps, which delays the transit of carriers through the sample.

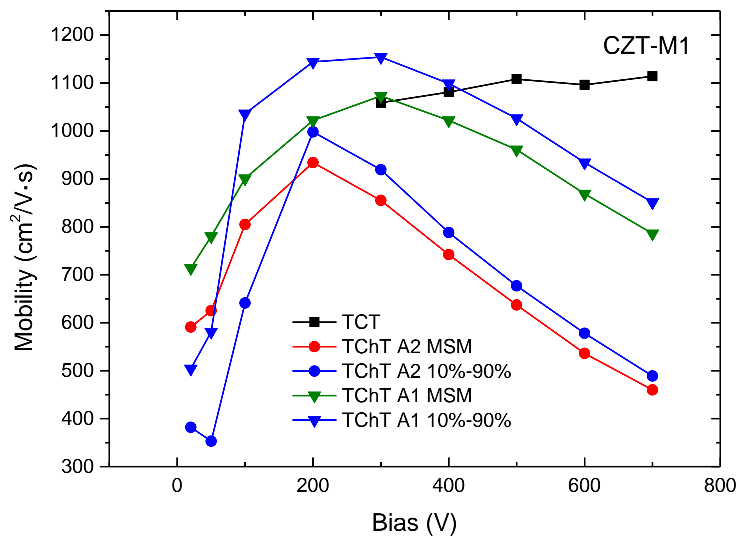

Fig. 6.5 *Bias dependence of electron mobility for CZT-M1 detector measured by A1 and A2 amplifiers, respectively, and evaluated by MSM and 10%-90% methods.*

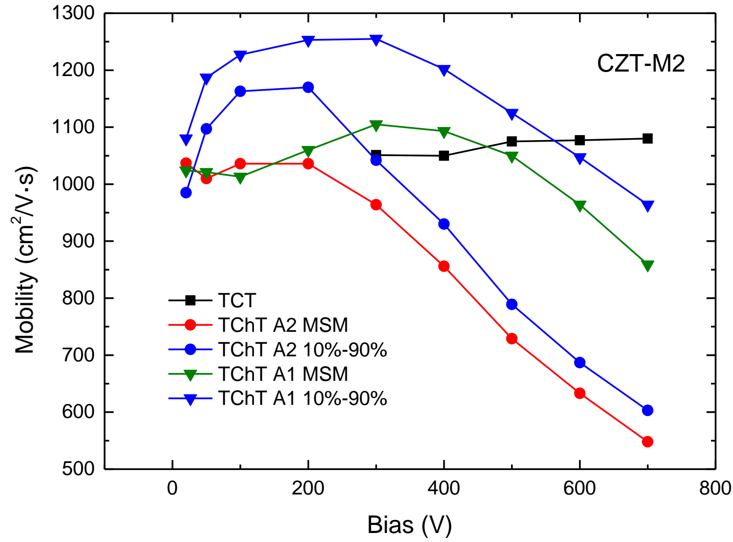

Fig. 6.6 *Bias dependence of electron mobility for CZT-M2 detector measured by A1 and A2 amplifiers, respectively, and evaluated by MSM and 10%-90% methods.*

In case of TChT the mobility ranges from 400 to 1220 cm^2/Vs so that no reliable average value can be determined. Electron mobility rapidly decreases with increasing detector bias for both detectors due to limitation of the frequency response of both amplifiers. Surprisingly, it also decreases (markedly for CZT-M1) from some 200 V to 20 V most probably due to the space charge formation and possible polarization of the sample [95] and to a strong plasma effect which yields evaluation error [8]. The mobility at low bias could not be checked by TCT because the signal of TCT was lower than the noise level. It is evident that, in contrast to TCT, the correct mobility may hardly be evaluated by TChT. Relatively weak deviation from the TCT value may be obtained at medium biasing, about 200 V – 300 V in our samples, where the extended transit time enables the circuit to produce a sufficiently fast response to the charge collection signal. The 10%-90% method yields mobility mostly greater than MSM; similarly, the circuit with preamplifier A1 provides mobility mostly greater than A2. It is suggested taking the maximum mobility determined with the A1 preamplifier and evaluated by the MSM for the most credible determination of mobility.

The summary of both samples mobility evaluated by MSM using both amplifiers is plotted in Fig. 6.7. At high bias above 300 V the error of the determined

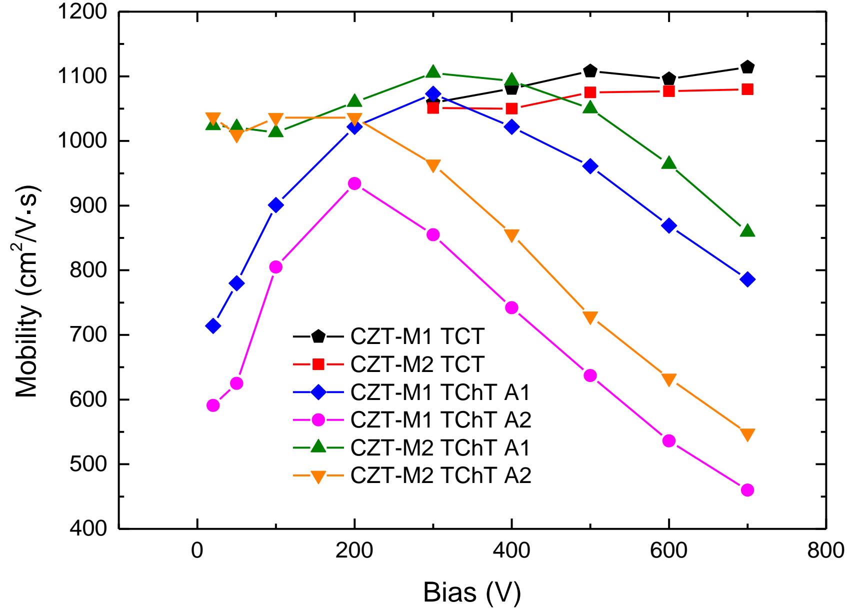

Fig. 6.7 *Bias dependence of electron mobility for A1 and A2 amplifiers and CZT-M1, M2 detectors using TCT and TChT (MSM) methods.*

mobility is seen to be significantly affected by the amplifier choice, since here A1 produces better mobility values than A2. The mobility depression is more significant for a thin detector with shorter transit time (CZT-M1) than for the thicker one (CZT-M2). The mobility obtained at low biasing splits between respective detectors M1 and M2 due to probably different internal properties of the detectors mentioned above. The selection of amplifiers has no large effect on the evaluated mobility at low bias. For both CZT-M1 and -M2 samples, the mobility values measured by TCT show a slight increase with increasing bias voltage. This effect could be explained by the Poole–Frenkel effect (PFE), which leads to a decrease of trap potential with increasing electric field and results in a faster carriers detrapping. In CdTe the PFE was nicely demonstrated for holes [12]. In this experimental setup the mobility enhancement is too weak to identify it reliably as the PFE. The decision on the contribution of PFE might be done by performing measurements at larger bias and at reduced temperature.

6.2. Laser-induced transient current pulse shape formation in Cd(Zn)Te planar detectors

As it was shown in previous chapters, TCT can be successfully used as a method for determining the drift velocity and electric field profiles in semiconductor detectors. Nevertheless, non-synchronized sources as alpha particles (α-TCT) used for generation of electron-hole pairs does not provide favourable signal to noise ratio.

Compared to that, laser-induced transient-current-technique (L-TCT) [42], [96], [97] offers more benefits. This fact is mainly due to the possibility of direct oscilloscope triggering derived from the excitation pulse and exact focusing of the laser beam on a specific detector spot area. Using this technique, even very low detector bias L–TCT electron signal may be recorded (down to approximately few voltages for CdZnTe detectors standardly used in our laboratory) so that the mobility–lifetime product and electric field profile can be determined for a very wide bias range.

It also has to be point out that measurements of the mobility by α-TCT are less precise than those done by the L-TCT. The indistinct oscilloscope trigger and plasma effects in the alpha particle excitation involve an additional uncertainty in the transit time determination and results in a lower accuracy of the evaluated mobility (estimated error is ~ 3%). The plasma effect that results in stretching the leading edge of the pulse is presented in Fig. 6.8 and is discussed in chapter 3.3.1.

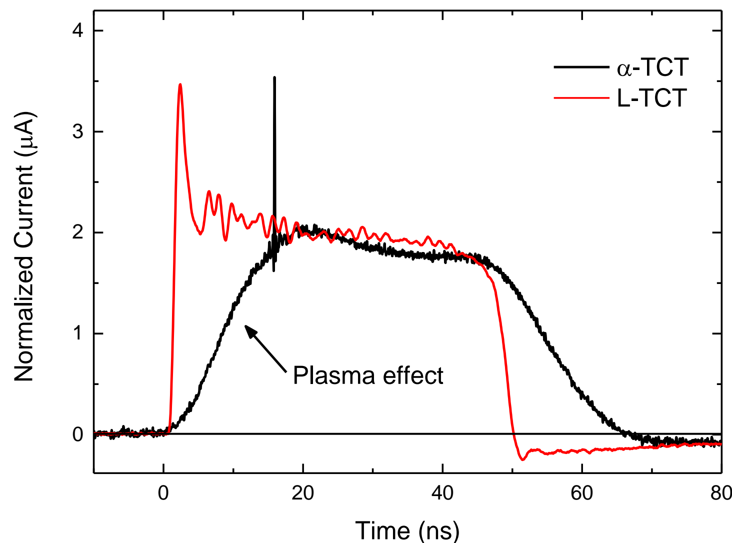

***Fig. 6.8** Comparison of α-TCT and L-TCT current waveforms at the same bias.*

On the other hand, in case of excitation using light with above band–gap energy with thin penetration depth ~ 0.36 μm [98], [99] entails the warping of TCT current waveforms (CWFs) by surface effects like surface recombination [42], [100] and surface photo-voltage [101]. Consequently, the mobility–lifetime product cannot be calculated simply from the standard Hecht equation fitting – equation (3.4) and a modified Hecht equation must be applied. Moreover, the processing of signal by additive electronics commonly results in debasement of CWFs. An attempt to revise this deficiency and to retrieve the original current waveforms was reported in [89].

Planar CZT detector with 12 % of Zn with dimensions of 5 × 5 × 1.2 mm^3 was used for investigation in this work. It is labelled as CZT-D1. Au/Au electrodes were prepared on larger sides by electroless deposition using aqueous 1 % $AuCl_3$ solution.

Detector transport properties were investigated using the modified L-TCT setup presented in Fig. 6.9, where the detector is irradiated using pulsed laser diode (660 nm wavelength, 300 mW maximum pulse peak power, 3 ns pulse width as FWHM, 200 ps rise and fall time, 3 mm^2 focal spot area). Laser diode is powered by an ultrafast pulse generator (Picosecond Pulse Labs 10 070A) with variable pulse width and repetition rate. The laser pulse shape is directly monitored by the ultrafast GaAs photodiode (Alphalas, 25 GHz bandwidth). Collimation optics and a translation stage were used to focus the laser beam onto the examined spot in the detector plane.

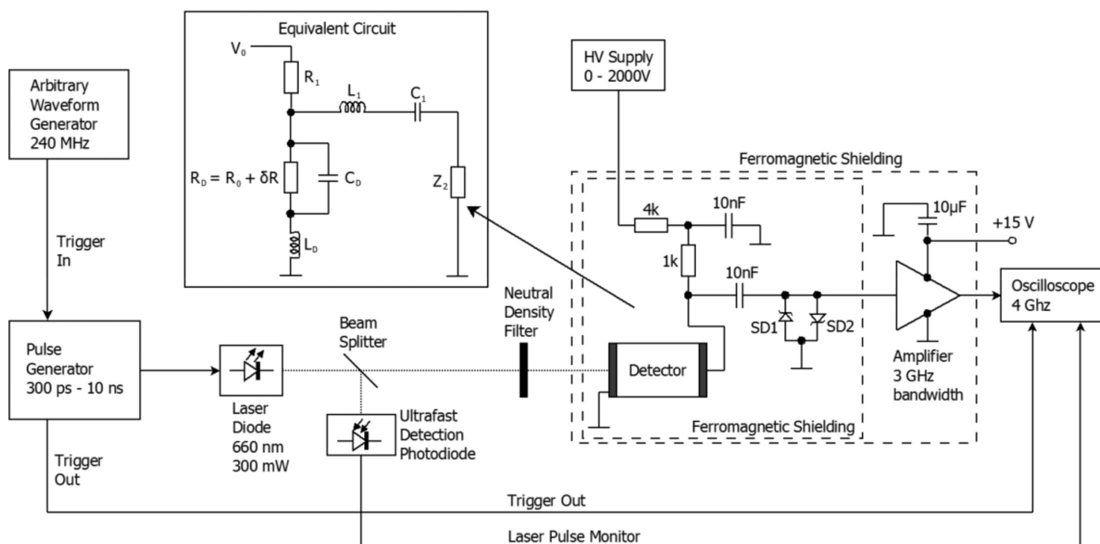

Fig. 6.9 *Block diagram of the laser excited TCT pulse detection electronics. Inset: equivalent circuit representing the detector and the amplifier input.*

Neutral density disc filter is placed in the beam line for variable intensity attenuation of the laser pulse. In the present results laser pulses with the output energy of 0.4 nJ and 100 Hz repetition rate were used to induce all CWFs in the detector and this light intensity did not disturb internal electric field. Generated current pulses are amplified using direct high frequency voltage amplification [8], [102] (L–3 Narda–Miteq AM–1607–3000, Gain = 132, DC input impedance of 50 Ω, frequency bandwidth up to 3 GHz) and recorded by an ultrafast digital sampling oscilloscope (LeCroy WaveRunner 640Zi, 40 Gs/s, resolution up to 11 bits, 4 GHz bandwidth, 50 Ω DC input impedance) for further processing. Equivalent lumped parameters circuit comprising passive components representing electrical characteristics of the detector and the amplifier input impedance is shown in the inset of Fig. 6.9. L-TCT electron signal was measured in a wide bias range (from 50 V to 700 V) very reliably since the transient CWF signal to noise ratio is highly favourable, mainly due to direct oscilloscope triggering and subsequent CWF amplification.

An experimental setup was built for measuring the detector transport properties under regular operating conditions. An Iseg SHQ122M for high voltage biasing (0-2000 V) was used in the measurement. In case of the high voltage applied on the detector, it cannot be directly connected to the amplifier or the oscilloscope 50 Ω DC input because of an input damage. The oscilloscope input has to be detached by the decoupling capacitance C_1 = 10 nF and the antiparallel Schottky diodes are also used for peak voltage protection of the amplifier. However, the decoupling capacity strongly affects the shape of CWF, especially the shape of the plateau and the falling edge and causes the CWF negative overshooting at the end of the falling edge. Therefore a deconvolution of the measured CWF with the instrument transfer function was applied to get the original shape of CWF. A detector equivalent circuit (DEC) comprised of 1 GΩ resistance and 2 pF capacity in parallel connection in place of the detector powered by the waveform generator (Tektronix AFG3252) replacing HV supply input is used for the determination of the instrument transfer function.

Characteristic L–TCT electron CWFs of studied CZT-D1 detector biased with 50 V – 700 V are shown in Fig. 6.10. It may be seen well resolved CWFs with transit time scaling with bias. Parasitic weak oscillations with the same shape and characteristic frequency ≈ 600 MHz and with predominant initial peak together with the falling edge negative overshooting are apparent at each CWF. Moreover, a very similar pattern was observed even at the zero bias L–TCT CWF, see Fig. 6.11. With

the aim to explore the effect more deeply, it has been performed the L–TCT measurements of the detector without ($L_D = 5$ nH) or with an additional series induction (short coiled copper wire with induction L_1 =30 nH or 100 nH) to simulate the influence of the parasitic inductance on the CWF shape, see the inset in Fig. 6.10. As seen in Fig. 6.12, the additional inductance manifests in the appearance of damped oscillations at lower frequency.

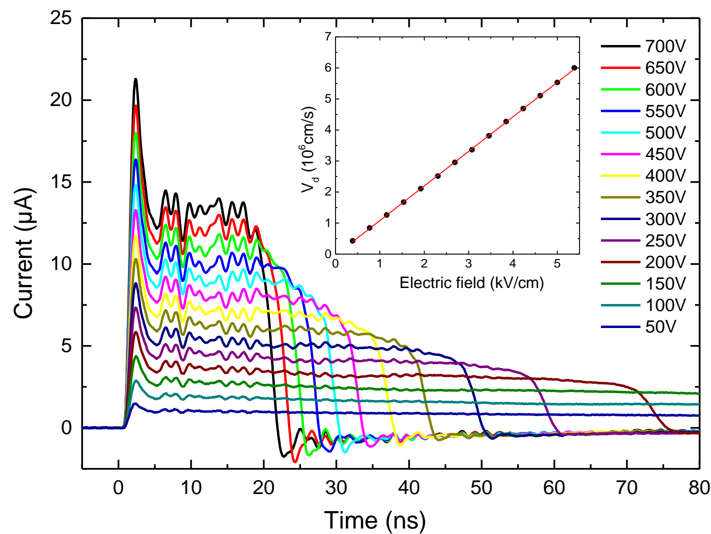

***Fig. 6.10** L–TCT current waveforms for CZT-D1 detector for different biases 50 V – 700 V. Note the same shape and period of weak oscillations apparent in each waveform. Inset shows the electron drift velocity versus applied electric field determined by the pulse shape double exponential fit* [102]. *Evaluated electron drift mobility is μ =1010 cm²/V.*

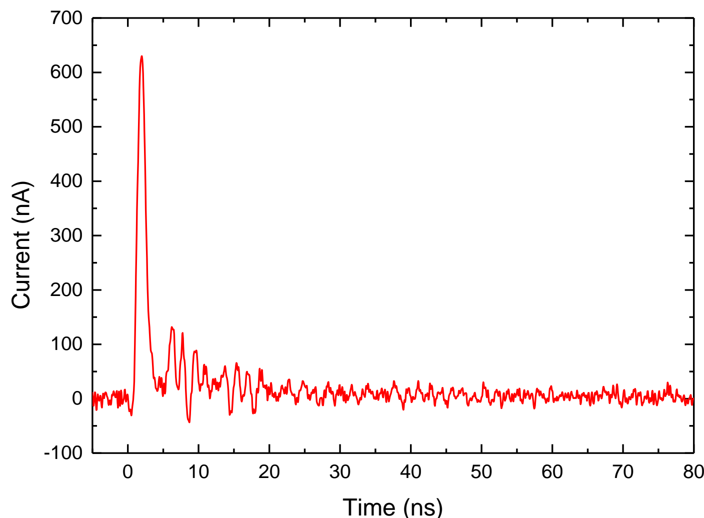

***Fig. 6.11** Induced transient photocurrent at zero applied bias for CZT-D1 detector.*

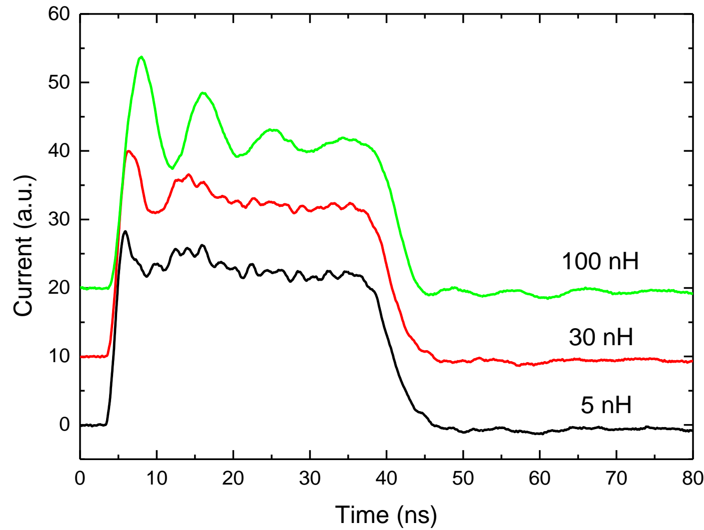

***Fig. 6.12** L–TCT current waveform shape dependence on the detector parasitic induction. Black line (5 nH) – no additive inductance connected to the detector, red (30 nH) and green (100 nH) lines – increasing additive inductance.*

Though the amplitude of parasitic oscillations damps, they persist and may be detected even in case of the highest induction value L_1 = 100 nH. Thus it can be concluded that the parasitic oscillations are not activated by an unrevealed inductance in the detector-related part of the circuit. They should stem from the electronic circuit and from the sampling noise of the oscilloscope. It was found that the initial laser pulse creates a very short photocurrent pulse which slightly destabilizes the detector electronics and is manifested in the initial peak and slowly damped oscillations connected with the whole RLC resonance circuit involving internal resistance, inductance and capacitance of the detector, amplifier and other electronic elements (filtering and decoupling capacitors and wiring). On the other hand, the negative overshooting of the falling edge is caused by the time constant of the serial RC circuit comprising filtering resistor R_1, decoupling capacitor C_1, the amplifier and 50 Ω DC input impedance of the oscilloscope.

6.2.1. Restoration of real current waveform shape

The TCT CWF is warped by passing of the signal through the electronic setup depicted in the block diagram in Fig. 6.9, mainly by the amplifier. The process is ruled by the amplifier, decoupling capacitor C_1 and additive electronics, which entails gradual damping of the current detected during the charge transfer through the sample

and the reversed current due to capacitors discharging after the majority of charge reaches the electrodes. Mathematically, the decayed current $j(t)$ is expressed by a convolution of the source function j_0 with the device transfer function characterizing the setup in the form

$$j(t) = \int_{-\infty}^{t} j_0(t')g(t - t')dt'. \tag{6.3}$$

With the aim to restore the right input signal it have been determined g by measuring the TCT signal $j_s(t)$ of DEC. The normalized response signal $j_s(t)/J_{s0}$ of the electronic setup with the DEC induced by a well–defined single step current pulse $j_{0s}(t) = J_{s0}\Theta(t)$, where $\Theta(t)$ is step function, is shown in Fig. 6.13. The response signal can be conveniently fitted by a quadruple–exponential function

$$j_{s,fit}(t) = \Theta(t) \sum_{m=1}^{4} a_m e^{-\frac{t}{\tau_m}} \tag{6.4}$$

where a_1 = 0.414, τ_1 = 34.2 μs, a_2 = 0.310, τ_2 = 3.6 μs, a_3 = 0.145, τ_3 = 379 ns, a_4 = 0.131, τ_4 = 20 ns.

On measuring j_s, it may be directly deduce the device transfer function

$$g(t) = \frac{1}{J_{s0}} \frac{dj_s(t)}{dt} = \delta(t) - \Theta(t) \sum_{m=1}^{4} \frac{a_m}{\tau_m} e^{-\frac{t}{\tau_m}} \tag{6.5}$$

in which δ(t) is the Dirac function. Keep on mind that $\int_{-\infty}^{\infty} \delta(t)dt = 0$. A few examples of $j(t)$ arising from originally constant $j_0(t)$ pulse for different injected model transit time t_r are shown in Fig. 6.14. The revealed transfer function corresponds to the equivalent scheme of the circuit delineated in Fig. 6.15, where R_1 = 5 kΩ and C_1 = 10 nF are fixed by the scheme in Fig. 6.9. Applying obvious linear algebra to solve electrical circuits, single elements of the circuit were calculated as follows: R_2 = 3.63 kΩ, C_2 = 1.62 nF, R_3 = 1.02 kΩ, C_3 = 442 pF, R_4 = 734 Ω, C_4 = 31 pF and C_5 = 4.42 nF. The remaining impedance Z is responsible for the high–frequency oscillations discussed in Fig. 6.10–Fig. 6.12 and it was omitted in the calculations here. Substituting g, eq. (6.3) may be conveniently adapted to the form of linear Volterra

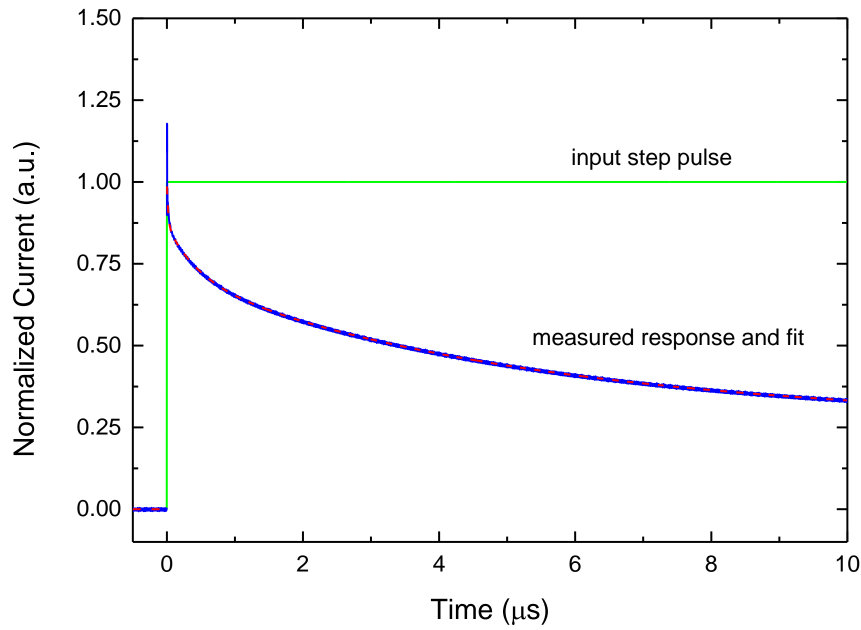

Fig. 6.13 *Normalized response of the electronic setup on the single step pulse in the input. Solid and dashed lines represent the input single step function, measured response on the output and the fit by a quadruple–exponential function (eq. (6.4)), respectively. Difference between the fit and the pulse is negligible in the whole fitting interval except a slight shift close to the beginning of the pulse.*

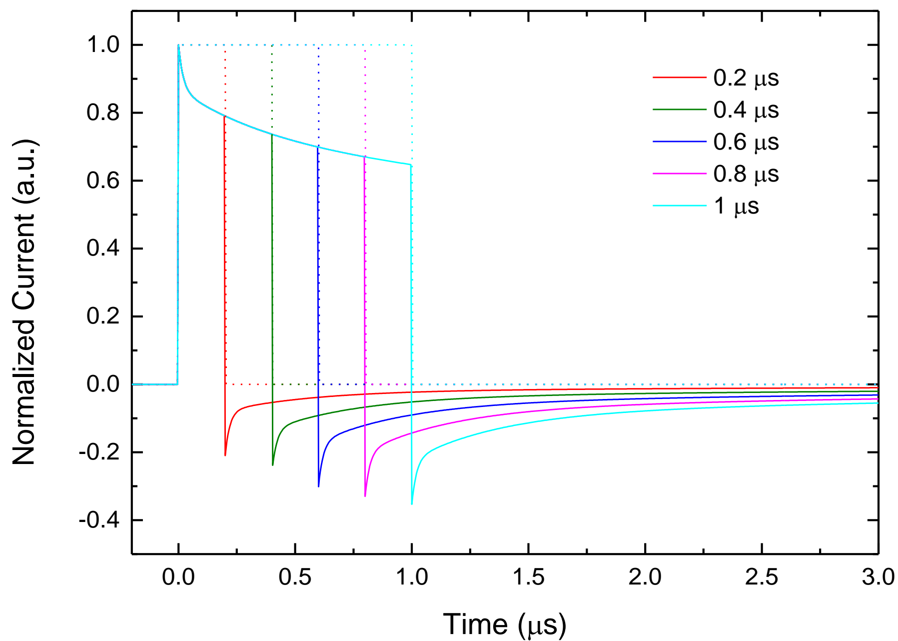

Fig. 6.14 *Convolution of constant CWFs $j_0(t)$ with $g(t)$ defined in eq. (6.5). Full and dotted lines plot $j(t)$ and $j_0(t)$ for the transit time t_r = 0.2, 0.4, 0.6, 0.8, 1.0 μs, respectively.*

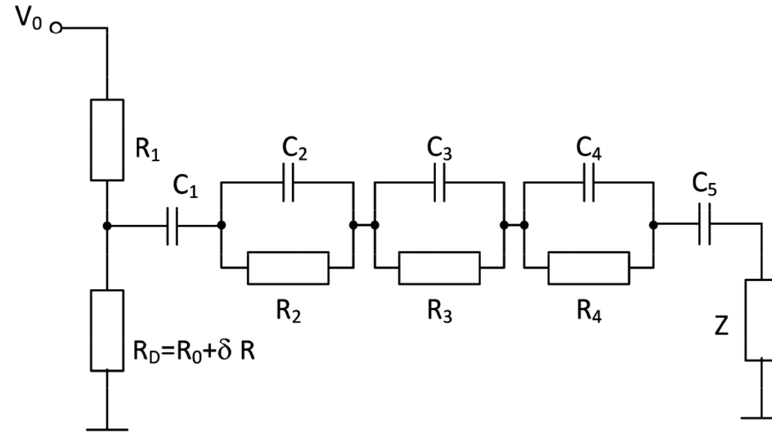

Fig. 6.15 *Detector and the electronic equivalent circuit scheme of the transfer function.*

integral equation of the second kind [103]

$$j_0(t) = j(t) + \sum_{m=1}^{4} \frac{a_m}{\tau_m} \int_0^t j_0(t')\, e^{-\frac{t'-t}{\tau_m}}\, dt' \qquad (6.6)$$

where the illumination is assumed at $t \geq 0$ and $j(t < 0) = 0$. Equation (6.6) is routinely solved numerically [101]. The functional application of the algorithm suffers, however, from the data extension describing the CWF, which typically exceeds 10^5 data points. The manipulation with a square matrix of such order makes this process impracticable. To effectively solve eq. (6.6), it has been engaged two other methods allowing a much simpler determination of j_0.

A-1. Van Cittert's Method: The straightforward solution of eq. (6.6) may be searched by the iteration loop taking as an initial guess in the integral in the right hand side of eq. (6.6). This approach to solving integral equations is named Van Cittert deconvolution method [104], [105]. The procedure is stable and converges fast within a time scale of minutes on common PC.

A-2. Direct Recurrent Method (DRM): Thanks to the simple quadruple–exponential form of g, it may be separated the *t* and *t'* parts in g. Consequently, the huge matrix used in [103] may be substituted by three one–dimensional arrays. Assuming the numerical integration by the trapezoidal method, eq. (6.6) may be converted into the form

$$j_0(t_i) = \frac{1}{1 - \frac{\Delta t}{2}\sum_{m=1}^{4}\frac{a_m}{\tau_m}} \times \left[j(t_i) + \sum_{m=1}^{4} \frac{a_m}{\tau_m} e^{-\frac{t_i}{\tau_m}} I_m(t_{i-1}) \right] \qquad (6.7)$$

where t_i is the i-th time point and Δt is the time step. Integrals I_m are expressed as

$$I_m(t_{i-1}) = I_m(t_{i-2}) + j_0(t_{i-1}) e^{\frac{t_{i-1}}{\tau_m}} \Delta t. \qquad (6.8)$$

This approach allows direct calculation of $j_0(t_i)$, as the right hand side of eq. (6.7) involves j_0 in the retarded time $t_j < t_i$ only. The procedure is much faster than the van Cittert's method. The numerical stability is, however, worse than in the previous method and the approach may be used only if t does not exceed significantly the lowest value of τ_m. The DRM method is henceforth used in the restoration of j_0.

Before calculating of restored real CWFs, the DRM was tested on model input current pulses (2.5 ns for both leading and falling edge, 50 mV output with 36 dB attenuator) created by the waveform generator using DEC substituting the detector.

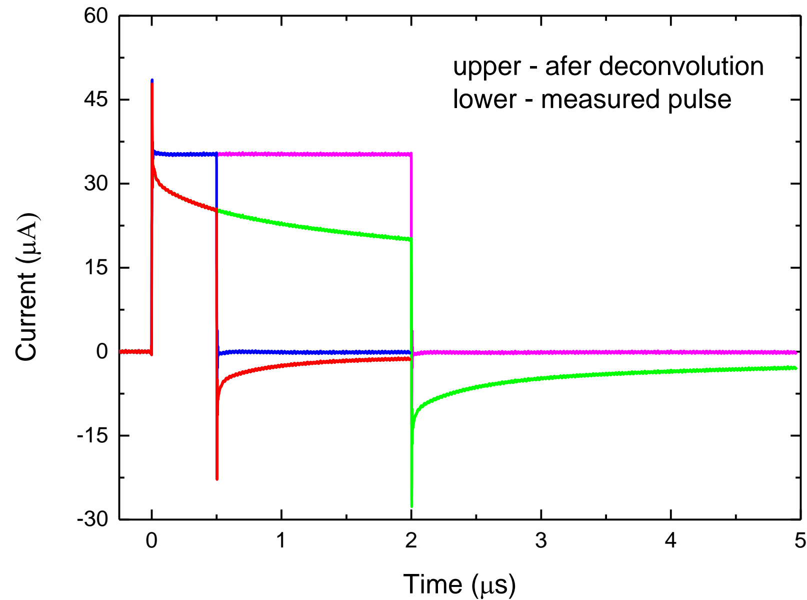

Fig. 6.16 *Deconvolution of rectangular pulses with 500 ns and 2μs duration. Bottom curved pulses (red, green) are measured, upper step–like pulses (blue, magenta) are restored.*

The measured restored 500 ns and 2 μs long pulses are shown in Fig. 6.16. The restored pulses are seen to correspond very well to the original rectangular pulses not only during the pulse duration but also after switching off the current. Small deflections remained at the steep changes of the pulses.

Examples of restored CWFs are shown in Fig. 6.17. A low bias was used intentionally since the warping of transients in this case is pronounced. The restored CWFs reveal less declining slope without negative overshooting compared to measured $j(t)$, which implies that reduced positive space charge then might be deduced from measured CWFs. Reciprocally, in case of negatively charged detectors characterized by ascending CWF the reconstruction would result in enhanced CWF. In case of holes collection at anode illumination, the statements would be opposite. The correction to the space charge density evaluated according to [8] reaches 10^9 cm^{-3} for CWFs with $t_r \approx 1$ μs and increases up to 3×10^{10} cm^{-3} at short $t_r < 20$ ns. The exact magnitude of the space charge correction depends on the transfer function. Other setups may lead to both smaller and larger effects.

The maximum collected charge about q_c = 280 fC apparent in Fig. 6.18 induces additional screening of applied bias. Taking the spot area S = 3 mm^2 and the detector thickness, the electric field induced between electron–hole clouds reaches 10 V/cm, which is much less than the electric field 200 V/cm applied at the lowest measured bias of 25 V. The screening field induces weak depression/enhancement of CWF at its

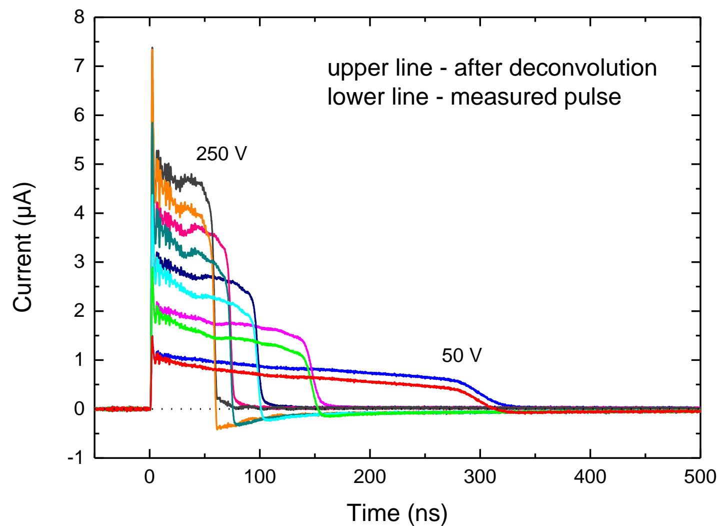

Fig. 6.17 *Comparison of measured and restored CWFs for 50 V–250 V biasing.*

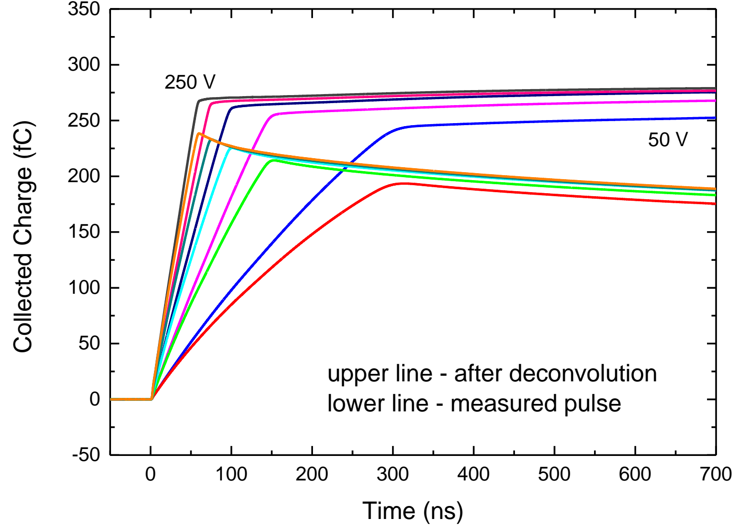

Fig. 6.18 *Temporal dependence of collected charge calculated for measured (lower lines) and restored (upper lines) current waveforms for bias in the interval 50 V-250 V.*

early/final part. For the quantities used in this chapter the space charge deviation calculated from such weakly warped CWF by the exponential fit of CWF [8] manifests in a seeming additional negative space charge with the density $\rho_s = 2q_c/(e{\cdot}L{\cdot}S) = 8 \times 10^8$ cm^{-3} homogeneously spread in the detector. This amount should be subtracted from calculated space charge to refine the results.

6.2.2. Charge collection efficiency set by L-TCT

CCE is an important quantity to be determined by the TCT. At low biasing the transit time t_r increases and becomes comparable to the decay time of $g(t)$; τ_m. As we may see in Fig. 6.14, the CWF is damped by the charging of coupling capacitor C_2 and becomes negative after principal portion of charge has been collected on contacts. The calculation of CCE by the straightforward integration of $j(t)$ is then worsened by ambiguous choice of a representative procedure to deduce CCE. The restoration of original CWF allows a significant refinement of the collected charge Q deduced directly from $j_0(t)$ via

$$Q(V) = \int_0^\infty j_0(t)\,\mathrm{dt}. \tag{6.9}$$

In view of the fact that $j_0(t)$ is principally positive and damps fast at $t > t_r$, Q becomes a well–defined unique quantity. The process of charge collection is conveniently expressed by eq. (6.2) (where $i = j$) as outlined in Fig. 6.18, which clearly points to an improvement in the determination of $Q(V) = q(V, t = \infty)$.

The obvious way to determine the mobility-lifetime product, which is the most common quantity characterizing the detector quality, is the fit of CCE(V) by the standard Hecht equation expressed in case of cathode illumination and electron collection in the form of equation (3.4).

Arrangement of the spectroscopic measurement using the charge sensitive preamplifier, shaping amplifier, multichannel analyzer and laser-diode (660 nm) as a source operating under the same conditions as in L-TCT was used for comparison of the results. In Fig. 6.19 the bias dependences of CCE(V) calculated using eq. (6.9) and CCE(V) evaluated from the bias dependence of the photo–peak position in laser–induced pulse height spectrum analysis (L-spect) are shown. Both dependences were fitted by standard Hecht equation (3.4). The fitted electron mobility–lifetime product is $\mu_e\tau_e = 1.52 \times 10^{-3}$ cm^2/V in case of L-spect and $\mu_e\tau_e = 1.44 \times 10^{-3}$ cm^2/V in case of L-TCT.

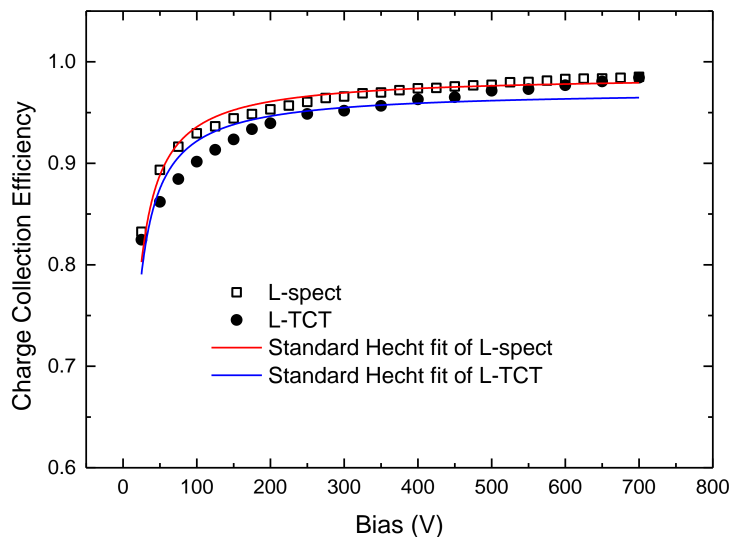

Fig. 6.19 *Charge collection efficiency of laser–induced electron waveforms derived from laser–excited transient charge technique pulse height spectra (black open squares) and calculated according to eq. (6.9) (black circles). Full lines plot the fits of L-spect (red) and L-TCT (blue) using eq. (3.4).*

An analogous procedure applied on measured CWFs without deconvolution by fitting maximum collected charge at each bias provides $\mu_e\tau_e = 5.2 \times 10^{-4}$ cm^2/V. The large deviation of this value from that obtained after deconvolution clearly proves the necessity of the incorporation of deconvolution procedure for getting relevant data in L-TCT.

6.2.3. Mobility-lifetime product set by L-TCT

As one can see in Fig. 6.19 the standard Hecht equation (3.4) does not precisely fit the measured data. This is caused by high surface recombination in case of the sample illumination by above bandgap light (660 nm ~ 1.88 eV) [100]. To prove this statement another planar CZT detector with ~ 10 % of Zn with dimensions of $5 \times 5 \times 3.2$ mm^3 was used for determination of μτ product (CZT-D2). The Au/Au electrodes were prepared the same way as the first sample – by electroless deposition using aqueous 1 % solution. The CCE depending on applied bias was set by alpha, low energy gamma and laser-induced pulse height spectrum analysis (L-spect) by the measuring setup described in chapter 3.2.1 and also by L-TCT.

In the case of sample irradiation by alpha particles or low energy gamma radiation, the incident particles/radiation is absorbed in units (alpha) to tens (gamma) micrometres inside the sample. Therefore in this case, the surface recombination can be neglected and the μτ product can be determined via *Standard Hecht* equation – eq. (3.4). On the other hand, in case of alpha particle irradiation, the plasma effect plays a significant role (especially at lower biasing) as it was discussed at the chapter 3.3.1 and it is shown in Fig. 6.8. Thus we can obtain lower value of μτ product. In the case of low energy gamma radiation, the longest penetration depth of the radiation (up to 10 % of the sample width) can influence the determined μτ product, as it is set by eq. (3.4) from the beginning of the sample. Thus in gamma pulse height spectrum analysis the determined μτ product value is higher than the real one.

When the μτ product is determined from L-spect or L-TCT, both plasma effect and long penetration depth can be neglected by low intensity of above bandgap energy light illumination. But the *Standard Hecht* equation (eq. (3.4)) has to be modified of surface recombination. As the steady-state continuity equation for a single carrier is given as

$$G(z) - \frac{N(z)}{\tau(z)} - \mu N(z)\frac{dE(z)}{dz} - \mu E(z)\frac{dN(z)}{dz} + D\frac{d^2N(z)}{dz^2} = 0 \qquad (6.10)$$

where $G(z)$ is carrier generation rate in z, $N(z)$ is photon induced carrier density at z; $\tau(z)$ is carrier lifetime at z; μ carrier mobility; $E(z)$ is electric field at z; and D is carrier diffusion constant. Light is illuminating the sample at $z = 0$ and the width of the sample is w.

The diffusion current is usually negligible compared with the drift current. The electric field is assumed to be uniform and the carrier lifetime is further assumed to be independent of position, so the equation is simplified to

$$G(z) - \frac{N(z)}{\tau} - \mu E\frac{dN(z)}{dz} = 0. \qquad (6.11)$$

The light is assumed to be uniformly absorbed through the crystal, so $G(z)$ is independent of position, $G(z) = G$. If light is assumed to be completely absorbed at the surface, then $G(0) = G_s$ (which takes a part in Q_0) and $G(z) = 0$ for $z > 0$. Under this condition, the CCE is obtained as

$$CCE = \frac{Q}{Q_0} = \frac{1}{1 + \frac{s}{\mu E}}\frac{\mu\tau E}{w}\left[1 - \exp\left(-\frac{w}{\mu\tau E}\right)\right]. \qquad (6.12)$$

Here, s is the surface recombination velocity, which is inversely proportional to the carrier surface lifetime [106]. This *Surface Hecht* equation becomes the *Standard Hecht* equation for $s = 0$.

CCE measured in the L-spect and L-TCT mode in CZT-D2 detector together with *Standard Hecht* (eq. (3.4)) and *Surface Hecht* (eq. (6.12)) fits are shown in Fig. 6.20. Dash lines are fits for L-TCT and straight lines are fits for L-spect.

It is clearly visible that *Surface Hecht* equation fits the obtained data more precisely than *Standard Hecht* equation. And what more, the obtained values of $\mu\tau$ product determined by *Surface Hecht* equation are in good corellation with additional measurements. The comparison of $\mu\tau$ product determined by all four measurements is in Table 6.1. There, it is obvious that $\mu\tau$ product determined via *Surface Hecht* equation in case of laser illumination has the similar value as $\mu\tau$ product determined by alpha or gamma spectroscopy.

As the alpha particle pulse height spectrum analysis is nowadays the most used method for determination of the μτ product it was also employed on the sample CZT-D1. The μτ determined by alpha spectroscopy is set as $\mu\tau = 1.41 \times 10^{-3}$ cm^2/V

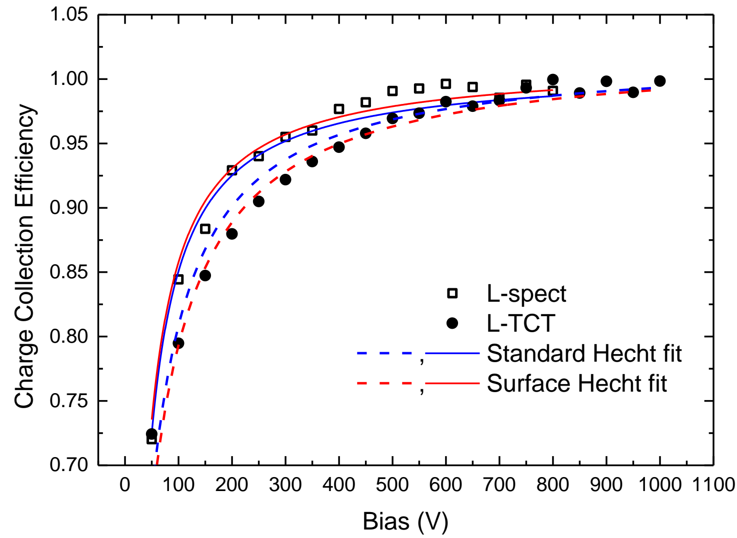

Fig. 6.20 *Collected charge as a function of the applied bias on CZT-D2 sample for L-spect and L-TCT methods with Standard Hecht (eq. (3.4)) and Surface Hecht (eq. (6.12)) fits of data. Dash lines are fits for L-TCT and straight lines are fits for L-spect.*

Methodology	**Used fit**	$\mu\tau$ **(CZT-D2)**	$\mu\tau$ **(CZT-D1)**
Alpha spectroscopy	Standard Hecht	9.40×10^{-3} cm^2/V	1.41×10^{-3} cm^2/V
Gamma spectroscopy	Standard Hecht	9.80×10^{-3} cm^2/V	-
L-spectroscopy	Standard Hecht	2.83×10^{-3} cm^2/V	-
L-TCT	Standard Hecht	1.34×10^{-3} cm^2/V	1.44×10^{-3} cm^2/V
L-spectroscopy	Surface Hecht	9.71×10^{-3} cm^2/V	-
L-TCT	Surface Hecht	9.66×10^{-3} cm^2/V	1.49×10^{-3} cm^2/V

Table 6.1 *Electron mobility-lifetime product determined on CZT-D2 and CZT-D1 samples by alpha, low energy gamma and laser-induced pulse height spectrum analysis and by L-TCT via Standard Hecht and Surface Hecht equation, respectively*

and the value from L-TCT set by *Surface Hecht* equation is $\mu\tau = 1.49 \times 10^{-3}$ cm^2/V. To remind, the fitted electron mobility–lifetime product via *Standard Hecht* equation is $\mu\tau = 1.44 \times 10^{-3}$ cm^2/V. The value determined by *Surface Hecht* or *Standard Hecht* equation in L-TCT measurement is very similar and both values are also very similar to the value determined by alpha spectroscopy. This can be caused by small surface recombination velocity [107], [108] in this sample when $s/\mu = 20$ V/cm, which is six time smaller than in case of CZT-D2.

6.3. Influence of the crystallography defects on the laser-induced transient current waveforms

Previous measurements were performed on samples without significant crystallographic defects. Therefore, $Cd_{0.9}Zn_{0.1}Te$ sample containing an unspecified defect was intentionally selected to determine its impact on CWFs. This sample, labelled as CZT-D3, had dimensions of $4.5 \times 4.5 \times 2.9$ mm^3. It was prepared by standard method – grinding in SiC abrasive, following with chemo-mechanical polishing in 3 % bromine-ethylene glycol solution made on a polishing kit on a silk pad and then the sample was further etched for about 30 seconds in a 3 % bromine-methanol solution. After all these surface treatments, the defect was recognized by infrared (IR) microscopy described in chapter 3.6.

The sample was characterized by IR microscopy from three sides close to the defect; contact side – A, right side – B and bottom side – C as it is shown in Fig. 6.21, Fig. 6.22 and Fig. 6.23, respectively. The defect was less noticeable on the side A, but it was clearly extending almost 600 μm inside the sample as it is seen from sample sides B (Fig. 6.22) and C (Fig. 6.23). No additional defects of such dimensions were found inside the sample. After the IR microscopy, the gold planar contacts were prepared from 1% $AuCl_3$ aqueous solution on the side A and its opposite side (side D) for further investigation of this sample.

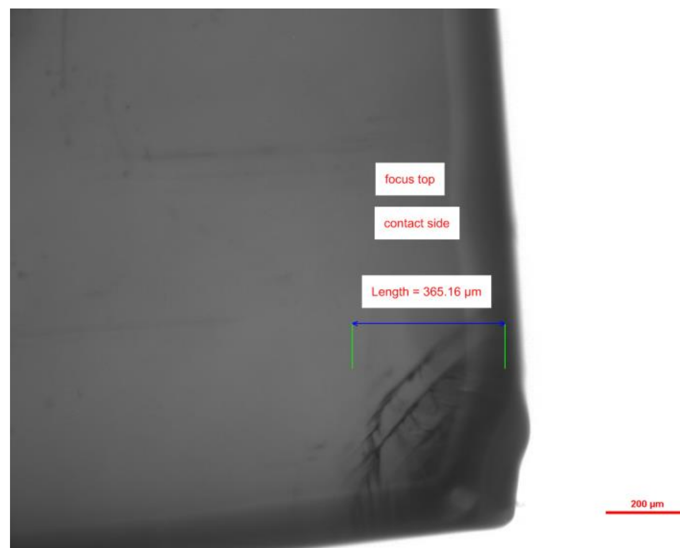

Fig. 6.21 *IR microscopy of the A-side (contact side) of the sample CZT-D3 showing the defect close to the corner of the sample.*

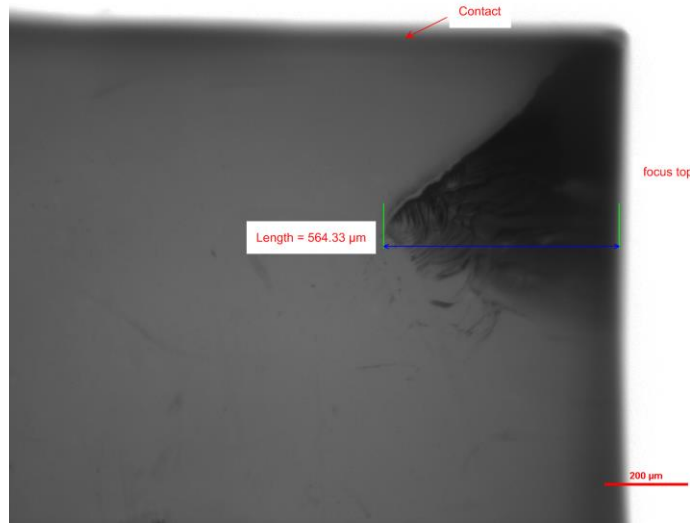

Fig. 6.22 *IR microscopy of the B-side (right side) of the sample CZT-D3 showing the defect close to the corner of the sample.*

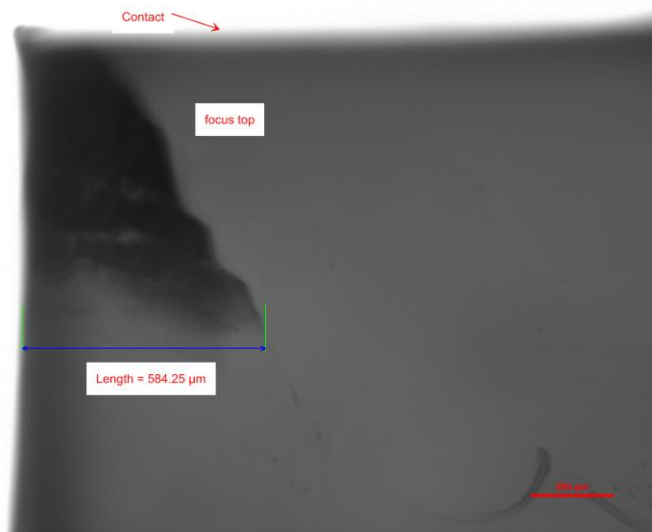

Fig. 6.23 *IR microscopy of the C-side (bottom side) of the sample CZT-D3 showing the defect close to the corner of the sample.*

The L-TCT setup shown in Fig. 6.9 was extended by XYZ translation stage with standard micrometres (resolution of 10 µm). The laser diode was attached on this stage which allows the precise setting of the illuminating spot of the incident laser beam on the sample. With this modification, it was possible to obtain 2D maps of current waveforms (CWFs) on the studied sample with resolution ≈ 800 µm which is given by the focal point area of laser diode. The mapping spots on the CZT-D sample are schematically shown in Fig. 6.24. It has been used standard illumination

wavelength of 660 nm, with repetition rate of 100 Hz. The sample bias was V_B = -300 V. The obtained results are shown in Fig. 6.25 (b), (c) and (d). After the sample mapping, the illuminating spot was defocused in order to illuminate the whole sample at once which allowed to obtain the mean CWFs depending on applied bias (Fig. 6.25 (a)). It must be stressed that it was illuminated the opposite side of side A. Therefore the influence of the defect should be reflected at the ending part of the CWFs.

The main effect of the defect was distortion of the inner electric field which is manifested as an increase of CWFs at the time around 200 ns [8]. This influence can be clearly seen in the bottom side of the sample – position x3y2 in Fig. 6.25 (c) and positions x2y2 and x4y2 in Fig. 6.25 (d) and is also clearly displayed on the right side of the sample – position x4y3 in Fig. 6.25 (b). This effect is also well demonstrated in Fig. 6.25 (a) when the whole sample was illuminated by laser light and the mean CWFs were recorded. Its influence was present for all biases but it is mostly expressed for the higher biases.

The other effect which is derived from the internal electric field distortion is the transit time extension. This extension is very well visible in Fig. 6.25 (d) for the

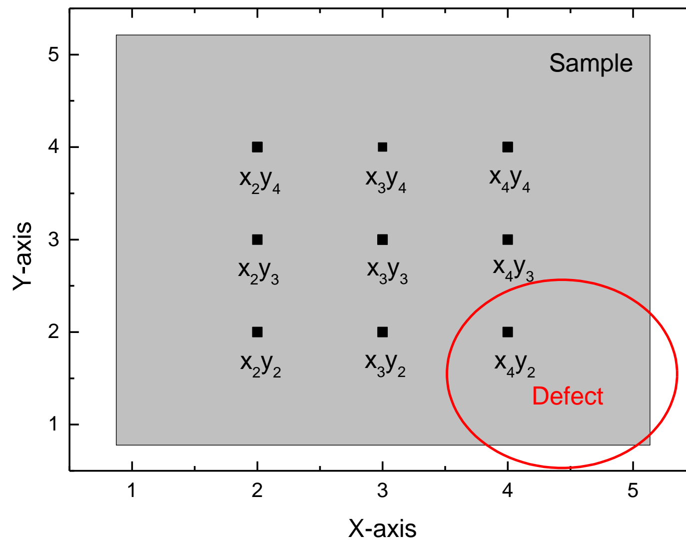

Fig. 6.24 *Schematic picture of the L-TCT mapping on side D of sample CZT-D3 for 9 spotting places. The grey rectangle represents the sample and the red circle depicts the region where the defect was located by IR microscopy.*

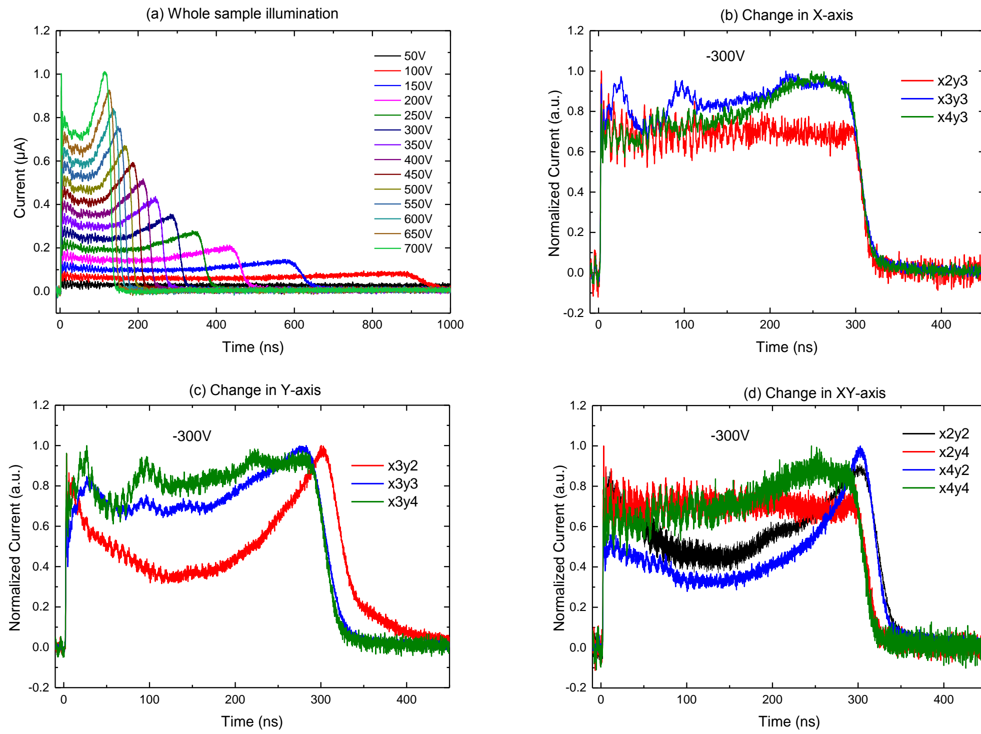

***Fig. 6.25** Transient current waveforms on sample CZT-D3 with inside defect for (a) whole sample illumination depending on applied bias and (b) different spotting in X-axis, (c) different spotting in Y-axis and (d) for four different spots in XY-axis at -300 V bias.*

positions x2y2 and x2y4 when the transit time of the electrons is ten nanoseconds longer than in two other displayed cases in this figure.

The spotting points near the sample boundaries were affected by the edge effects, when the illumination light shined not only perpendicular to the sample, but also on its edges. This results in distortions of the CWFs and it is very hard to express the edges influence, therefore only the points further from the edges were selected for examination and the sample edges were covered by mechanical mask in case of whole sample illumination measurements.

After this characterization, the sample was grinded in SiC abrasive on the side of the defect to the final thickness of 3.8 mm and the same surface treatment as at the beginning was applied. After this defect removal, there was nothing extraordinary to find on IR microscopy. Therefore the same gold contacts were prepared and the sample was characterized by L-TCT again. The obtained results are shown in Fig. 6.26 (a), (b) and (c) for different spots on the sample.

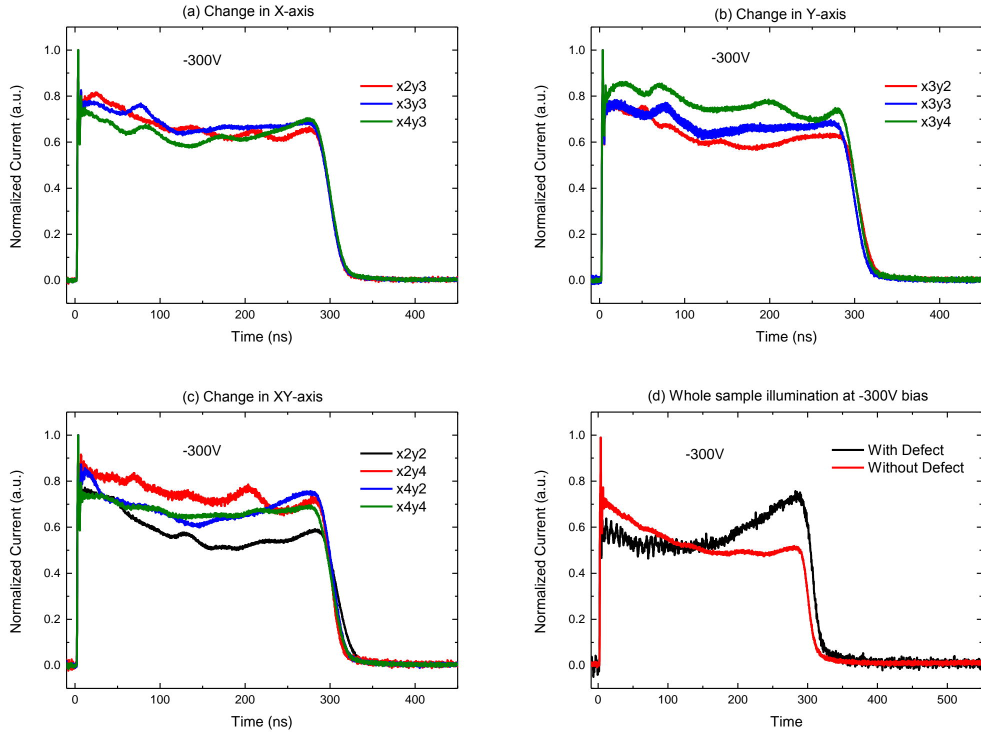

Fig. 6.26 *Transient current waveforms on sample CZT-D3 after grinding the inside defect for (a) different spotting in X-axis, (b) different spotting in Y-axis, (c) for four different spots in XY-axis and (d) for whole sample illumination before and after defect grinding. All measurements were performed at -300V bias.*

It is clearly visible that the CWFs are much straighter when the defect is not presented inside the sample and none of the CWFs display the rise of the current around 200 ns anymore. The interesting thing is, that even though the defect length is visible for ≈ 600 μm on IR microscope, its influence extends much further inside the sample. This statement is substantiated by comparing CWFs at positions x3y2 and x2y2 from Fig. 6.25 (c), (d) and from Fig. 6.26 (b), (c), respectively. Especially the position x2y2 is ≈ 2 mm away from the defect and yet there is still visible distortion of CWF when the defect was presented inside the sample (Fig. 6.25 (d)).

The comparison of mean CWFs at -300 V applied bias before and after grinding (with and without inside defect, respectively) is shown in Fig. 6.26 (d). When the sample was disposed of the defect (red curve in Fig. 6.26 (d)), the CWF has standard exponential decay character which is expected for CZT sample with gold contacts [63]. Also the transit time was 7 ns shorter than in case when the defect was presented inside the sample. That is due to the fact that the mean CWF is the average value of all CWFs which were very similar throughout the sample in this case and

nowhere on the sample was the spot where the CWF had extended transit time like in the initial state.

This chapter shows that very fast L-TCT mapping characterization can provide useful information about homogeneity of the sample and that the significant distortion of CWFs is most probably connected to the inside defects of the sample. Yet the origin of the studied defect is still unknown.

6.4. Charge transport in CdZnTe coplanar grid detectors examined by laser-induced transient currents

In this chapter, laser-induced transient-current-technique was used for the visualization of charge transfer in the CPG CdZnTe radiation detector including distinction to the collecting (CG) and non-collecting grids (NCG). Transient current waveforms measured at different intergrid biasing allowed the identification of principal charge transit features and the final redistribution of collected charge between grids. It is demonstrated that while at the initial period of the charge passing through the detector bulk the current waveform shapes on the CG and NCG electrodes are nearly the same, the intergrid biasing entails significant current deviation at the final part of the transients, where inverted current through the non-collecting grid induces markedly reduced/enhanced collected charge in the NCG/CG electrode. An optimum ratio of cathode/intergrid biasing was found to be close to the ratio of detector width/intergrid dimensions. Also the theoretical simulations demonstrating charge-transfer through CPG are presented.

6.4.1. Experiment and experimental results

In contrast to conventional planar detectors, where the electric field profiles were extensively studied by Pockels effect or transient-current-techniques, analogous investigations on CPG detector are still missing. It is a challenging task to determine CPG detector internal electric field shape precisely due to relatively complicated electrodes structure and application of the bias and intergrid voltage simultaneously. L-TCT is used in this chapter to record a good quality CPG detector current waveforms (CWF) that have very low amplitude by definition. L-TCT enables to characterize the time resolved charge collection process and to evaluate the electric field profile inside the CPG detector under various bias conditions.

Two CPG CdZnTe detectors (labelled as CPG1 and CPG2) with dimensions of $10 \times 10 \times 10$ mm^3 were purchased from Redlen Inc. for the investigation in this chapter. Configuration of the CPG electrodes was designed similar to the anode design in [19] or [21]. Gamma spectroscopic resolution of the detector measured under the bias 1700 V and intergrid voltage 80 V gives the resolution of 2.1 % of the Full Width at Half Maximum at ^{137}Cs (662 keV).

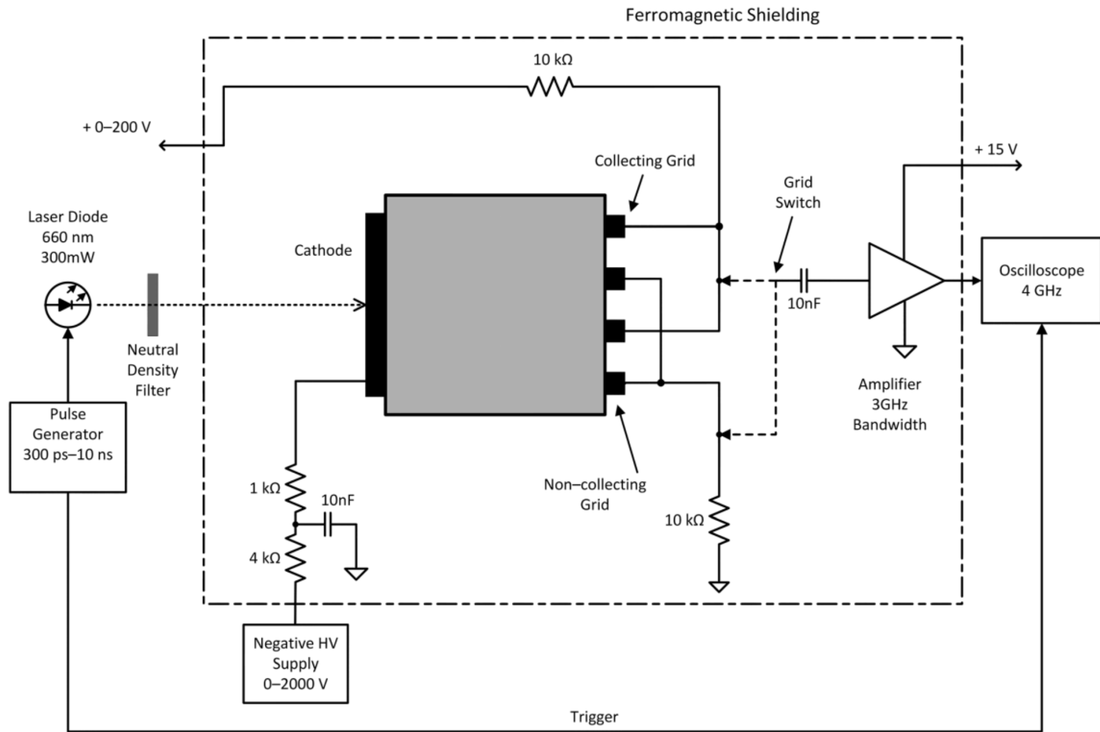

Fig. 6.27 *Block diagram of L–TCT experimental setup for the measurement of CPG detector CWF. Both collecting and non-collecting grid associated CWFs can be recorded by the setup.*

L-TCT setup was modified for measuring the CPG detectors as it is seen in Fig. 6.27. The detector cathode was irradiated by optical pulses (≈ 3 ns as FWHM, 200 ps rise and fall time) using the laser diode (660 nm, 300 mW) that is powered by an ultrafast pulse generator (Picosecond Pulse Labs 10 070A). Pulse output energy was 0.4 nJ and repetition rate was 100 Hz. The wavelength 660 nm was chosen to generate electron-hole pairs locally below the cathode. Collimation and imaging optics and a translation stage is used in the setup to adjust the laser diode beam onto the examined spot of ≈ 3 mm^2 in the centre of cathode. A neutral density disc filter is placed in the beam line for optimal intensity attenuation of the laser pulse. L–TCT detection electronics is again based on the direct high frequency voltage amplification of CWF flowing on the AC coupled detector anode. Negative bias V_B is applied to the CPG detector cathode (up to 1700 V) and supplementary intergrid voltage V_{IG} between the collecting and noncollecting anode grid is introduced by an additional adjustable low noise voltage supply (0 – 200 V). CWF shape is recorded using an ultrafast digital sampling oscilloscope. Both collecting and noncollecting grid associated CWFs can

be recorded in the setup independently by the respective anode grid switching to the input coupling capacitor of the amplifier. Also the deconvolution procedure that removes influencing by the electronic setup transfer function is routinely applied to obtain original measured CWF shapes (see chapter 6.2.1.).

The dependence of electron CWFs on various cathode biases (from 1000V to 1700 V) and intergrid voltage set to 50V for collecting and noncollecting anode grid of CPG1 CdZnTe detector are presented in Fig. 6.28 and Fig. 6.29, respectively.

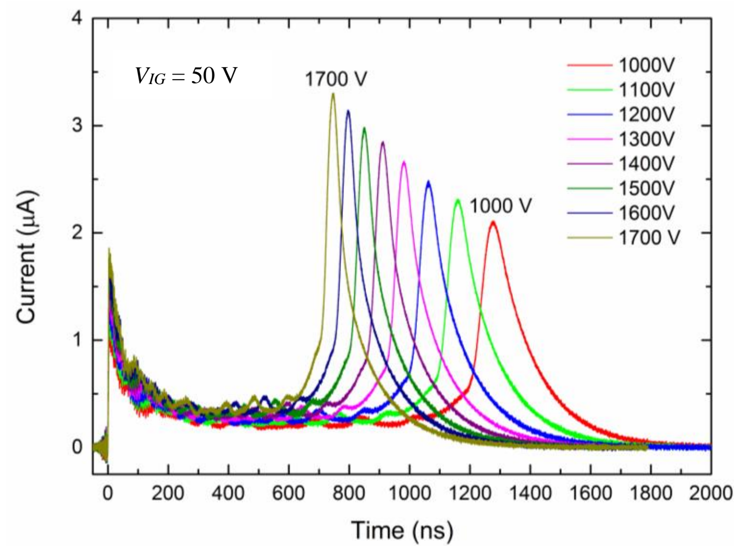

Fig. 6.28 *The bias dependence of L–TCT electron CWFs of CPG1 detector measured on the collecting anode grid for intergrid voltage of 50 V.*

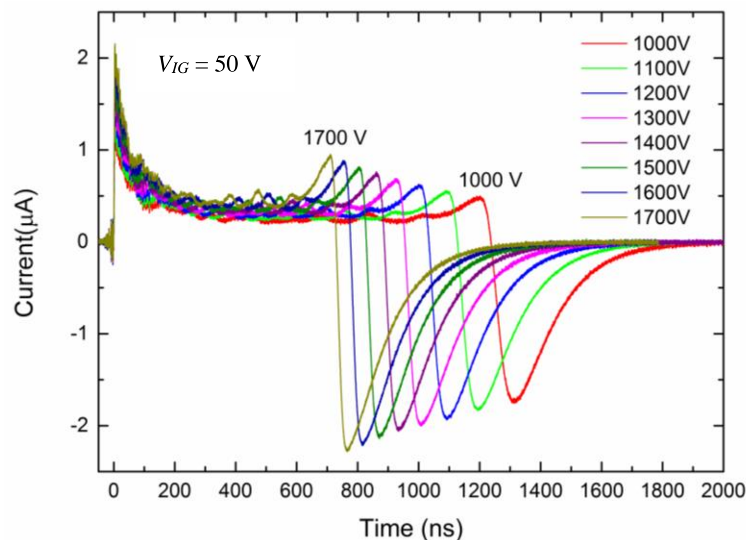

Fig. 6.29 *The bias dependence of L–TCT electron CWF of CPG1 detector measured on the noncollecting anode grid for intergrid voltage of 50 V.*

CWFs measured on both grids show an initial distinct peak on the leading edge resulting from the contact influence on the detector internal electric field profile and variable dominant tail peaks representing the electric field forcing the electron drift from NCG to CG near the anode. The amplitude and FWHM of the tail peak is strongly dependent on the detector bias V_B. The dependence of electron collecting grid CWFs biased by 1700V with various intergrid voltages is shown in Fig. 6.30 and intergrid voltage dependence of the overall collected charge calculated by the integration of CFWs and the detector resolution for ^{137}Cs (662 keV) peak are presented in the inset of Fig. 6.30. It is clearly visible that the optimal V_{IG} sufficient for nearly total charge collection on CG grid reaches about 80V which corresponds to the best detector resolution. While for lower V_{IG} the collected charge is markedly lower, for higher V_{IG} it is practically independent of V_{IG}. Simultaneously, at the higher intergrid voltage the overall electronic noise of the detector increases due to higher leakage current resulting in worsened spectroscopic performance. Based on all the obtained experimental data it is suggested an optimum intergrid voltage V_{IG} expressed by the formula

$$V_{IG} \cong V_B \frac{D_g}{L} \tag{6.13}$$

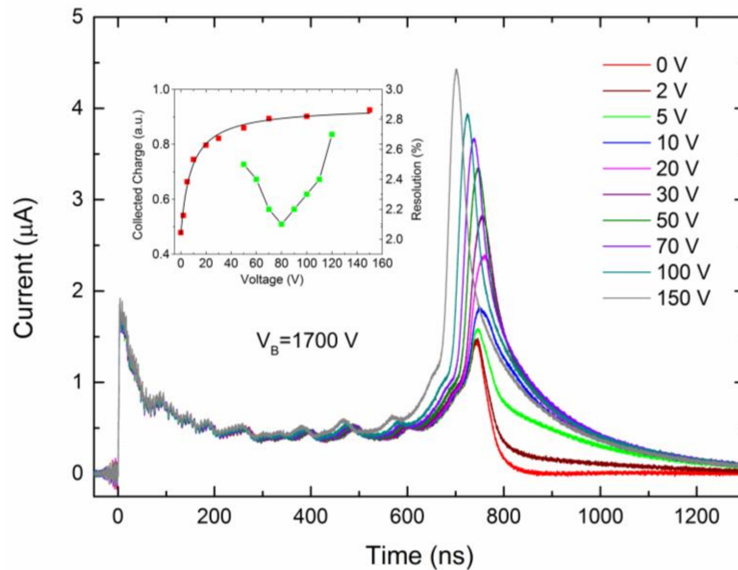

Fig. 6.30 Intergrid voltage dependence of L–TCT electron CWFs of CPG1 detector measured on the collecting anode grid for bias 1700 V. The dependence of integrated CWFs collected charge (red squares) and the detector resolution (green squares) on the intergrid voltage is given in the inset with a guide for eye fit (black line).

where V_B is the detector bias, L is the detector width, and D_g is the distance between the adjacent grid centres. In measured detector with L = 10 mm and D_g = 0.5 mm the optimum V_{IG} results ≈ 0.05 V_B. For the case with V_B = 1700 V shown in Fig. 6.30 the optimum V_{IG} ≈ 85 V is evident. In addition we may conclude that based on Eq. (6.13) the increasing of single V_B or V_{IG} without complementary increasing of V_{IG} or V_B, respectively, does not improve the detector performance.

6.4.2. Theoretical methods and TCT simulations

The L-TCT response has been modelled by drift transport mechanism of photo-generated carriers. The above band gap photo-generation is assumed. Because in L-TCT, holes are swept to cathode in subnanosecond times, hence, their influence is negligible, the electrons only [109] and collection times much shorter than electron lifetime are assumed. The current response caused by moving charge between electrodes have been calculated using Shockley-Ramo theorem. The foundation of Shockley-Ramo theorem is based on known electrostatic potential in two cases. The first one consists of real electrostatic potential distribution within a detector. The second is a potential distribution of a weighting potential. In the second case, the electrode of interest is biased to 1 V and all other electrodes are at 0 V. The corresponding electric field determines the charge response on a given electrode and the time derivative determines the current response [110]–[113]. The full real potential and corresponding electric field determines the trajectory of photo-generated carriers. It is assumed only small enough concentration of photo-generated carriers that they do not spread by diffusion or electrostatic repulsion on the length scale of detector size before they are all swept by anode. This is clearly well fulfilled since the diffusion time broadening is about 10 ns and carriers move about 800 ns from cathode to anode. The limitations of this assumption are discussed later.

Theoretical simulations of the detector internal electric field profile were performed by solving Poisson's equation

$$-\Delta\varphi = \frac{\rho_S}{\epsilon}, \tag{6.14}$$

by finite element method. Mostly neutral detector bulk characterized by ρ_s = 0 is used with an exception of weak space charge near the cathode with the positive space charge

concentration $N_D = 4 \times 10^{10}$ cm^{-3} to get enhanced current observed shortly after the pulse excitation. The small current enhancement at the time of charge collection has been modelled by a weak negative space charge near the anode ($N_A = 5 \times 10^{10}$ cm^{-3}). The V_B then preferentially drops within the space charge region between the cathode and anode. The detector geometry has been chosen to properly model a Redlen Inc. state-of-the-art CdZnTe CPG detector. The mesh triangulation has been used to properly describe size effects of rectangular metal anode grid. The anode behaves as a set of parallel charged wires when charge is far from the anode compared to anode characteristic size (anode strip width). And, the anode behaves like infinitely large planar electrode if the charge is close enough to anode compared to characteristic anode size. The latter case as a measure of sufficiently dense triangulation is considered. This regime can be analytically treated as well, and pronounces itself as a constant electric field and linear-in-distance electrostatic potential.

The electron trajectories are calculated for 300 starting equidistant positions at the partially transparent cathode. Each trajectory is traced according to the local electric field and the overall measured current response is obtained by the sum of all 300 current responses. The motion of each electron (electron packet) has been calculated by integrating their drift velocity. The starting positions are located in a 1.4 mm wide laser spot at the cathode centre to simulate photon absorption by focused laser beam. The strong local electric field in the vicinity of electrodes causes velocity saturation. The local electric field reaches maximal values $\approx 10^4$ V/cm, electron mobility is $\mu \approx 1000$ cm^2 V^{-1} s^{-1}, giving rise to speeds up to 1×10^7 cm/s. The saturation velocity in CdZnTe is $v_{sat} \approx 1.5 \times 10^7$ cm/s [38] hence it is expected the velocity-field dependence to exhibit non-linear behaviour. The velocity saturation [13] is taken into account by

$$v = \frac{\mu E_{loc}}{\sqrt{1 + \left(\frac{\mu E_{loc}}{v_{sat}}\right)^2}}. \tag{6.15}$$

The carrier diffusion has been taken into account by convolution of bare drift current response with Gaussian distribution of time varying width. The temporal broadening δt can be estimated from

$$\delta t = \frac{\sqrt{2D_e t_r}}{v} \tag{6.16}$$

where

$$D_e = \mu_e \frac{k_b T}{e} \tag{6.17}$$

is electron diffusion constant related to electron mobility μ_e, temperature T and mean drift velocity v, which can be estimated from the transient time t_r and detector width L; $v = L/t_r$. The temporal spread of the current packet is considered to be $\delta t = 0$ ns at t = 0 ns and it has been estimated to be $\delta t = 10$ ns at the time of charge collection on anode (t ≈ 800 ns). The spatial potential distribution is shown in Fig. 6.31(a) and in Fig. 6.31(b). The electric field profiles along three selected electron trajectories are depicted in Fig. 6.31(c) and Fig. 6.31(d). This model shows that the electric field near the anode strongly depends on a position inside the detector. It may be observed that the electron trajectories can be split into three groups, inset in Fig. 6.31(a) and corresponding potential profiles are shown in the inset of Fig. 6.31(b).

The first group of electrons moves directly to the collecting grid, the trajectory of the second group moves towards the noncollecting grid and bends to the collecting grid. The third group of electrons reaches the noncollecting grid. The electrons directly moving towards collecting grid have the shortest trajectory, the electrons dragged from their initial motion from noncollecting to the collecting grid have the longest trajectory and the electrons swept by NCG move in the lowest mean electric field. This spatial distribution is reflected in the spread of CWFs. The results of L-TCT numerical modelling are shown for five values of V_{IG} = 0 V, 10 V, 30 V, 70 V, and 150 V in Fig. 6.32(a) and Fig. 6.32(c) and for four values of V_B = 1000 V, 1200 V, 1400 V, and 1700 V in Fig. 6.32(b) and Fig. 6.32(d). The current calculated between cathode and (a), (b) collecting anode grid is compared with signal on (c), (d) noncollecting grid.

The proposed theoretical model (Fig. 6.32) describes well all major trends in the experimental data (Fig. 6.28, Fig. 6.29 and Fig. 6.30). The measured CWFs are in good agreement with the model, even though that non detector surface effects are included. Hence, it can be assumed that the surface effects are negligible and basic CWFs can be explained solely by currents induced by moving charge in the bulk of the detector. The electrons moving by constant speed towards/from given electrode cause positive/negative current. The accelerating/decelerating electrons cause increasing/decreasing current magnitude.

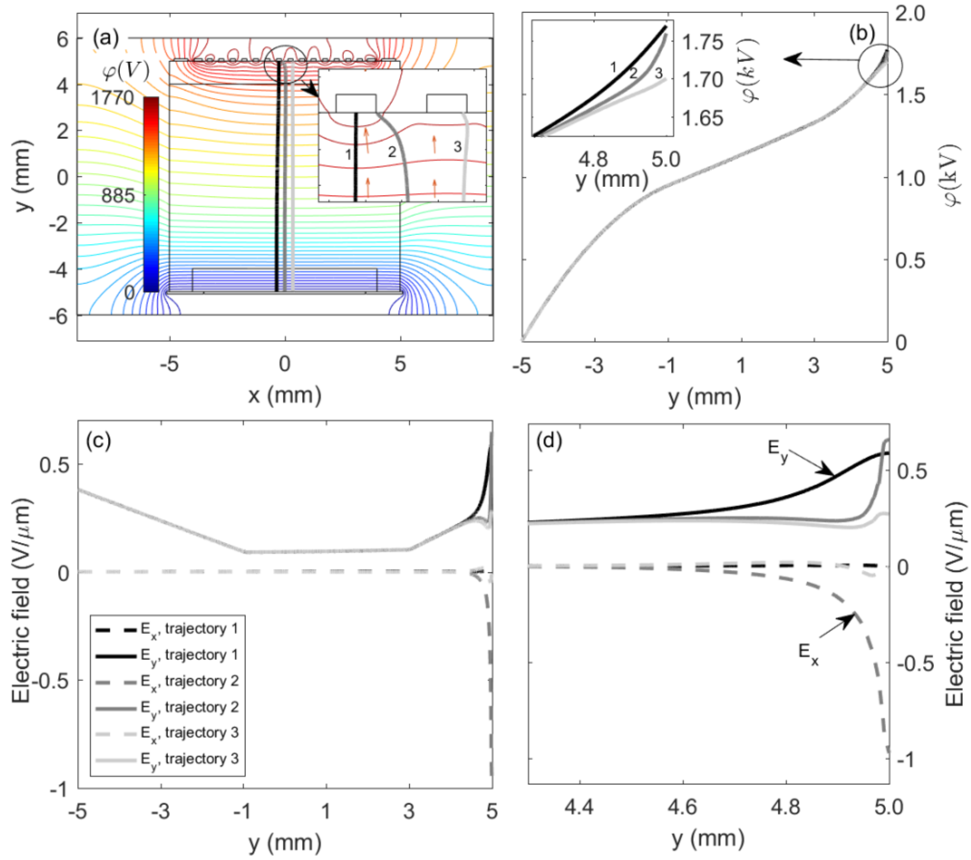

Fig. 6.31 *(a) Spatial distribution of equipotential lines inside the detector area and in its close surroundings. The detector area is depicted by thin solid black lines. The three selected electron trajectories are shown by thick black and dark and light grey solid lines and labelled 1, 2, and 3, respectively. The trajectories start at the cathode (bottom part of the detector) and end at the anode (top part of the detector). The inset in (a) shows all three trajectories in the close vicinity of the anode (left contact is CG and right contact is NCG). Four vectors of E_{loc} are also shown by red arrows in the inset. (b) Electrostatic potential $\varphi(x,y)$ profile along the electrons trajectories. Inset in (b); detail of $\varphi(x,y)$ in the anode vicinity. The local electric field along electrons trajectories is shown in (c) and (d). Figure (c) is the overall field profile. The field profile in the anode vicinity is shown in (d). The solid and dashed curves belong to E_x and E_y electric field components, respectively.*

The current decrease at $t = 0$ ns is due to the decelerating electrons in the positive space charge around the cathode. Similarly, the current increase at the time of charge collection ($t \approx 0.7$ ns in Fig. 6.32(a)) for $V_{IG} = 0$ V is due to the accelerating electrons in negative space charge around the anode (see the next subchapter). This effect is pronounced for non-zero V_{IG} as a collection current peak shoulder.

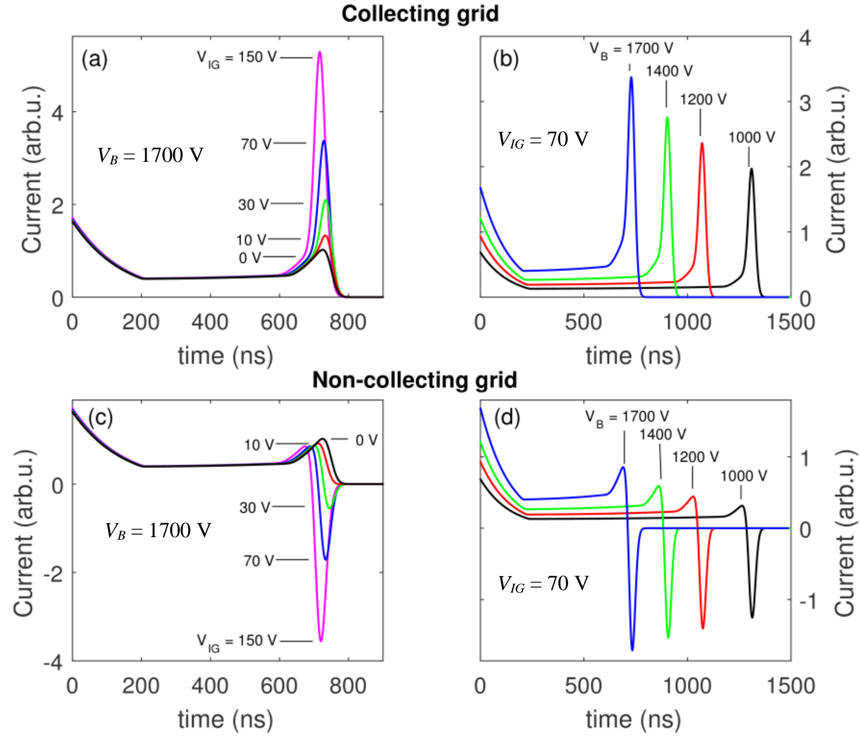

Fig. 6.32 *The calculated L-TCT curves for (a), (b) CG and (c), (d) NCG. The (a), (c) V_{IG} dependence is calculated for V_B = 1700 V and (b), (d) V_B dependence is calculated for V_{IG} = 70 V.*

The slight current increase at intermediate times is due to the spatial non-homogeneity of electric field inside the detector. The rising NCG current at, e.g., $t \approx 0.7$ ns for $V_B = 1700$ V (Fig. 6.32(c)) is caused by accelerated electrons in negative space charge at the NCG anode. The sudden current reversal is a consequence of electrons retraction from NCG as they are swept towards CG by its higher electrostatic potential. The intergrid bias V_{IG} influences electrostatic potential distribution mainly in a small area at anode. Hence, it affects the collection current peak only. The effect of V_{IG} can be seen in Fig. 6.30 and Figs. Fig. 6.32(a), Fig. 6.32(c). The collection current peak rises with increasing V_{IG} and the peak position shifts towards shorter collection times, both being consequence of higher mean field at the anode. The small shift of the collection current peak at $V_{IG} \approx 30$ V towards longer collection time is caused by diffusion. In contrast to V_{IG}, the cathode potential V_B determines mean field throughout the detector. Hence it affects, beside the transient time, also the width of the depletion width at the cathode and, as a consequence, the local electric field together with measured current. It also has to be pointed out that the L-TCT curve

simulation, as proposed here, can be used as another method to retrieve electric field profile throughout the detector [79], [114], [115].

6.4.3. Doping, depletion width and diffusion

The effect of CPG detector doping was also theoretically simulated as it is shown in Fig. 6.33 for positive space charge $N_D = 0.7 \times 10^{10}$ cm^{-3}, 4.0×10^{10} cm^{-3} and 16×10^{10} cm^{-3}. The current response in L-TCT is modelled for collecting grid (CG) in Fig. 6.33 (a,b,e,f) and for non-collecting grid (NCG) in Fig. 6.33 (c,d). The current response can be split into three characteristic intervals. The first one is given by charge

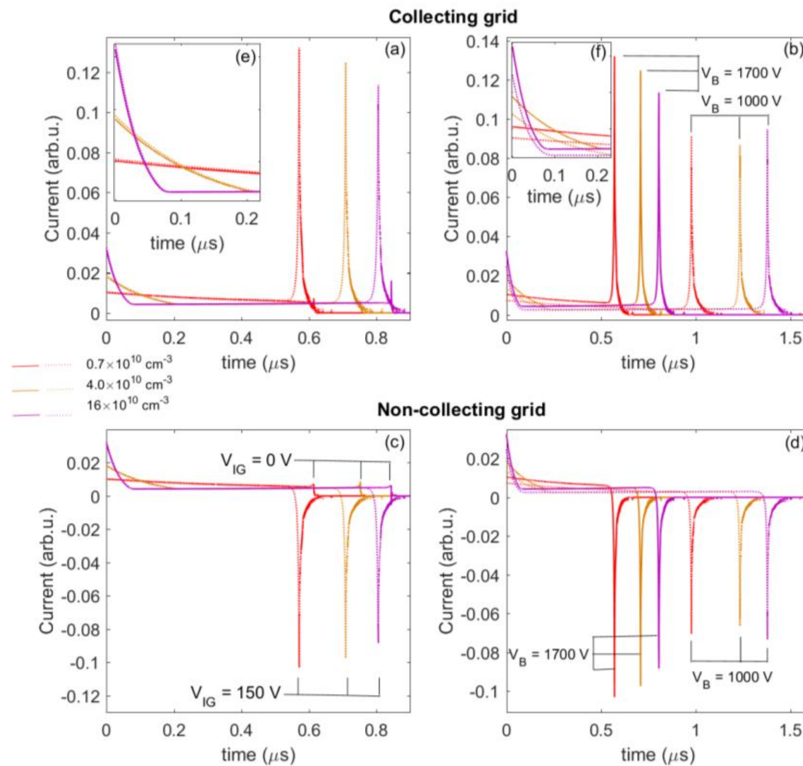

Fig. 6.33 *Doping dependence of L-TCT response curves. Doping densities $N_D = 0.7 \times 10^{10}$ cm^{-3}, 4.0×10^{10} cm^{-3}and 16.0×10^{10} cm^{-3} are distinguished by red, orange and violet color. Solid (dashed) curves in (a,c,e) show numerical simulation for intergrid bias $V_{IG} = 0$ V (150 V). Solid (dashed) curves in (b,d,f) show numerical simulation for negative cathode bias $V_B = 1700$ V (1000 V). The insets (e,f) depict detail of the current response around $t \approx 0$ µs. The space charge width below cathode is 0.64 DW. The simulation is shown for (a,b,e,f) collecting grid and (c,d) non-collecting grid. The I_G trend (a,c,e) is studied for negative V_B=1700 V and the V_B trend (b,d,f) is studied for V_{IG}=150 V.*

deceleration in a positive space charge below cathode. The second regime is at intermediate times when the charge moves through the part of the detector without any fixed space charge. The third regime is a time of charge collection at the anode. It can be seen from numerical simulation that the peak current response at the collection time increases with decreasing doping. The initial current peak is decreasing with decreasing doping and ideally disappears. The initial current peak can give rise to a spurious signal contributing to a low energy spectral shoulder in γ-ray spectra. The anode intergrid bias is shown for two values 0 V and 150 V in Fig. 6.33 (a) and (c). The intergrid bias does not influence the initial current response, as is shown in the inset Fig. 6.33 (e), in contrast to cathode bias, inset (f). This is caused by the local effects of intergrid bias on a small area around anode. The cathode bias VB (cathode to NCG bias) influences mean field within a detector, thus changing current response for all times from the photo-carrier generation to their complete collection on CG.

The cathode depletion width dependence of the L -TCT waveform is shown in Fig. 6.34. The cathode is a planar electrode and the constant current is expected for uncharged bulk semiconductor. The space charge (fixed or mobile) causes deceleration of carriers, hence decreasing current. The equilibrium depletion width (DW) is given by [13]

$$DW = \sqrt{\frac{2\epsilon V}{qN_D}}, \tag{6.18}$$

where N_D is doping density (or fixed space charge), V is a voltage drop within a depletion width and ϵ is permittivity. The width of the depletion region varies from this simple model when carrier trapping and de-trapping is assumed, or more than one trapping level is located in the vicinity of the Fermi level. It can be seen from Fig. 6.34 that the peak current increases with decreasing depletion width. This effect is due to the reduced total voltage drop in a depletion region and consequently higher voltage drop at the anode. The latter causing higher electric field and higher current. It has to be note here that this is in contrast to doping density. The current response of a NCG is shown in Fig. 6.34 (b). The current response is, similarly to CG, stronger for thinner depletion width.

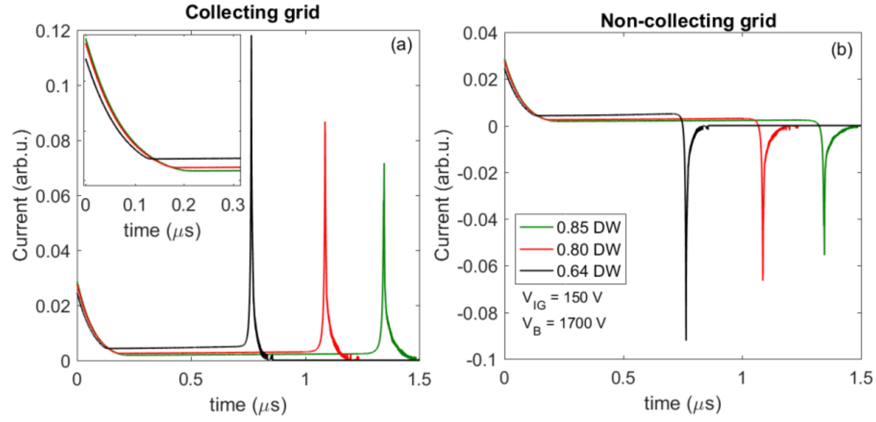

Fig. 6.34 *Space charge width dependence of L-TCT response curves. The space charge width is measured in units of equilibrium depletion width DW for $N_D = 8 \times 10^{10}$ cm^{-3}. The black, red and green curves correspond to depletion width 0.64, 0.80 and 0.85 DW, respectively. The numerical simulation is shown for (a) collecting and (b) non-collecting grid. The inset in (a) depicts detail of current evolution at $t \approx 0$ μs. The intergrid bias $V_{IG} = 150$ V and cathode bias negative $V_B = 1700$ V.*

The effect of diffusion is shown in Fig. 6.35. Diffusion takes important role for long enough transient times t_r when δt is comparable or larger than drift current temporal width. For this reason it is shown only the current peak modification at the charge collection on anode. The temporal broadening δt be estimated by eq. (6.16). The current response for CG and NCG is shown for four diffusion broadening times (0, 10, 20, 30 ns). The current response is calculated for $N_D = 4 \times 10^{10}$ cm^{-3} and space charge width 0.64 of the equilibrium depletion width.

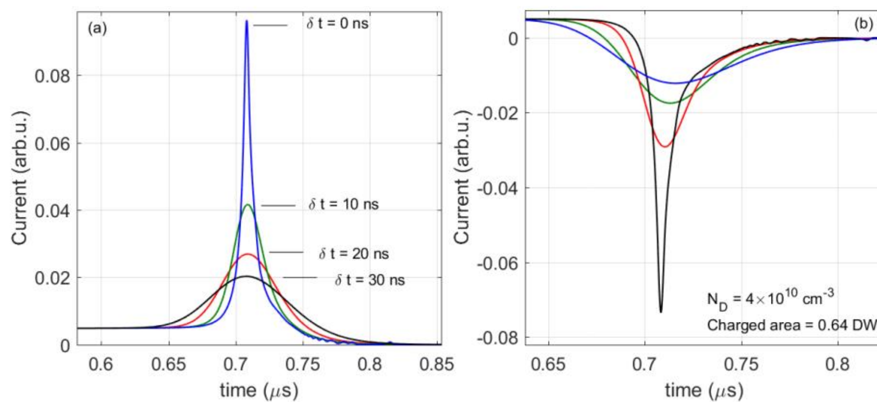

Fig. 6.35 *The effect of diffusion on L-TCT current response; positive space charge below cathode only (0.64 DW, $N_D = 4 \times 10^{10}$ cm^{-3}). Diffusion peak broadening $\delta t = 0$, 10, 20 and 30 ns has been assumed. The effect of diffusion is simulated for (a) collecting and (b) non-collecting grid. The intergrid bias $V_{IG} = 150$ V and cathode bias $V_B = 1700$ V.*

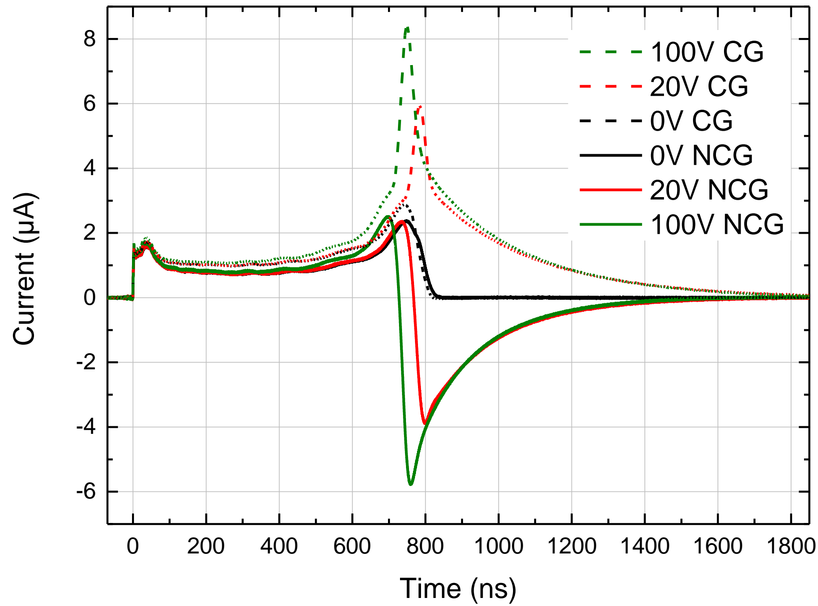

Fig. 6.36 *Experimental data of L-TCT in CPG2 sample measured on a collecting grid (solid curves) and non-collecting grid (dashed curves) for negative V_B = 1500 V and three intergrid biases V_{IG} = 0 V, 20 V, 100 V.*

The measured L-TCT waveforms in a CPG2 detector on a CG and NCG anode are shown in Fig. 6.36. The data show good qualitative agreement and in many aspects also quantitative comparison with simulated data can be made, especially concerning relative intensities of current peaks at the beginning and at the end of charge collection. The initially decreasing current is caused by decelerating electrons in a positive space charge below the cathode. The second collection current peak is stronger than the first one especially due to the strong electric field between CG and NCG. This current originates also in a negative space charge below anode. The current peak at the time of charge collection $t_r \cong 700 - 800$ ns is broadened by electron diffusion. The amount of broadening estimated from the numerical simulation is $\delta t \approx 10$ ns.

6.4.4. Differential current sensing

In this part, the importance of the measurement technique to detect photogenerated carriers is presented. An example of three current waveforms detected on CG, NCG and differentially measured signal between CG and NCG is shown in Fig. 6.37. The advantage of differential sensing is lack of any signal before charge reaches coplanar grid anode. There is no influence of the positive space charge at ca-

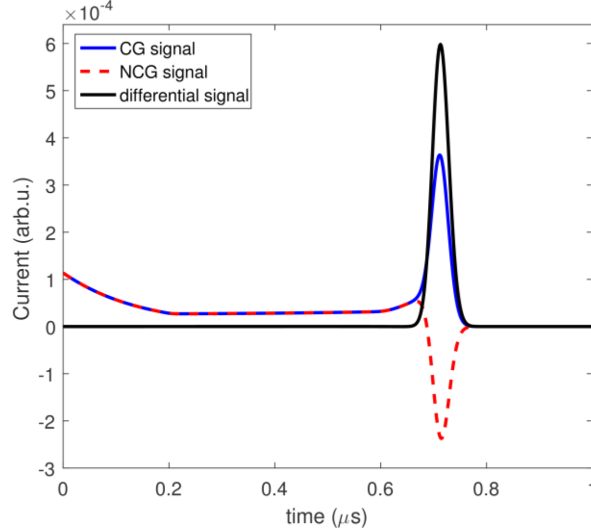

Fig. 6.37 *L-TCT current response for voltage drop $V = \frac{1}{3}V_B$ at the cathode (positive space charge $N_D = 4 \times 10^{10}$ cm^{-3}) and voltage drop $V = \frac{1}{10}V_B$ at the anode (negative space charge $N_A = 5 \times 10^{10}$ cm^{-3}). The current response measured at the collecting grid (solid blue curve), non-collecting grid (dashed red curve) and differential signal (solid black curve). The applied biases are V_{IG} = 150 V and negative V_B = 1700 V.*

thode, since such a current response is equal for CG and NCG. The differential sensing does not bring significant improvement for L-TCT, where the differential current waveform can be formed by data post-processing, as has been done in numerical simulation in Fig. 6.37 to illustrate the method. The advantage is more pronounced when γ-ray photons are detected. Here, the absorption events occur randomly within a detector volume and they contribute to signal broadening.

X-ray/gamma-ray experiment has been modelled by solution of Poisson equation (eq. (6.14)) and, in the second computation step, electron trajectories have been obtained by integrating their velocities (as in L-TCT curves). The initial position of photo-generated carriers have been determined in a Monte-Carlo loop. Random position of photo-generated carriers is a model of large absorption length of X/gamma-ray radiation, hence the model holds for more than 100's eV energetic photons. Here, all trajectories have not been summed with a random initial position. Instead, the current response has been calculated for each trajectory separately and the total collected charge has been calculated by integrating current response in time. The electron current response has been considered only since holes mobility is ten times

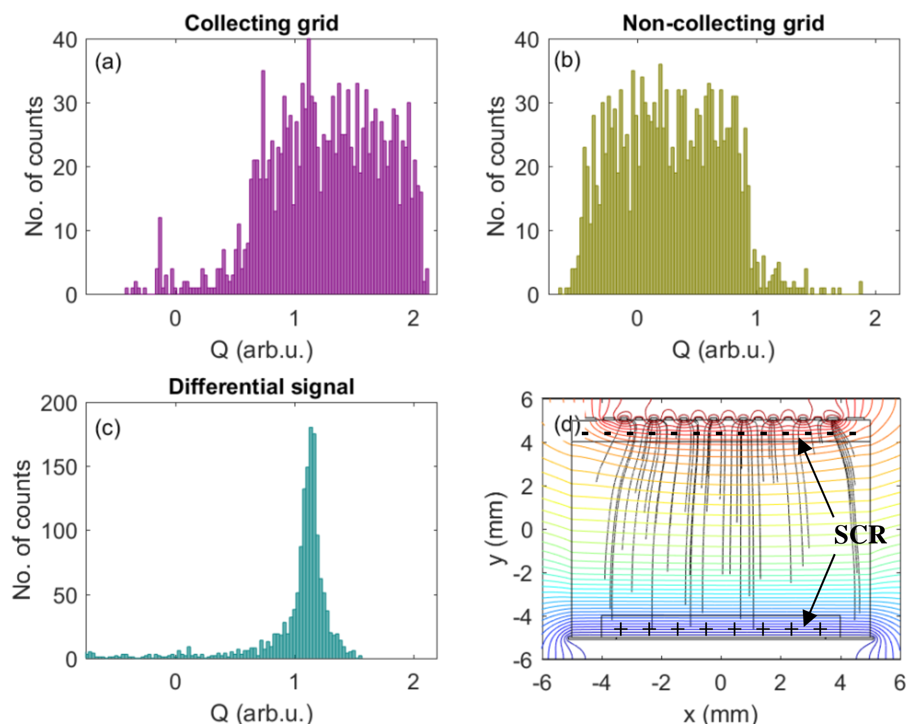

Fig. 6.38 *Monte-Carlo simulation of 1500 single γ-ray photon absorption events. The absorption probability is assumed to be equal throughout the detector volume. Currents induced by holes are neglected. The histograms (a,b,c) depict statistics of collected charge for all absorption events. The statistics is shown for the case of current measured on (a) collecting, (b) non-collecting grid and (c) differential signal between collecting and non-collecting grid. Equipotential lines (blue to red contour lines), detector area (solid black lines) and 50 selected random absorption events are shown in (d). Arrows are pointing to the positive and negative space charge regions (SCR), respectively.*

lower [34] and holes have higher trapping cross-section. The γ-ray photon detection is modelled in Fig. 6.38. 1500 trajectories of randomly generated photo-excited electrons have been traced and the total electron-induced charge has been calculated. An example of 50 random trajectories is shown in Fig. 6.38 (d). Let's note, that if holes are considered the total collected charge is $1e$, however, low hole mobility and high trapping cross-section for holes is assumed. This leads to much weaker current response, or, the current response on very long time scales in comparison to electron induced TCT waveforms. For this reason, electron traced from below cathode gives larger induced charge than electrons traced from the anode vicinity. The statistics of all Monte-Carlo simulated absorption events are shown in Fig. 6.38 (a,b,c) for CG, NCG and for differential sensing, respectively. The CG and NCG current waveforms

have rectangular like shape caused by equal distribution of absorption events within a detector. The mean collected charge on NCG is shifted towards zero because ideally no charge is collected by NCG. Negative space charge at the anode is considered here. This space charge screens the electric field of neutral bulk detector (no charge collected by NCG) and it allows certain electron trajectories to be collected by NCG. In contrast to CG current response, the differential sensing, see Fig. 6.38 (c) shows the same mean charge collection, however, the Full Width at Half Maximum is ten times smaller. This is caused by the signal insensitivity to the position of random-in-nature absorption events of γ-ray photons. Let's also note that there is no spurious signal at 0 ns, Fig. 6.37, caused by positive space charge, hence reduced low energy spectral shoulder [37] is expected beside the Compton scattering contribution. The effect of holes is also reduced regardless of assumptions made in this simulations. Holes are attracted towards cathode giving even weaker response on a CG anode.

6.4.5. Discussion of obtained results

General considerations to understand current waveforms follow from Shochley-Ramo theorem $i = eE_v v$. Decreasing/increasing current points on decreasing/increasing electric field in a positive/negative space charge at cathode/anode. The space charge at anode forms weak current response at $V_{IG} = 0$ V and it causes current shoulder for early time of charge collection. The dominant signal at the charge collection time for $V_{IG} > 0$ is caused by accelerated electrons in a spatially modulated electric field by intergrid bias V_{IG}. More specifically, it has been shown that the cathode bias increases the peak current response. It also increases the initial signal caused by positive space charge at the cathode – Fig. 6.33 (b). This can lead to spurious signal leading to low energy spectral shoulder in X-ray spectra. At the same time, since the charge is swept faster through detector bulk, there is lower probability for carrier trapping and detector polarization. The lowest doping density is still the ultimate option here because it worsens the charge collection efficiency. The effect of diffusion is twofold. First, the higher is diffusion/mobility, the faster is a response time at a given detector size. Second, as absorption efficiency increases with detector size, diffusion lowers the signal. Hence, for fast response and strong current signal, thinner detector is acceptable. Let's also point out that thinner detector volume also eliminates carrier trapping. The optimal detector thickness and coplanar grid dimensions can be

established for differential signal sensing. The final peak width in the case of differential sensing is caused by space charge at the anode, grid size (signal increases for denser anode grid) and by carrier diffusion. Low diffusion rate also leads to better signal-to-noise ratio. The diffusion length on a distance of detector size should be smaller than anode intergrid spacing. If diffusion length is comparable or larger than the anode intergrid spacing, the CG and NCG diffusion dominated current will be equal, and, differential signal will be negligible.

The proposed numerical model shows that many current waveform characteristics can be explained separately one by one using simple physical considerations. These are based on electrostatic potential spatial distribution of the space charge in bulk semiconductor and assuming proper scaling of charge-to-electrode distance. If charge is close to planar cathode with respect to the cathode dimension, the electric field can be considered constant and electrostatic potential linearly scales with distance from cathode. In the presence of space charge below cathode and charge-cathode proximity, the field scales linearly and electrostatic potential quadratically with the charge-cathode distance. The Schockley-Ramo theorem then gives quadratic current waveform. The situation at the anode has to be split into two regimes. When electron is far from anode compared to the anode dimension, the electric field can be thought as that of charged wire. The intergrid potential difference will be negligible and the electron effectively moves in the effective electric field given by mean potential on CG and NCG anode. This mean potential influences the transient time by the order of 100 D/L %, where D is anode width and L is a detector width. When electron approaches anode on a distance much smaller than anode width, the situation becomes equal to the one at cathode in close charge-cathode proximity. The iterative schemes can be applied to describe analytically field profiles through whole detector volume. Deviations from these assumptions lead to another model parameters. It has been studied negative space charge below anode as an example and discussed diffusion due to localized carriers in one narrow potential minimum. This additional parameter is easily taken into account in this drift model.

7. Conclusion

The thesis is focused on the study of detectors performance based on semiconductors CdTe and CdZnTe which have been examined at IoP CU for several years. This challenging task was supported by standard experiments used in laboratories of IoP CU, and also by new experimental techniques which were developed in this laboratories: the laser-induced transient-current-technique (L-TCT) and spectral measurement of pixelated detectors under the high flux of X-rays. High improvements of existing experimental setup in the case of TCT and development of a new setup in the case of spectral measurement under high X-ray fluxes, were supplied by the simultaneous development of methods for processing of measured data. This labour resulted in publication of several papers [45], [53], [102], [116]–[119] and provided data for this work where the most interesting results are reported and summarized. The thesis itself is divided into three parts.

The first part deals with surface treatments on CdTe and CZT material prior to metal contact preparation and with the influence of these various treatments on detector performance (i.e. leakage current and spectral resolution), especially the long-term time stability of such prepared detectors. The best treatments – chemo-mechanical polishing with additional chemical etching and consequent passivation in 50% potassium hydroxide (**BEBM+KOH**) or in NH_4F/H_2O_2 aqueous solution (**BEBM+NHF**) were proposed. These treatments have shown a high leakage current reduction leading to high energy resolution of detectors and moreover, they are stable in time. This was investigated for 21 days and one year, respectively. The results were published in [116].

The second part is study of pixelated CZT detector under the high flux of X-rays. In this case, the enormous generation of electron-hole pairs leads to the capturing of generated holes at the deep level inside band gap which creates space charge inside the sample. This space charge then shields an applied electric field, thus, the detector has lower charge collection and becomes polarized. The polarized detector then needs time without biasing to restore to the base state. The main effort of this part of the thesis was depolarization of such detectors during the X-ray irradiation. This can be done by infrared (IR) illumination of the sample at a specific wavelength/energy (1200 nm in this case). By adding this additional illumination, it is possible to generate electrons from valence band to the deep level where recombination with the trapped

holes occurs and the value of the space charge drops. This can has a huge application potential in X-ray medical imaging. Although only the first results are presented in this work, this study is still ongoing. Currently, the experiments with higher intensities of additional IR illumination are studied. Higher intensities should allowed depolarizing of the detector into the higher X-ray fluxes. Results of this work were published in [53].

The last part of thesis is about development of L-TCT as a powerful experimental technique for characterization of semiconductor detectors. The existing apparatus at IoP CU was extended by nanoseconds laser pulse generators with wavelengths from visible to IR spectral region; high frequency electronics with lower noise; XYZ translation stages; faster monitoring oscilloscope LeCroy – 4 GHz and others.

With this modifications it was possible to study the transport properties of planar and coplanar detectors. At the first part of this chapter, the transport properties of (CdZn)Te detectors were characterized using TCT and TChT output signal generated by alpha–particles. It was found that the calculated electron mobility using TCT method is practically independent of the applied detector bias and is close to the previously published results. On the other hand, it is quite difficult to use α-TCT method for mobility evaluation at low bias due to a very weak transient current signal with strong high frequency noise. Therefore the experimental setup was extended by laser source for generating electron-hole pairs (L-TCT) which is the subject of the second part of this chapter.

L–TCT current waveforms were recorded in a wide bias range 50 V – 700 V and the evidence of the detector parasitic induction component in the current waveform shape has been identified and discussed. Original CWFs were retrieved by a deconvolution with the transfer function of the electronic setup and the restored CWFs revealed less declining slope with no negative overshooting compared to the measured data. Calculating collected charge from the deconvoluted CWFs allowed us a more precise determination of the charge collection efficiency and electron mobility–lifetime product. It is argued that deconvolution of measured CWFs makes possible to determine the mobility–lifetime product with much better precision compared to the previous approach.

Another part of this chapter deals with the inhomogeneity presented inside the detector sample and its influence on the measured L-TCT CWFs at the different spots

on the sample as well as on the mean CWF of the sample. The mapping of CWFs and infrared microscopy provided the proof of unspecified defect occurring inside the sample and affecting the profile of CWFs, which indicates distortion of internal electric field, and the transit time of collected charge carriers.

At the last part of this chapter, the L–TCT response of co-planar detector has been studied experimentally and the results have been compared with the theoretical model. The optimal ratio of intergrid and cathode bias has been proposed based on spatial distribution of the electric field within the detector. This approach enables to find optimal working conditions of CPG detector to reach the best energy resolution. The theoretical model of fixed space charge below cathode and anode has been used to describe all major trends in L–TCT data. The numerical model shows that the electric field in the electrodes' vicinity is strong enough to cause velocity saturation and current peak broadening shows, beside sample inhomogeneity, an important role of carrier diffusion. Finally, modelling the L–TCT curves can be used as a method to probe internal electric field inside the radiation detectors.

Although quite a few applications of the L-TCT were demonstrated and studied in this thesis, another ones, including investigations of the electric field at various temperatures, various types of excitation (above bandgap laser illumination) or application on another materials (ZnO, Perovskite, SiC,…) are currently being studied or are about to be investigated soon at IoP CU.

Bibliography

[1] D. de Nobel, *Philips Res. Reps.*, vol. 14, no. 361, 1959.

[2] C. Szeles, S. A. Soldner, S. Vydrin, J. Graves, and D. S. Bale, “CdZnTe semiconductor detectors for spectroscopic X-ray imaging,” *IEEE Trans. Nucl. Sci.*, vol. 55, pp. 572–582, 2008.

[3] R. Matz, T. E. Schlesinger, J. C. Lund, and M. Schieber, “CdZnTe spectrometers for gamma and X-ray applications,” *Semicond. Room Temp. Nucl. Detect. Appl.*, vol. 43, pp. 335–335, 1995.

[4] S. Del Sordo, L. Abbene, E. Caroli, A. M. Mancini, A. Zappettini, and P. Ubertini, “Progress in the Development of CdTe and CdZnTe Semiconductor Radiation Detectors for Astrophysical and Medical Applications,” *Sensors*, vol. 9, pp. 3491–3526, 2009.

[5] N. Gehrels G. Chincarini, P. Giommi, K. O. Mason, J. A. Nousek, A. A. Wells, N. E. White, S. D. Barthelmy, D. N. Burrows, L. R. Cominsky, K. C. Hurley, F. E. Marshall, P. Meszaros, P. W. A. Roming, L. Angelini, L. M. Barbier, T. Belloni, S. Campana, P. A. Caraveo, M. M. Chester, O. Citterio, T. L. Cline, M. S. Cropper, J. R. Cummings, A. J. Dean, E. D. Feigelson, E. E. Fenimore, D. . Frail, A. S. Fruchter, G. P. Garmire, K. Gendreau, G. Ghisellini, J. Greiner, J. E. Hill, S. D. Hunsberger, H. A. Krimm, S. R. Kulkarni, P. Kumar, F. Lebrun, N. M. Lloyd- Ronning, C. B. Markwardt, B. J. Mattson, R. F. Mushotzky, J. P. Norris, J. Osborne, B. Paczynski, D. M. Palmer, H. S. Park, A. M. Parsons, J. Paul, M. J. Rees, C. S. Reynolds, J. E. Rhoads, T. P. Sasseen, B. E. Schaefer, A. T. Short, A. P. Smale, I. A. Smith, L. Stella, G. Tagliaferri, T. Takahashi, M. Tashiro, L. K. Townsley, J. Tueller, M. J. L. Turner, M. Vietri, W. Voges, M. J. Ward, R. Willingale, F. M. Zerbi, and W. W. Zhang, “The Swift gamma-ray burst mission,” Astrophys. J., vol. 611, pp. 1005–1020, 2004.

[6] U.S. Department of Energy, “https://energy.gov/eere/sunshot/cadmium-telluride,” 2017. .

[7] H. W. Kraner, Z. Li, and E. Fretwurst, “The use of the signal current pulse shape to study the internal electric field profile and trapping effects in neutron damaged silicon detectors,” Nucl. Inst. Methods Phys. Res. A, vol. 326, no. 1–2, pp. 350–356, 1993.

[8] Š. Uxa, E. Belas, R. Grill, P. Praus, and R. B. James, “Determination of Electric-Field Profile in CdTe and CdZnTe Detectors Using Transient-Current Technique,” IEEE Trans. Nucl. Sci., vol. 59, no. 5, pp. 2402–2408, Oct. 2012.

[9] E. Fretwurst, V. Eremin, H. Feick, J. Gerhardt, Z. Li, and G. Lindström, “Investigation of damage-induced defects in silicon by TCT,” Nucl. Instruments Methods Phys. Res. Sect. A Accel. Spectrometers, Detect. Assoc. Equip., vol. 388, no. 3, pp. 356–360, 1997.

[10] K. Suzuki, T. Sawada, and S. Seto, “Temperature-Dependent Measurements of Time-of-Flight Current Waveforms in Schottky CdTe Detectors,” EEE Trans. Nucl. Sci., vol. 60, no. 4, pp. 2840–2844, 2013.

[11] C. Canali, M. Martini, G. Ottaviani, and K. R. Zanio, “Transport properties of CdTe,” Phys. Rev. B, vol. 4, no. 2, pp. 422–431, 1971.

[12] G. Ottaviani, C. Canali, C. Jacoboni, A. A. Quaranta, and K. Zanio, “Hole mobility and Poole-Frenkel effect in CdTe,” J. Appl. Phys., vol. 44, no. 1, pp. 360–371, 1973.

[13] S. M. Sze, Physics of Semiconductor Devices, 2nd ed. New York: John Wiley & Son, 1981.
[14] M. Sowinska, G. Hennard, D. Feder, M. Hage-Ali, J. Koebel, A. Zumbiehl, M. Ayoub, and P. Siffert, "Spectral characteristics of small- and large-volume CdTe detectors: Comparison among hemispheric, planar, and pixellated structure," *IEEE Trans. Nucl. Sci.*, vol. 49, no. 6, pp. 3306–3313, 202AD.
[15] O. Frisch, "British Atomic Energy Report," 1944.
[16] Y. Cui, A. E. Bolotnikov, G. Camarda, A. Hossain, G. Yang, and R. B. James, "CZT virtual Frisch-grid detector: Principles and applications," *2009 IEEE Long Isl. Syst. Appl. Technol. Conf.*, pp. 1–5, May 2009.
[17] A. E. Bolotnikov, G. C. Camarda, G. A. Carini, M. Fiederle, L. Li, D. S. McGregor, W. McNeil, G. W. Wright, and R. B. James, "Performance characteristics of Frisch-ring CdZnTe detectors," IEE*E Trans. Nucl. Sci.*, vol. 53, no. 2, pp. 607–614, Apr. 2006.
[18] B. W. Sturm, "GAMMA-RAY SPECTROSCOPY USING DEPTH-SENSING COPLANAR GRID CdZnTe," University of Michigan, 2007.
[19] M. Amman and P. N. Luke, "Optimization criteria for coplanar-grid detectors," *IEEE Trans. Nucl. Sci.*, vol. 46, no. 3, pp. 205–212, 1999.
[20] Z. He, G. F. Knoll, D. K. Wehe, and Y. F. Du, "Coplanar grid patterns and their effect on energy resolution of CdZnTe detectors," *Nucl. Instruments Methods Phys. Res. Sect. A Accel. Spectrometers, Detect. Assoc. Equip.*, vol. 411, no. 1, pp. 107–113, 1998.
[21] Z. He, G. F. Knoll, D. K. Wehe, and Y. F. Du, "Coplanar grid patterns and their effect on energy resolution of CdZnTe detectors," *Nucl. Instruments Methods Phys. Res. Sect. A*, vol. 411, pp. 107–113, 1997.
[22] R. H. Bube, *Photoelectronic Properties of Semiconductors*, 1st ed. Cambridge: Cambridge University Press, 1992.
[23] R. H. Bube, *Photoconductivity of Solids*, 2nd ed. New York: Robert E. Krieger Publishing Co., Inc., 1978.
[24] H. K. Henisch, *Semiconductor Contacts: An approach to ideas and models*, 1st ed. New York: Oxford University Press, 1984.
[25] P. Moravec, Z. F. Tomashik, V. G. Ivanits'Ka, V. M. Tomashik, J. Franc, K. Mašek, and P. Höschl, "Slow-polishing iodine-based etchant for CdTe and CdZnTe single crystals," *J. Electron. Mater.*, vol. 41, no. 10, pp. 2838–2845, 2012.
[26] L. Marchini, A. Zappettini, E. Gombia, R. Mosca, M. Lanata, and M. Pavesi, "Study of Surface Treatment Effects on the Metal-CdZnTe Interface," *IEEE Trans. Nucl. Sci.*, vol. 56, no. 4, pp. 1823–1826, Aug. 2009.
[27] L. A. Kosyachenko, O. L. Maslyanchuk, V. M. Sklyarchuk, E. V. Grushko, V. a. Gnatyuk, T. Aoki, and Y. Hatanaka, "Electrical characteristics of Schottky diodes based on semi-insulating CdTe single crystals," *J. Appl. Phys.*, vol. 101, no. 1, p. 13704, 2007.
[28] T. Takahashi, T. Mitani, Y. Kobayashi, M. Kouda, G. Sato, S. Watanabe, K. Nakazawa, Y. Okada, M. Funaki, R. Ohno, and K. Mori, "High-resolution Schottky CdTe diode detector," *IEEE Trans. Nucl. Sci.*, vol. 49, no. 3, pp. 1297–1303, Jun. 2002.
[29] K. Nakazawa, K. Oonuki, T. Tanaka, Y. Kobayashi, K. Tamura, T. Mitani, G. Sato, S. Watanabe, T. Takahashi, R. Ohno, a. Kitajima, Y. Kuroda, and M. Onishi, "Improvement of the CdTe diode detectors using a guard-ring electrode," *IEEE Trans. Nucl. Sci.*, vol. 51, no. 4, pp. 1881–1885, Aug. 2004.

[30] A. E. Bolotnikov, C. M. H. Chen, W. R. Cook, F. A. Harrison, I. Kuvvetli, and S. M. Schindler, "Effects of bulk and surface conductivity on the performance of CdZnTe pixel detectors," *IEEE Trans. Nucl. Sci.*, vol. 49, no. 4, pp. 1941–1949, Aug. 2002.
[31] M. Bugar, "Dynamics of structural defects in CdTe-based semiconductors," Charles University, 2011.
[32] G. F. Knoll, *Radiation Detection and Measurement*, 4th Edi. John Willey & Sons, Inc, 2010.
[33] K. Hecht, "For the mechanism of the photoelectric primary current in insulating crystals," *Zeits. Phys.*, vol. 77, pp. 235–245, 1932.
[34] J. Fink, H. Krüger, P. Lodomez, and N. Wermes, "Characterization of charge collection in CdTe and CZT using the transient current technique," *Nucl. Instruments Methods Phys. Res. A*, vol. 560, no. 2, pp. 435–443, May 2006.
[35] J. Pekárek, "Detektory RTG a gama záření na bázi polovodiče CdTe/CdZnTeCdTe / CdZnTe," Charles University, 2013.
[36] A. Cola, I. Farella, M. Anni, and M. C. Martucci, "Charge Transients by Variable Wavelength Optical Pulses in CdTe Nuclear Detectors," *IEEE Trans. Nucl. Sci.*, vol. 59, no. 4, pp. 1569–1574, 2012.
[37] J. R. Haynes and W. Shockley, "The Mobility and Life of Injected Holes and Electrons in Germanium," *Phys. Rev.*, vol. 81, no. 835, 1951.
[38] C. Canali, F. Nava, and L. Reggiani, "Drift velocity and diffusion coefficients from time-of-flight measurements," in *Topics in Applied Physics 58, Hot–Electron transport in Semiconductors,* 1st ed., L. Reggiani, Ed. New York: NY, USA: Springer, 1985, pp. 87–112.
[39] W. Bohne, W. Galster, K. Grabisch, and H. Morgenstern, "The influence of plasma effects on the timing properties of surface-barrier detectors for heavy ions," *Nucl. Inst. Methods Phys. Res. A*, vol. 240, no. 1, pp. 145–151, 1985.
[40] Š. Uxa, "Transport and optical properties of CdTe / CdZnTe single crystals," Charles University, 2014.
[41] P. J. Sellin, G. Prekas, J. Franc, and R. Grill, "Electric field distributions in CdZnTe due to reduced temperature and X-ray irradiation," *Appl. Phys. Lett.*, vol. 96, no. 133509, pp. 1–4, 2010.
[42] K. Suzuki, T. Sawada, and K. Imai, "Effect of DC Bias Field on the Time-of-Flight Current Waveforms of CdTe and CdZnTe Detectors," *IEEE Trans. Nucl. Sci.*, vol. 58, no. 4, pp. 1958–1963, Aug. 2011.
[43] H. Fujiwara, *Spectroscopic Ellipsometry: Principles and Applications*. Chichaster, UK: John Wiley & Son, 2007.
[44] J. Zazvorka, "Photoconductivity, photoluminescence and charge collection in semiinsulating CdTe and CdZnTe," Charles University, 2016.
[45] J. Zázvorka, J. Franc, M. Statelov, J. Pekárek, M. Veis, P. Moravec, and K. Mašek, "Optical and electrical study of CdZnTe surfaces passivated by KOH and NH4F solutions," *Appl. Surf. Sci.*, vol. 389, 2016.
[46] P. De Antonis, E. J. Morton, and F. J. W. Podd, "Infra-red Microscopy of Cd(Zn)Te Radiation Detectors Revealing Their Internal Electric Field Structure Under Bias," *IEEE Trans. Nucl. Sci.*, vol. 43, no. 3, pp. 1487–1490, 1996.
[47] A. Zumbiehl, M. Hage-Ali, P. Fougeres, J. M. Koebel, R. Regal, and P. Siffert, "Electric field distribution in CdTe and Cd1-xZnxTe nuclear detectors," *J. Cryst. Growth*, vol. 197, pp. 650–654, 1999.

[48] A. Burger, M. Groza, Y. Cui, D. Hillman, E. Brewer, A. Bilikiss, G. W. Wright, L. Li, F. Lu, and R. B. James, “Characterization of large single-crystal gamma-ray detectors of cadmium zinc telluride,” *J. Electron. Mater.*, vol. 32, no. 7, pp. 756–760, 2003.

[49] A. Cola, I. Farella, N. Auricchio, and E. Caroli, “Investigation of the electric field distribution in x-ray detectors by Pockels effect,” *J. Opt. A PURE Appl. Opt.*, vol. 8, pp. S467–S472, 2006.

[50] A. L. Washington, L. C. Teague, M. C. Duff, A. Burger, M. Groza, and V. Buliga, “Response of the Internal Electric Field in CdZnTe to Illumination at Multiple Optical Powers,” *J. Electron. Mater.*, vol. 41, no. 10, pp. 2874–2880, 2012.

[51] A. E. Bolotnikov, G. S. Camarda, E. Chen, S. Cheng, Y. Cui, R. Gul, R. Gallagher, V. Dedic, G. De Geronimo, L. O. Giraldo, J. Fried, A. Hossain, J. M. Mackenzie, P. Sellin, S. Taherion, E. Vernon, G. Yang, and R. B. James, “CdZnTe position-sensitive drift detectors with thicknesses up to 5 cm,” *Appl. Phys. Lett.*, vol. 108, no. 93504, pp. 1–5, 2016.

[52] M. Rejhon, “Vliv vnějších polí na elektrické pole a fotoproud detektorů CdTe,” Charles University, 2015.

[53] J. Pekarek, V. Dedic, J. Franc, E. Belas, M. Rejhon, P. Moravec, J. Tous, and J. Voltr, “Infrared LED Enhanced Spectroscopic CdZnTe Detector Working under High Fluxes of X-rays,” *Sensors*, vol. 16, no. 10, p. 1591, 2016.

[54] M. C. Duff, D. B. Hunter, A. Burger, M. Groza, V. Buliga, and D. R. Black, “Effect of surface preparation technique on the radiation detector performance of CdZnTe,” *Appl. Surf. Sci.*, vol. 254, pp. 2889–2892, 2008.

[55] A. Hossain, A. E. Bolotnikov, G. S. Camarda, Y. Cui, S. Babalola, A. Burger, and R. B. James, “Effects of Surface Processing on the Response of CZT Gamma Detectors : Studies with a Collimated Synchrotron X-Ray Beam,” *J. Electron. Mater.*, vol. 37, no. 9, p. 1356, 2008.

[56] G. Zha, J. Wanqi, T. Tingting, and W. Xiaoqin, “Effect of surface treatments on the electrical and optical properties of CdZnTe single crystal,” *Nucl. Instruments Methods Phys. Res. Sect. A*, vol. 566, pp. 495–499, 2006.

[57] V. A. Gnatyuk, O. I. Vlasenko, S. N. Levytskyi, E. Dieguez, J. Crocco, H. Bensalah, M. Fiederle, A. Fauler, and T. Aoki, “Surface processing of CdZnTe crystals,” *Proc. SPIE Hard X-ray/Gamma Ray, Neutron Opt. Sensors, Appl.*, vol. 8507, p. 85071S, 2012.

[58] A. J. Nelson, A. M. Conway, C. E. Reinhardt, J. L. Ferreira, R. J. Nikolic, and S. A. Payne, “X-ray photoemission analysis of passivated Cd(1−x)ZnxTe surfaces for improved radiation detectors,” *Mater. Lett.*, vol. 63, no. 2, pp. 180–181, Jan. 2009.

[59] A. Burger, H. Chen, K. Chattopadhyay, D. Shi, S. H. Morgan, W. E. Collins, and R. B. James, “Characterization of metal contacts on and surfaces of cadmium zinc telluride,” *Nucl. Instruments Methods Phys. Res. Sect. A*, vol. 428, pp. 8–13, 1999.

[60] L. A. Kosyachenko, V. M. Sklyarchuk, O. F. Sklyarchuk, O. L. Maslyanchuk, V. a. Gnatyuk, and T. Aoki, “Higher Voltage Ni/CdTe Schottky Diodes With Low Leakage Current,” *IEEE Trans. Nucl. Sci.*, vol. 56, no. 4, pp. 1827–1834, Aug. 2009.

[61] J. Pekárek, E. Belas, R. Grill, Š. Uxa, and R. B. James, “Characterization of CdTe and (CdZn) Te detectors with different metal contacts,” *Proc. SPIE 8852, Hard X-Ray, Gamma-Ray, Neutron Detect. Phys. XV, 88521F*, 2013.

[62] Q. Zheng, F. Dierre, J. Franc, J. Crocco, H. Bensalah, V. Corregidor, E. Alves, E. Ruiz, O. Vela, J. M. Perez, and E. Dieguez, "Investigation of generation of defects due to metallization on CdZnTe detectors," *J. Phys. D. Appl. Phys.*, vol. 45, p. 175102, 2012.

[63] Š. Uxa, E. Belas, R. Grill, P. Praus, and R. B. James, "Effect of contact preparation on the profile of the electric field in CdZnTe detectors," *J. Phys. D. Appl. Phys.*, vol. 46, no. 39, p. 395102, Oct. 2013.

[64] G. Wright, Y. Cui, U. N. Roy, C. Barnett, K. Reed, A. Burger, F. Lu, L. Li, and R. B. James, "The Effects of Chemical Etching on the Charge Nuclear Radiation Detectors," *IEEE Trans. Nucl. Sci.*, vol. 49, no. 5, pp. 2521–2525, 2002.

[65] G. W. Wright, R. B. James, D. Chinn, B. A. Brunett, R. W. Olsen, J. Van Scyoc, M. Cliftl, A. Burger, K. Chattopadhyay, D. Shi, and R. Wingfield, "Evaluation of NH4F / H202 Effectiveness as a Surface Passivation for Cd1-xZnxTe Crystals," *SPIE Proceeding Hard X-Ray, Gamma-Ray, Neutron Detect. Phys. II*, vol. 4141, 2000.

[66] W. Xiaoqin, J. Wanqi, L. Qiang, and G. Zhi, "Surface passivation of CdZnTe wafers," *Mater. Sci. Semicond. Process.*, vol. 8, no. 6, pp. 615–621, 2005.

[67] K. Chattopadhyay, M. Hayes, J.-O. Ndap, A. Burger, W. J. Lu, H. G. McWhinney, T. Grady, and R. B. James, "Surface passivation of cadmium zinc telluride radiation detectors by potassium hydroxide solution," *J. Electron. Mater.*, vol. 29, no. 6, pp. 708–712, 2000.

[68] V. G. Ivanits'ka, P. Moravec, J. Franc, Z. F. Tomashik, P. I. Feychuk, V. M. Tomashik, L. P. Shcherbak, K. Masek, and P. Höschl, "Chemical Etching of CdTe in Aqueous Solutions of H2O2-HI-Citric Acid," *J. Electron. Mater.*, vol. 36, no. 8, p. 1021, 2007.

[69] K.-T. H. Chen, S. U. Egarievwe, Z. Hu, J. Tong, D. T. Shi, G. H. Wu, C. M. S. Chen, M. A. George, W. E. Collins, A. Burger, R. B. James, and L. M. Bartlett, "Study of gamma-ray detector performance of cadmium zinc telluride crystals treated by different etchants," *Proc. SPIE Hard X-ray/Gamma Ray, Neutron Opt. Sensors, Appl.*, vol. 2859, pp. 255–262, 1996.

[70] A. Hossain, A. E. Bolotnikov, G. S. Camarda, Y. Cui, D. Jones, J. Hall, K. H. Kim, J. Mwathi, X. Tong, G. Yang, and R. B. James, "Novel Approach to Surface Processing for Improving the Efficiency of CdZnTe Detectors Role of Surface Roughness," *J. Electron. Mater.*, vol. 43, no. 8, pp. 2771–2777, 2014.

[71] M. Shkir, V. Ganesh, S. Alfaify, A. Black, E. Dieguez, and G. Bhagavannarayana, "VGF bulk growth, crystalline perfection and mechanical studies of CdZnTe single crystal: A detector grade materials," *J. Alloys Compd.*, vol. 686, pp. 438–446, 2016.

[72] J. Zazvorka, J. Franc, P. Moravec, E. Jesenska, L. Sedivy, J. Ulrych, and K. Masek, "Contactless resistivity and photoconductivity correlation to surface preparation of CdZnTe," *Appl. Surf. Sci.*, vol. 315, pp. 144–148, 2014.

[73] S. Tari, F. Aqariden, Y. Chang, C. Grein, and J. Li, "Impact of Surface Treatment on the Structural and Electronic Properties of Polished CdZnTe Surfaces for Radiation Detectors," *J. Electron. Mater.*, vol. 42, no. 11, pp. 3252–3259, 2013.

[74] Q. Zheng, F. Dierre, M. Ayoub, J. Crocco, H. Bensalah, V. Corregidor, E. Alves, R. Fernandez-Ruiz, J. M. Perez, and E. Dieguez, "Comparison of radiation detector performance for different metal contacts on CdZnTe deposited by electroless deposition method," *Cryst. Res. Technol.*, vol. 46, no.

11, pp. 1131–1136, 2011.
[75] Y. Nemirovsky, A. Ruzin, G. ASA, G. Gorelik, and L. Li, “Study of contacts to CdZnTe radiation detectors,” *J. Electron. Mater.*, vol. 26, no. 6, p. 756, 1997.
[76] J. Zázvorka, J. Franc, L. Beran, P. Moravec, J. Pekárek, and M. Veis, “Dynamics of native oxide growth on CdTe and CdZnTe X-ray and gamma-ray detectors,” *Sci. Technol. Adv. Mater.*, vol. 17, no. 1, pp. 792–798, 2016.
[77] D. S. Bale and C. Szeles, “Nature of polarization in wide-bandgap semiconductor detectors under high-flux irradiation: Application to semi-insulating Cd1−xZnxTe,” *Phys. Rev. B*, vol. 77, no. 35205, pp. 1–16, 2008.
[78] M. Strassburg, C. Schroeter, and P. Hackenschmied, “CdTe/CZT under high flux irradiation Matthias,” *J. Instrum.*, vol. 6, p. C01055, 2011.
[79] J. Franc, V. Dedic, P. J. Sellin, R. Grill, and P. Veeramani, “Radiation induced control of electric field in Au / CdTe / In structures,” *Appl. Phys. Lett.*, vol. 98, no. 232115, pp. 1–4, 2011.
[80] A. Cola and I. Farella, “Electric Field and Current Transport Mechanisms in Schottky CdTe X-ray Detectors under Perturbing Optical Radiation,” *Sensors*, vol. 13, pp. 9414–9434, 2013.
[81] M. Prokesch, D. S. Bale, and C. Szeles, “Fast High-Flux Response of CdZnTe X-Ray Detectors by Optical Manipulation of Deep Fast High-Flux Response of CdZnTe X-Ray Detectors by Optical Manipulation of Deep Level Defect Occupations,” *IEEE Trans. Nucl. Sci.*, vol. 57, no. 4, pp. 2397–2399, 2010.
[82] V. Dedic, J. Franc, P. J. Sellin, R. Grill, and V. Perumal, “Study on electric field in Au/CdZnTe/In detectors under high fluxes of X-ray and laser irradiation,” *J. Instrum.*, vol. 7, p. P02011, 2012.
[83] V. Dedic, J. Franc, M. Rejhon, R. Grill, and P. J. Sellin, “De-polarization of a CdZnTe radiation detector by pulsed infrared light,” *Appl. Phys. Lett.*, vol. 107, no. 32105, pp. 1–5, 2015.
[84] J. Franc, V. Dedic, J. Zazvorka, M. Hakl, R. Grill, and P. J. Sellin, “Flux-dependent electric field changes in semi-insulating CdZnTe,” *J. Phys. D. Appl. Phys.*, vol. 46, no. 235306, p. 4, 2013.
[85] J. Franc, V. Dedic, M. Rejhon, J. Zazvorka, P. Praus, J. Tous, and J. Sellin, “Control of electric field in CdZnTe radiation detectors by above-bandgap light,” *J. Appl. Phys.*, vol. 117, no. 165702, pp. 1–8, 2015.
[86] J. Zazvorka, J. Franc, V. Dedic, and M. Hakl, “Electric field response to infrared illumination in CdTe/CdZnTe detectors,” *J. Instrum.*, vol. 9, no. C04038, p. 7, 2014.
[87] R. Echeverria, A. B. Vicent, and N. V. Joshi, “Photoquenching Effect and Its Consequence in p Type Gallium Arsenid,” *Solid State Commun.*, vol. 52, no. 11, pp. 901–904, 1984.
[88] M. Martini, J. W. Mayer, and K. R. Zanio, “Drift velocity and trapping in semiconductors - Transient charge technique,” in *Applied Solid State Science, Advances in Materials and Device Research*, vol. 3, R. Wolfe, Ed. New York: NY, USA: Academic, 1972.
[89] H. Pernegger, S. Roe, P. Weilhammer, V. Eremin, H. Frais-Kölbl, E. Griesmayer, H. Kagan, S. Schnetzer, R. Stone, W. Trischuk, D. Twitchen, and A. Whitehead, “Charge-carrier properties in synthetic single-crystal diamond measured with the transient-current technique,” *J. Appl. Phys.*, vol. 97, no. 7, p. 9, 2005.

[90] A. Savitzky and M. J. Golay, "Smoothing and Differentiation of Data by Simplified Least Squares Procedures," *Anal. Chem.*, vol. 36, no. 8, pp. 1627–1639, 1964.
[91] O. Madelung, *Semiconductors: Data Handbook*, 3rd ed. New York: Springer, 2004.
[92] K. Suzuki, S. Seto, A. Iwata, and M. Bingo, "Transport Properties of Undoped Cd0.9Zn0.1Te Grown by High Pressure Bridgman Technique," *J. Electron. Mater.*, vol. 29, no. 6, pp. 704–707, 2000.
[93] Z. Burshtein, H. N. Jayatirtha, A. Burger, J. F. Butler, B. Apotovsky, and F. P. Doty, "Charge-carrier mobilities in Cd0.8Zn0.2Te single crystals used as nuclear radiation detectors," *Appl. Phys. Lett.*, vol. 63, no. 1, pp. 102–104, 1993.
[94] J. C. Erickson, H. W. Yao, R. B. James, H. Hermon, and M. Greaves, "Time of flight experimental studies of CdZnTe radiation detectors," *J. Electron. Mater.*, vol. 29, no. 6, pp. 699–703, 2000.
[95] R. Grill, E. Belas, J. Franc, and M. Bugár, "Polarization Study of Defect Structure of CdTe Radiation Detectors," *IEEE Trans. Nucl. Sci.*, vol. 58, no. 6, pp. 3172–3181, 2011.
[96] P. Russo, M. Quattrocchi, and E. Bertolucci, "Response of semi-insulating GaAs detectors to near-infrared picosecond light pulses," *Nucl. Instruments Methods Phys. Res. Sect. A Accel. Spectrometers, Detect. Assoc. Equip.*, vol. 466, no. 1, pp. 105–114, 2001.
[97] J. Harkonen, E. Tuovinen, P. Luukka, I. Kassamakov, M. Autioniemi, E. Tuominen, P. Sane, P. Pusa, J. Raisanen, V. Eremin, E. Verbitskaya, and Z. Li, "Low-temperature TCT characterization of heavily proton irradiated p-type magnetic Czochralski silicon detectors," *Nucl. Instruments Methods Phys. Res. Sect. A Accel. Spectrometers, Detect. Assoc. Equip.*, vol. 583, no. 1, pp. 71–76, 2007.
[98] P. Horodyský, R. Grill, and P. Hlídek, "Band-edge photoluminescence in CdTe," *Phys. Status Solidi Basic Res.*, vol. 243, no. 12, pp. 2882–2891, 2006.
[99] J. Franc, P. Hlídek, P. Moravec, E. Belas, P. Höschl, L. Turjanska, and R. Varghová, "Determination of energy gap in Cd1−xZnxTe (x = 0-0.06)," *Semicond. Sci. Technol.*, vol. 15, pp. 561–564, 2000.
[100] Y. Cui, M. Groza, D. Hillman, A. Burger, and R. B. James, "Study of surface recombination velocity of Cd(1−x)Zn(x)Te radiation detectors by direct current photoconductivity," *J. Appl. Phys.*, vol. 92, no. 5, p. 2556, 2002.
[101] A. Cavallini, D. Cavalcoli, A. Castaldini, and B. Fraboni, "Photocurrent and Surface Photovoltage Spectroscopy Investigations of CdTe-based Compounds," *IEEE Trans. Nucl. Sci.*, vol. 54, no. 5, pp. 1719–1722, 2007.
[102] P. Praus, E. Belas, J. Franc, R. Grill, P. Höschl, and J. Pekárek, "Electronic Pulse Shape Formation in Transient Charge and Transient Current Detection Approach in (CdZn)Te Detectors," *IEEE Trans. Nucl. Sci.*, vol. 61, no. 4, pp. 2333–2337, 2014.
[103] W. H. Press, S. A. Teukolsky, W. T. Vatterling, and B. P. Flannery, *Numerical Recepes in Fortran*, 2nd ed. Cambridge: U.K: Cambridge Univ. Press, 1992.
[104] P. H. van Cittert, *Z. Phys.*, vol. 65, p. 547, 1930.
[105] P. Bandžuch, M. Morháč, and J. Krištiak, "Study of the Van Cittert and Gold iterative methods of deconvolution and their application in the deconvolution of experimental spectra of positron annihilation," *Nucl. Instruments Methods Phys. Res. Sect. A Accel. Spectrometers, Detect. Assoc. Equip.*, vol. 384, pp.

506–515, 1997.
[106] M. Zanichelli *et al.*, “Characterization of bulk and surface transport mechanisms by means of the photocurrent technique,” *IEEE Trans. Nucl. Sci.*, vol. 56, no. 6, pp. 3591–3596, 2009.
[107] Y. Cui, G. W. Wright, X. Ma, K. Chattopadhyay, R. B. James, and A. Burger, “DC photoconductivity study of semi-insulating Cd1−xZnxTe crystals,” *J. Electron. Mater.*, vol. 30, no. 6, pp. 774–778, 2001.
[108] K. Suzuki, S. Seto, T. Sawada, and K. Imai, “Effects of sub-gap irradiation on the time-of-flight current waveforms of high resistivity CdTe,” *Phys. Status Solidi C Conf.*, vol. 3, no. 4, pp. 1130–1134, 2006.
[109] P. N. Luke, “Unipolar Charge Sensing with Coplanar Electrodes—Application to Semiconductor Detectors,” *IEEE Trans. Nucl. Sci.*, vol. 42, no. 4, pp. 207–213, 1995.
[110] W. Shockley, “Currents to Conductors Induced by a Moving Point Charge,” *J. Appl. Phys.*, vol. 9, pp. 635–636, 1938.
[111] S. Ramo, “Currents Induced by Electron Motion,” *IEEE Trans. Nucl. Sci.*, vol. 27, no. 9, pp. 584–585, 1939.
[112] G. Cavalleri, E. Gatti, G. Fabri, and V. Svelto, “Extension of Ramo’s theorem as applied to induced charge in semiconductor detectors,” *Nucl. Instruments Methods*, vol. 92, no. 1, pp. 137–140, 1971.
[113] Z. He, “Review of the Shockley-Ramo theorem and its application in semiconductor gamma-ray detectors,” *Nucl. Instruments Methods Phys. Res. Sect. A Accel. Spectrometers, Detect. Assoc. Equip.*, vol. 463, no. 1, pp. 250–267, 2001.
[114] A. Cola and I. Farella, “Electric fields and dominant carrier transport mechanisms in CdTe Schottky detectors,” *Appl. Phys. Lett.*, vol. 102, no. 11, p. 5, 2013.
[115] A. Santi, M. Zanichelli, G. Piacentini, M. Pavesi, A. Cola, and I. Farella, “An original method to evaluate the transport parameters and reconstruct the electric field in solid-state photodetectors,” *Appl. Phys. Lett.*, vol. 104, no. 19, p. 5, 2014.
[116] J. Pekarek, E. Belas, and J. Zazvorka, “Long-Term Stable Surface Treatments on CdTe and CdZnTe Radiation Detectors,” *J. Electron. Mater.*, vol. 46, no. 4, pp. 1996–2002, 2016.
[117] P. Praus, J. Kunc, E. Belas, J. Pekarek, and R. Grill, “Charge transport in CdZnTe coplanar grid detectors examined by laser induced transient currents,” *Appl. Phys. Lett.*, vol. 109, no. 13, pp. 1–6, 2016.
[118] P. Praus, E. Belas, J. Bok, R. Grill, and J. Pekárek, “Laser Induced Transient Current Pulse Shape Formation in (CdZn)Te Detectors,” *IEEE Trans. Nucl. Sci.*, vol. 63, no. 1, pp. 246–251, 2016.
[119] J. Zázvorka, P. Hlídek, J. Franc, J. Pekárek, and R. Grill, “Photoluminescence study of surface treatment effects on detector-grade CdTe:In,” *Semicond. Sci. Technol.*, vol. 31, no. 2, 2015.

List of Tables

Table 3.1 *Types of radiation sources.* 25

Table 4.1 *Labelling of samples for surface treatment study and their resistivity obtained by contactless resistivity measurement (COREMA)* 39

Table 4.2 *Resolution ($R\gamma$), $CCE\gamma$ and current (I) for various surface treatments on the CZT-I sample at bias of -800 V* 43

Table 6.1 *Electron mobility-lifetime product determined on CZT-D2 and CZT-D1 samples by alpha, low energy gamma and laser-induced pulse height spectrum analysis and by L-TCT via Standard Hecht and Surface Hecht equation, respectively* 86

List of Abbreviations

CdTe	cadmium telluride
CdZnTe/CZT	cadmium zinc telluride
CCE	charge collection efficiency
IR	infrared
TCT	transient-current-technique
(e-h) pairs	electron-hole pairs
IoP CU	Institute of Physics of Charles University
VGF	vertical-gradient-freeze
HPB	high-pressure-Bridgeman
THM	travelling-heater-method
E_g	bandgap energy
Z	atomic number
ρ	resistivity
$\mu\tau$	mobility-lifetime product
CPG	coplanar-grid detector
FG	Frish-grid
CG	collecting grid
NCG	non-collecting grid
FWHM	full width at half maximum
L	sample width
MS	metal-semiconductor
MOS	metal-oxid-semiconductor
$\phi_{m/s}$	work function of metal/semiconductor
$F_{m/s}$	Fermi level of metal/semiconductor
E_{vac}	energy of vacuum
χ_{s}	electron affinity of semiconductor

E_c	conducting band
E_v	valence band
ϕ_B	barrier height
GR	guard ring
R	rate of capture/recombination
S_c	cross section of charge carriers
v_{th}	thermal velocity of free carriers
n/p	density of free electrons/holes
N_t	density of trapping centres
τ	lifetime
V_A, V_B	vacancies of A, B compound
A_i, B_i	interstitials of A, B compound
B_A, A_B	antisite defects of A, B compound
$\mathbf{J_{tot}}$	total current density
$\mathbf{J_{dr}}$	drift current
$\mathbf{J_{df}}$	diffusion current
$\sigma_{n/p}$	conductivity of electrons/holes
e	charge per electron
$\mu_{n/p}$	mobility of electrons/holes
E	electric field strength
v_{dr}	drift velocity of carriers
m_n^*	effective mass of the electron
τ_{sc}	scattering relaxation time
D_n	electron diffusion coefficient
k	Boltzmann constant
T	temperature
kT	thermal energy

G	photoexcitation rate
μ_d	drift mobility
n_t	density of trapped carriers
ToF	time of flight
t_r	transit time
τ_g	time of electron-hole pair generation
τ_ϵ	dielectric relaxation time
ϵ_0	vacuum permittivity
ϵ_r	relative permittivity of the material
CWFs	current waveforms
ρ_{SC}	space-charge density
a	linear slope of the electric field
E_0	electric field under the irradiated electrode
N	space-charge density
DW	depletion width
Q	total collected charge
MCA	multi channel analyser
v	velocity
V	voltage
I	current
R_γ	gamma resolution
E_γ	energy of the monoenergetic source of radiation
TChT	transient charge technique
FET	field-effect transistor
Ψ, Δ	ellipsometric angles
EMA	effective medium approximation
$\boldsymbol{\eta}$	impertivity tensor

T	transmittance
r_{41}	Pockels coefficient for CdTe/CZT material
LED	light emitting diode
COREMA	contactless resistivity mapping
XPS	X-ray photoelectron spectroscopy
(BM)	bromine-methanol etching
(BE)	brome-ethylene glycol polishing
(BEBM)	brome-ethylene glycol polishing + bromine-methanol etching
(NHF)	passivation in NH_4F/H_2O_2
(KOH)	passivation in KOH
IRSS	infrared spectral scanning
CPS	counts per second
MSM	maximum slope method
PFE	Poole–Frenkel effect
α-TCT	alpha-induced transient current technique
L-TCT	laser-induced transient current technique
DEC	detector equivalent circuit
$j(t)$	decayed current
j_0	source function
g	device transfer function
$j_s(t)$	TCT signal
$j_s(t)/J_{s0}$	normalized response signal
$\Theta(t)$	step function
δ(t)	Dirac function
DRM	Direct Recurrent Method
q_c	maximum collected charge
L-spect	laser-induced pulse height spectroscopy

s	surface recombination velocity
V_B	detector bias
V_{IG}	intergrid voltage
D_g	distance between the adjacent grid centres
N_D	positive space charge concentration
N_A	negative space charge concentration
v_{sat}	saturation velocity
δt	temporal broadening
$\varphi(x,y)$	electrostatic potential
IoP CU	Institute of Physics of Charles University